Minimization of drainage time of filled PET bottle with initial rotation

A numerical study

by

Lim Chi Ho

to obtain the degree of **Master of Science** in Mechanical Engineering
at the **Delft University of Technology**
to be publicly defended on Tuesday November 24th, 2020 at 13:00 PM.

Student:	Lim Chi Ho	
Student number:	4458109	
Department document number:	P&E-3035	
Thesis supervisor:	Dr.ir. W.-P. Breugem	TU Delft
	Dr.ir. M.J.B.M. Pourquie	TU Delft
Thesis committee:	Dr.ir. W.-P. Breugem	TU Delft, Chairman
	Dr.ir. M.J.B.M. Pourquie	TU Delft
	Dr. R. Delfos	TU Delft

Abstract

The drainage time of liquid-filled PET bottles can be greatly reduced by pre-rotating the bottle with a certain angular velocity. Depending on the magnitude of the angular velocity, up to four different flow regimes can be distinguished during the emptying of a bottle: bubble regime, transition regime, vortex regime and the swirl regime. At zero or low pre-rotation, the flow is in the so-called bubble regime in which the intermittent downward liquid flow is accompanied by an upward motion of irregularly shaped air bubbles into the bottle. At sufficiently high pre-rotation, the picture is completely different. After initial transient behaviour in which the flow is first in the bubble regime, the flow undergoes transition towards a so-called vortex regime. This is characterized by regular downward motion of liquid along the bottle wall in a free-surface vortex and accompanying upward motion of air through the nozzle core. Finally, close to the end of the drainage process another transition towards a so-called swirl regime takes place, in which the last bit of liquid swirls around in the bottle before being slowed down sufficiently to exit the bottle through the nozzle opening. Dimensional analysis indicates that for a specific bottle geometry the non-dimensional total drainage time $t_d/t_{d,0}$, where $t_{d,0}$ is a characteristic drainage time scale for stationary low-viscosity fluids in the bubble regime, depends primarily on 3 non-dimensional numbers: (1) the rotation number, Π (2) the Morton number, Mo, and (3) the Eötvos number, Eo. The former represents the characteristic ratio of centrifugal to hydrostatic forces inside the liquid phase. The objective of this study is to determine the relationship between the non-dimensional drainage time and Π and gain insight in the influence of Eötvos and Morton onto this. To this purpose, a parametric CFD study of a model PET bottle has been conducted and the results have been compared with previous preliminary experiments performed in our group.

The numerical study is divided into three categories, each discussing the influence of one of the dimensionless parameters. The influence of the Π-number was studied by altering the initial rotational velocity of the bottle. It was found that at some critical Π-number, the drainage time was minimal. A further increase beyond the critical Π-number resulted in a longer drainage time, due to the stronger centrifugal force acting on the liquid layer. It was found through an analytical solution and verified with the numerical results that the rate at which the Π-number grows in relation to the dimensionless drainage time is to the power 3 for the laminar case and to the power 3/2 for the turbulent case. Below the critical value, the flow is expected to remain in the so-called bubble regime, also increasing the drainage time. Furthermore, the onset of the vortex regime was expected to occur at a constant value of Π. This was also verified with the numerical results and a strong correlation was found between the onset and the corresponding local Π-number. The influence of the Morton number is also discussed, where an increase in the Morton number was realized with an increase in viscosity. It was found that the drainage time got substantially reduced with an increase in viscosity. The effects of viscous dissipation resulted in a bigger effective area and higher axial downward flow velocity. However, increasing the Morton number excessively would result in the flow regime remaining in the bubble regime. Therefore, the critical Π-number shifts depending on the different fluid compositions. When varying the Eötvos number, by both changing the viscosity and the surface tension, it was found that the latter had negligible effect on the generation of the air-core or the drainage time.

Keywords: *air-core vortex, bubble regime, multi-phase numerical study, PET bottle, Computational Fluid Dynamics, swirling flow*

Acknowledgements

Hereby I would like to express my sincere gratitude to all whom have contributed in making this study possible.

First of all, I would like to express my appreciation to dr.ir. W.P. Breugem and dr.ir. M.J.B.M. Pourquie for their valuable and constructive suggestions and aid during the whole process of this thesis. Wim-Paul, thank you for consistently providing time every two weeks and guiding me through this thesis, even when your twins were born. Mathieu, thank you for your patience and all the help when teaching me how to work on the cluster and the basics of Ansys.

Second of all, I would like to thank my parents, Stephen and Daphne, for their unconditional and irreplaceable support. Without their support, I would not have made it this far on my own.

Lastly, I am grateful for all my friends and fellow students who made my master thesis tolerable. Due to COVID, constantly working from home was not the most pleasant experience. I want to thank them for accompanying me during the study hours and providing me with the right amount of distractions during my free time.

Contents

List of Figures

List of Tables

Nomenclature

Symbol	**Description**	**Unit**
ρ	density	kg/m^3
μ	dynamic viscosity	kg/(m·s)
ν	kinematic viscosity	m^2/s
γ	surface tension	kg/s^2
p	pressure	kg/(m·s^2)
p_{atm}	atmospheric pressure	kg/(m·s^2)
g	gravitational acceleration	m/s^2
u	velocity	m/s
u_T	terminal rise velocity	m/s
$u_{T,0}$	stagnant terminal rise velocity	m/s
U_l	mean liquid velocity	m/s
u_τ	frictional velocity	m/s
u_h	outward velocity of the bottle opening	m/s
u_b	bulk velocity	m/s
$\overline{u}$, u'	mean velocity, fluctuating velocity of Reynolds decomposition	m/s
u_r, u_θ, u_z	radial, circumferential and axial velocity	m/s
Ω,ω	angular velocity, local angular velocity	s^{-1}
Ω_b	initial angular velocity of the bottle	s^{-1}
Ω_h	angular velocity of the interface at the bottle opening	s^{-1}
f	Coriolis parameter	s^{-1}
$f_1.f_2$	frequency modulation	s^{-1}
Γ	circulation	m^2/s
t	time	s
t_d,$t_{d,0}$	drainage time, drainage time of stationary bottle	s
t_{Ek}, t_{dif}	Ekman spin-up time, radial diffusion time	s
T	time period	s
D	diameter	m
D_e	equivalent diameter	m
d_b, d_h	bottle diameter, bottle opening diameter	m
R	radius	m
r_i	radius of the interface	m
r_h	radius of the bottle opening	m
θ	nozzle angle	°
H	height	m
h_0	initial liquid level	m
h_c	critical submergence height	m
A	area	m^2
A_{liquid}	effective liquid area in the bottle opening	m^2
A_{cell}	cell area	m^2
n_{cell}	amount of cells	-
δ	boundary layer thickness	m
V	volume	m^3
V_b	liquid volume of the bottle	m^3
Q	total flow rate	m^3/s
$\dot{m}$	total mass flow	kg/s
σ	stress tensor	kg/(m·s^2)
$\lvert E\rvert$	strain rate magnitude	-
b	body force	kg·m·s^{-2}

E	energy	J
α_k	volume fraction of phase k	-
ω	growth rate	s^{-1}
k	wave number	m^{-1}
λ	wave length	m
κ	curvature	m^{-1}
τ_w	wall shear stress	$\mathrm{kg/(m{\cdot}s^2)}$
α	volume fraction	-
α_{liquid}	liquid volume fraction	-
α_{gas}	gas volume fraction	-
$\mathbf{n}$	normal vector	-
ϕ	level set function	-
C_f	Schlichting skin-friction correlation	-
C_{CFL}	Courant number	-
$y+$	dimensionless wall unit	-
I	identity matrix	-
$x_{i,o}$	subscript for inner and outer	-
$x_{d,c}$	subscript for dispersed and continuous phase	-
$x_{H,L}$	subscript for heavier and lighter fluid	-
$x_{I,R}$	subscript for inertial and rotating frame of reference	-
$x_{h,b}$	subscript for bottle opening and bottle	-
$x_{1,2}$	subscript for bottom and top fluid	-

Dimensionless parameter	**Description**
Fr	Froude
Mo	Morton
Eo	Eötvos
Π	Rotational number, Pi
$\Pi_{critical}$	Critical Pi number
Π_{onset}	Onset Pi number
Re,	Reynolds number
Re_T	Terminal Reynolds number
Re_o,Re_i	outer, inner cylinder Reynolds number
$Re*$	Reduced Reynolds number
Re_c	Critical instability Reynolds number
N_f	Inverse viscosity or $\sqrt{Ga}$
Ga	Galileo number
Ro	Rossby
Ek	Ekman
Ta	Taylor
A	Atwood
$t*$	dimensionless drainage time
$d*$	normalized neck diameter
$L*$	dimensionless critical distance
$D*$	tank diameter ratio
$A*$	aspect ratio

1 Introduction

Vortex flows are not uncommon in nature and technology. A good example of this vortex flow is when emptying a kitchen sink or a bathtub full of water. These so-called bathtub vortices may look innocent on the outside, however the swirling flow of these vortices can cause a number of problems at hydraulic intakes of mechanical or industrial equipment. For example, the vortex can decrease the pump or turbine efficiency. The bathtub vortex generates a dimple in the free surface and sometimes this results in a fully developed air core that grows into the hydraulic intake. This leads to a decrease in the maximum flow rate into the intake resulting in a decrease in efficiency. Also due to the presence of the air core in the vortex, floating matter, trash and dirty air may increase the risk of damage due to the extra moving parts being dragged into the hydraulic devices. Typical examples where the bathtub vortices decrease the efficiency are rocket fuel tanks [1] and power plant cooling systems [2]. Due to the complexity of this phenomenon and the several issues stated above, it is important to study and analyze the formation and evolution mechanism of the free surface vortex theoretically.

However, the air-core vortex can also be used to increase efficiencies in certain other industries. A good example is a gravitational water vortex power plant, where due to the generated air-core vortex, energy can be gained and turned into electricity. [3] Another example can be found in the soda industry where numerous soda PET bottles have to be filled and emptied during the production process. Since the PET bottles only have one opening, the pressure in the air-layer exhibits a transient behaviour, where the downward liquid flow has to be accompanied by a simultaneous upward air flow into the bottle due to the rising under-pressure at the top of the bottle. However, due to the hydrostatic force overpowering the surface tension force at the interface near the bottle opening, the hydrostatic force divides the air stream into multiple air bubbles. Therefore, this regime is defined as the bubble regime. A visualization of how the bubble regime develops from the moment the bottle is opened is shown in figure 1. It is believed that the pulsating behaviour of the bubble regime increases the drainage time significantly, resulting in a decrease of the efficiency of the bottle emptying process.

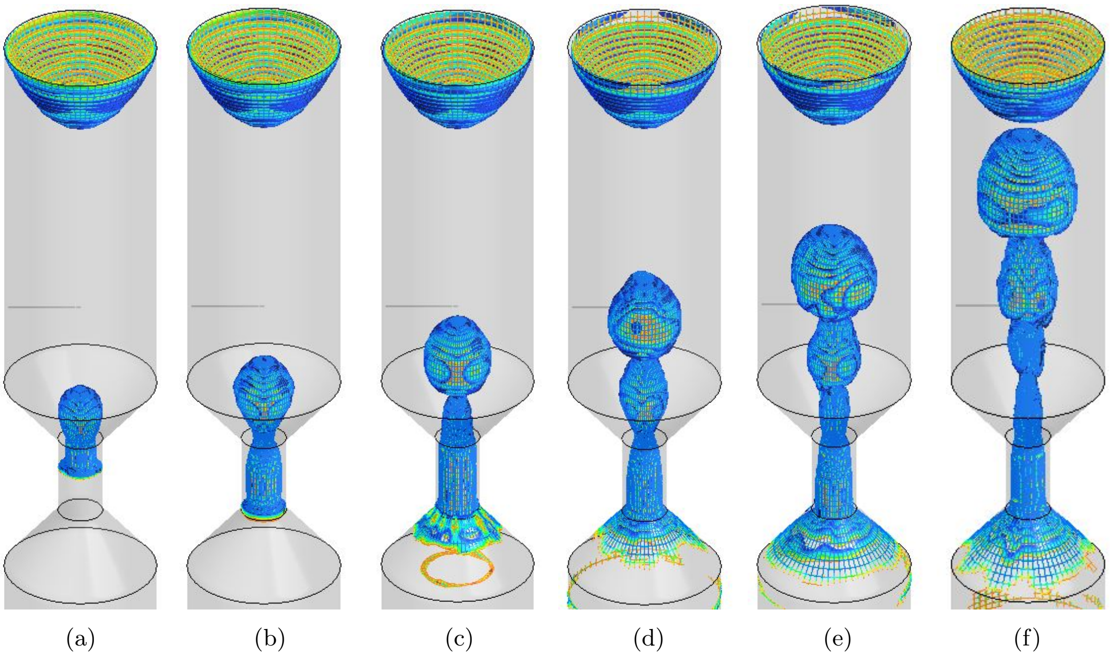
(a) (b) (c) (d) (e) (f)

Figure 1: CFD results of the interface from the bubble regime where a time step of $\Delta t = 0.05$ s is taken between each picture. The starting time value in figure (a) is $t = 0.05$ s. The initial angular velocity of the bottle is 50 rad/s. The fluid consists of 40% glycerol and 60% water.

One way to increase the emptying efficiency is by pre-rotating the bottle with a certain angular velocity.

At sufficiently high pre-rotation, the flow undergoes transient behaviour, where the bubble regime transitions into a so-called vortex regime. This regime is characterized by a continuous downward liquid flow along the wall in the form of an air-core vortex, while air entrains through the air-core into the bottle. Due to the continuous liquid flow. an increase in the liquid flow rate is obtained, resulting in a shorter drainage time. An example of the transition period can be seen in figure 2 a-c, and a visualization of a fully developed vortex is depicted in 2 d.

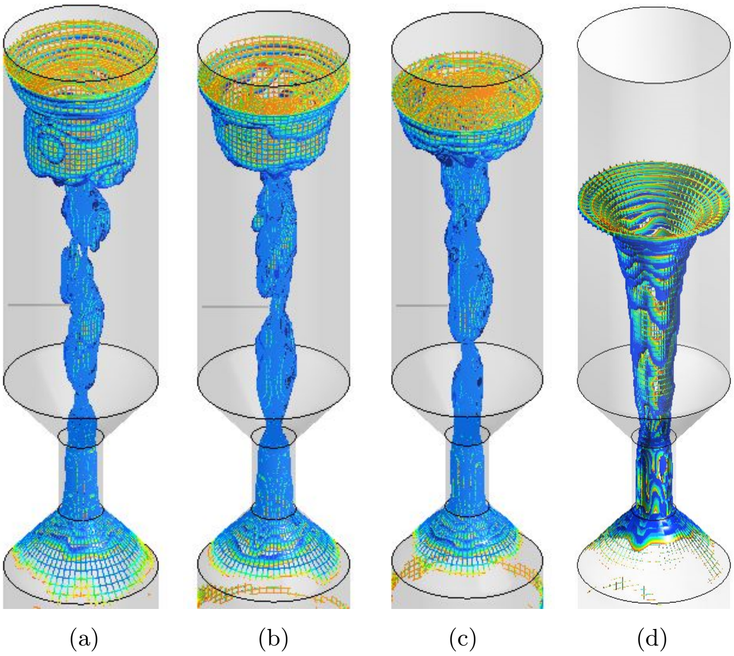

Figure 2: CFD results of the interface with an initial angular velocity of 50 rad/s. The fluid consists of 40% glycerol and 60% water. a)-c) liquid transitioning behaviour with $\Delta t = 0.05$ s d) vortex regime at $t = 3$ s.

To enhance the efficiency of the soda industry and study the flow behaviour of this vortex flow, a group of bachelor students from the Delft University of Technology have performed experimental studies on the draining time of a model PET bottle. A short summary of their findings can be found in appendix A. By studying the effects of initial angular velocities and different viscosities, the minimal drainage time was tried to be obtained. They found that for a water filled bottle, the drainage time for the stationary bottle was around 20 seconds, whereas for the pre-rotated bottle, the minimized drainage time was 7 seconds. Their conclusion was that the minimal outflow time was obtained when the initial angular velocity would create a somewhat stammering vortex by keeping the angular velocity as low as possible, but high enough to avoid the bubble regime. They also found that the viscosity of the fluid had a significant influence on the generation of the vortex. This study will elaborate on their results by performing a numerical investigation on this topic. A major advantage of CFD is that it provides detailed information on the 3D and instantaneous flow. Furthermore, it is an excellent tool for a parametric study of the influence of relevant flow parameters, recast in terms of non-dimensional numbers, on the drainage time. From Buckingham-Pi theorem, three dimensionless parameters were selected to study their influence on the non-dimensional drainage time, namely the (1) rotation number, Π (2) Morton number, Mo (3) Eötvos number, Eo. The rotation number represents the characteristic ratio between the centrifugal to the hydrostatic force on the liquid layer. The Morton number represents the ratio between the viscous and surface tension forces and the Eötvos number is the ratio between the buoyancy and surface tension forces. The non-dimensional drainage time is defined as the ratio between the drainage time of the tested case and the emptying time of a stationary bottle. It is believed that the non-dimensional drainage time depends primarily on the three non-dimensional numbers. By changing the initial angular velocity, viscosity and surface tension re-casted in these non-dimensional parameters, it is believed that the minimal non-dimensional drainage time can be obtained.

This study is divided into six parts, where in chapter 2, a literature review is performed on existing studies. Chapter 3 will focus on the numerical analysis and elaborate on certain simulation strategies and computational methods. The results will be shown and discussed in chapter 4. In the fifth chapter, the final conclusion will be drawn on how to minimize the overall drainage time of the bottle. In the sixth chapter, recommendations will be given on how to continue on this study. The last chapter is the appendix containing relevant elaborations on certain topics in this study.

Thesis scope: Aims and objectives

The aim of this study is to determine for which initial angular velocity the total drainage time of a liquid-filled PET bottle is minimized. It is expected that the initial rotational velocity, fluid properties such as surface tension and viscosity all have a big influence on the drainage time of the bottle. The primary hypothesis of this study is that **an optimal initial rotational velocity should exist, where the velocity should be just high enough to create a fully developed air-core vortex**. Initial angular velocities beyond this magnitude will decrease the volumetric flow rate due to the lower available through-flow area for the downward liquid flow in the nozzle accompanied by the increase of the rotational velocity. Also, it is expected that for a bigger liquid through-flow area, less fluid will be effected by the friction due to wall effects. The drainage time can also be reduced by altering the fluid properties. It is believed that by increasing viscosity, the drainage time can be heavily decreased. This is due to viscous dissipation reducing the centrifugal force and therefore enhancing the downward liquid velocity. Thus, for this thesis, the main objective is to study the effects of the three different parameters through the use of three dimensionless numbers.

The following are a list of the general thesis objectives:

1. Finding the optimal initial angular velocity to minimize the total drainage time.
2. Obtaining the relationship between the non-dimensional drainage time and Π.
3. Determining the influence of the Morton number on the drainage time.
4. Determining the influence of the Eötvos number on the drainage time.

By studying these four main objectives, it is believed that the minimal drainage time can be acquired-.

2 Literature study

2.1 Drainage from a closed reservoir in absence of rotation

Since the PET bottle only has one opening, due to the closed end-wall at the top, the downward liquid flow has to be accompanied by a simultaneous upward air flow into the bottle. This regime, called the bubble regime, is characterized where large air bubbles with diameters of the order of the bottle neck are generated periodically and rise into the bottle until it burst at the free surface at the top. Numerous researchers have studied the motion of these bubbles in vertical pipes and free space analytically and experimentally. Their findings will be discussed in this subsection of the literature study.

2.1.1 Dimensionless parameters

When looking at air bubbles, different dimensionless parameters can give good insight on for example the shape and size of the bubble or on the terminal velocity for one single air bubble. The various dimensionless groups are given as

$$Fr = \frac{u_T}{\sqrt{gD_e}} \tag{1}$$

the Froude number, which is given as the ratio between the inertial and gravitational forces, where u_T is the terminal velocity and D_e the equivalent diameter of the bubble;

$$Mo = \frac{\mid \rho_d - \rho_c \mid g\mu_c^4}{\rho_c^2\gamma^3} \tag{2}$$

the Morton number, which represents the ratio between the viscous and surface tension forces where ρ_d and ρ_c are the densities of the dispersed (bubbles) and the continuous (liquid) phase respectively, μ_c the dynamic viscosity of the continuous phase and γ is the surface tension;

$$Eo = \frac{\mid \rho_d - \rho_c \mid gD_e^2}{\gamma} \tag{3}$$

the Eötvos number, which is the ratio between the buoyancy and surface tension forces;

$$Re_T = \frac{u_T D_e}{\nu_c} \tag{4}$$

the terminal Reynolds number which displays the ratio between the inertial and viscous forces through the terminal velocity of the bubble, where ν_c is the kinematic viscosity of the continuous phase.

$$N_{\mathrm{f}} = \left(\frac{Eo^3}{Mo}\right)^{1/4} \tag{5}$$

the 'dimensionless inverse viscosity'.[4] When surface tension is negligible (for $Eo > 40$) [5], then the characteristics of the bubble are determined by the inertial and viscous forces. By combining the Eötvos and Morton number to eliminate the surface tension force, the new dimensionless parameter depicted in equation 5 can be derived. This dimensionless parameter is also present as the Galileo number ($Ga = N_{\mathrm{f}}^2$) in literature.[6]

2.1.2 Rayleigh-Taylor instability

During the pre-rotating of the bottle, the lid at the bottle opening is still closed, resulting in a flat interface at both sides of the lid. However, this changes when the lid is opened. Since the heavier fluid is on top, the initial flat interface undergoes a number of deformations before the bubbles are formed. The instability that occurs at the interface between a dense fluid on top supported by a lighter fluid under gravity is called the Rayleigh-Taylor instability. A visual representation of the instability is depicted in figure 24a.

There is a complex evolution associated with the initial flat unstable interface. The growth of the instability consists of four different stages:

1. In the first stage, the perturbation amplitudes of the interface are small compared to the wavelength of the interface. The equations of motion can be analyzed using the linearized form of the equations of motion, resulting in the amplitude perturbations of the wavelength to grow exponentially with time. The perturbation retains its sinusoidal shape. How the linearized form of the equations of motion is obtained can be found through the works of Sharp, who provides a clear and detailed description of how he acquired the linearized form. [7]
2. During the second stage, non-linear effects start to appear and the beginning of the formation of the bubbles can be observed. The development is strongly influenced by the density ratio, namely the Atwood number $A = \frac{\rho_H - \rho_L}{\rho_H + \rho_L}$, where the subscripts H stands for the heavy and L for the lighter fluid. If $A \leq 1$, the light fluid moves into the heavy fluid layer in the form of bubbles. If $A \leq 0$, the heavy fluid starts to grow into the light fluid in the form of mushroom-shaped spikes. An overview of the different attempts to model the nonlinear growth of spikes and bubbles is also provided and discussed by Sharp. [7]
3. The nonlinear terms can not longer be ignored in the third stage. The bubbles starts to interact and merge with each other, resulting in large bubbles that move faster into the heavier fluid.
4. In the final stage, a region of turbulent mixing of the two fluids has been developed.

Numerous factors influence the development of the Rayleigh-Taylor instability. Examples include surface tension, viscosity and the prior discussed Atwood number.

2.1.3 Bubble shape

After the initial interface is deformed into the first shaped bubble, the terminal rise velocity of the bubble, the bubble shape and the trajectory of the bubble in free space are all dependent on the fluid properties. Clift made a shape regime map based on the characteristics for bubbles and drops in unhindered gravitational liquids. [8] This shape regime map is displayed in figure 3 and is only applicable when the density and viscosity ratios are small, such as air bubbles in water. The map is dependent on three dimensionless parameters, the Morton, Eötvos and terminal Reynolds number, where these three dimensionless parameters each describe a bubble characteristic. The Morton number is used to describe the liquid phase properties, the Eötvos number measures the importance of deformation of the bubble due to the gravitational force on the surface tension and the terminal Reynolds number characterizes the terminal rise velocity of the bubble. Since the Reynolds number is the only number that contains the terminal rise velocity, figure 3 can also be used to estimate the terminal rise velocity in free space. However, more accurate correlations are usually available and will be discussed later in this literature review. The figure from Clift is mainly used to distinguish the different bubble shapes into their own regimes. Since liquid is flowing out of the bottle, while air is entraining into the bottle, it was found by Martin et al. that the bubble shape will become asymmetrical.[9]

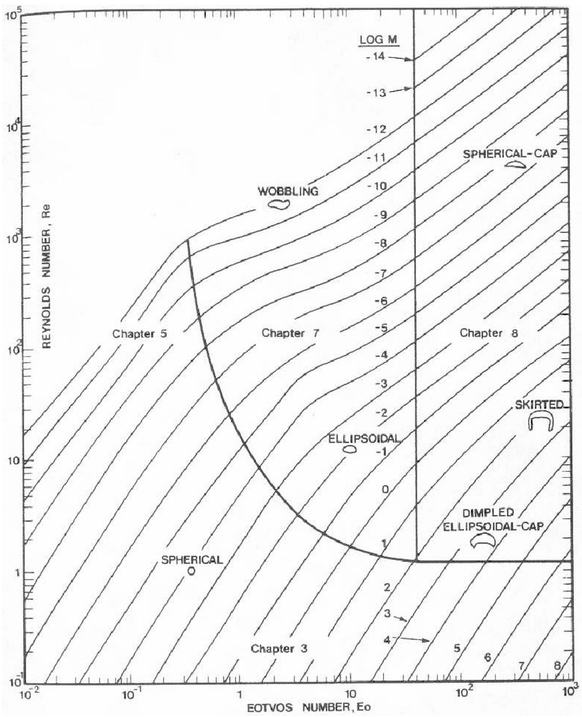

Figure 3: Behaviour of the bubble shape as a function of Eo, Mo and Re_T when ρ_d/ρ_c and μ_d/μ_c are small.[8]

2.1.4 Terminal rise velocity of Taylor bubbles

Figure 3 describes the air bubble in an unhindered liquid environment. However, in this study it is expected that the geometry of the PET bottle opening does influence the initial shape of the bubble and also the rise velocity. Thus, looking at bubble entrainment, where wall effects are considered, should give a better insight on the behaviour of the bubbles in the bubble regime than the figure designed by Clift.

When assuming the case for a Taylor bubble, that rises in a stagnant ideal fluid in a vertical tube, the terminal rise velocity of the bubble can be determined with the dimensionless Froude number shown equation 1. Theoretical and experimental results have shown that the dimensionless Froude number has a constant value when determining the terminal velocity of the bubble. Dumitrescu theoretically derived that this constant value was equal to $Fr = 0.351$ and experimental data provided for cylindrical air bubbles that the constant value was $Fr = 0.346$. [10] Davies and Taylor estimated that the value of the dimensionless parameter to be $Fr = 0.328$ and proved it with their experimental data. [11] White and Beardmore validated the results of Dumitrescu. However, they found in general that the Froude number is a function of the dimensionless inverse viscosity N_f and the Eötvos number. [12] Viana found that when surface tension is negligible, thus for $Eo > 40$, the Froude number is only dependent on the inverse viscosity. The Froude number is then related to the inverse viscosity number as: [5]

$$Fr = 0.34\left[1 + \left(\frac{31.08}{N_{\mathrm{f}}}\right)^{1.45}\right]^{-0.71} \tag{6}$$

The fluid behaves as an ideal fluid when $Eo > 70$ [12] , which results that the dimensionless Froude number is equal to $Fr = 0.345$. This can also be observed in figure 4. For a value of above 70, the Froude number does not change. From figure 4, it can also be seen that the zero velocity criteria for the bubble has been reached when $Eo \leq 4$.

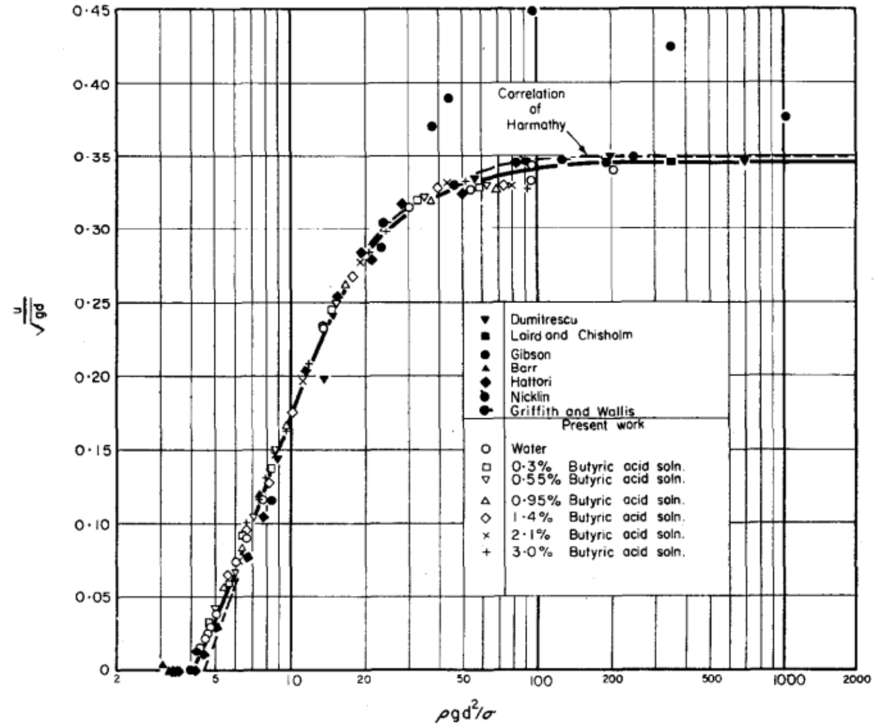

Figure 4: Results for cylindrical air bubbles rising in water and dilute solutions contained in vertical pipes, depending on the Froude and Eötvos number[12]

The critical value of 4 can be theoretically explained with a simple pressure balance analysis. When the terminal rise velocity of the bubble goes to zero, it can be assumed that the bubble will get in contact with the wall. When considering the wall to be hydrophylic, the top bubble interface will act as a meniscus with a maximum curvature of $\frac{2}{d/2}$, where d is the diameter of the glass pipe, and the bottom bubble interface act as a flat cylinder with a minimum curvature of $\frac{1}{d/2}$. This means that the difference in Laplace pressure has to be balanced by the hydrostatic pressure over a height of $\frac{d}{2}$:

$$\rho g \frac{d}{2} \sim \frac{2\gamma}{d}$$

From this simple analysis, it can be concluded that the zero velocity criteria is satisfied when it is in the order of magnitude $Eo \leq 4$.

When the viscous, inertial and surface tension forces all are significant, it takes three different independent dimensionless groups to obtain a correlation to determine the rise velocity. A general correlation for the terminal rise velocity for the bubble was found by White and Beardmore[12] and is given in figure 5, where the figure depends on the Froude, Eötvos and Morton number. Since only the Froude number contains the terminal rise velocity term, whereas the other two dimensionless parameters only contain fluid properties, it is straightforward on how to determine the terminal rise velocity through figure 5.

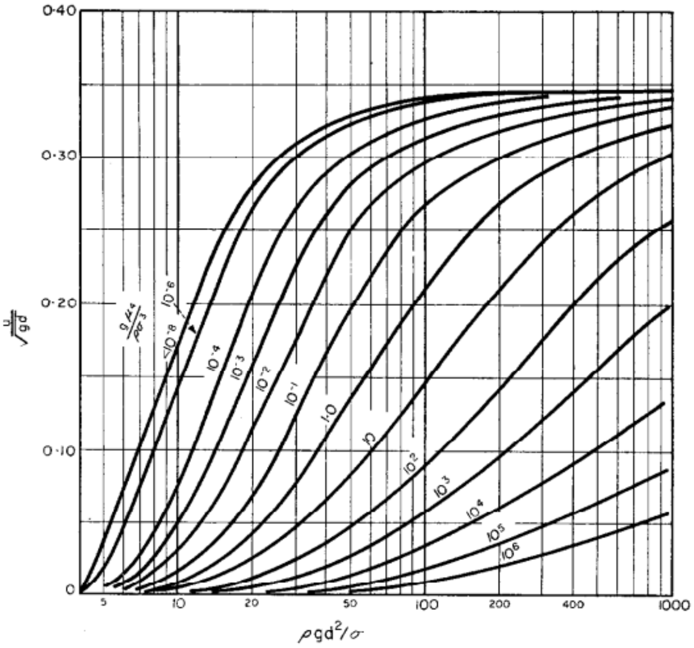

Figure 5: General correlation for the rise velocity of cylindrical air bubbles in liquids in vertical tubes[12]

White and Beardmore also specified different regimes for the different values of the three dimensionless parameters. These are depicted in figure 6, where the seven regimes are based off on the conditions under which the various retarding forces may be neglected. For example, the rising velocity of the Taylor bubble is independent of the viscous forces in region 2, whereas in region 3 the velocity is independent of the surface tension forces.

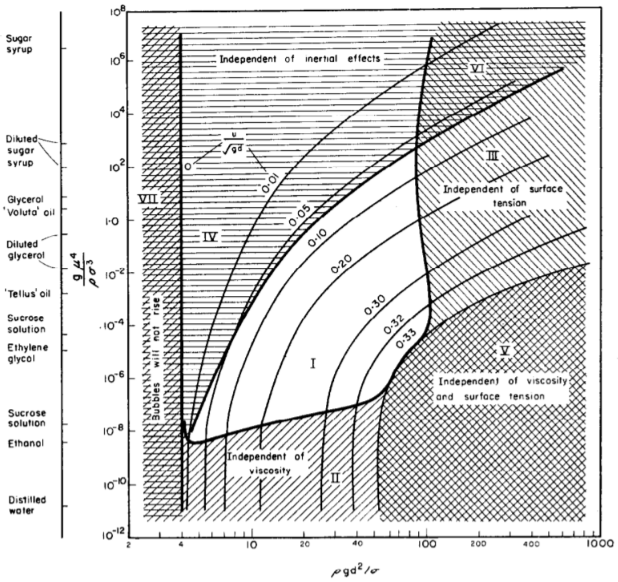

Figure 6: Crossplot of data, showing regions in which the effect of certain parameters becomes unimportant [12]

The graphs and equations described above are valid in stagnant fluids. However, in the case of a draining bottle, the fluid is not stagnant, due to the fluid flowing out of the bottle. Thus, an extra term should be added to account for the difference in terminal rise velocity. The terminal rise velocity in stagnant fluid $u_{T,0}$ can be rewritten through the Froude number as

$$u_{T,0} = k\sqrt{gD_e} \tag{7}$$

where k is the critical value of the Froude number. For a Taylor bubble rising in a moving liquid, the rising bubble velocity u_T can be determined as a function of its rise velocity in a stagnant fluid and the contribution due to the mean liquid velocity U_l: [13]

$$u_T = Cu_l + u_{T,0} \tag{8}$$

The value of constant C displayed in equation 8 depends on the velocity profile of the liquid and the bubble and can be seen as the ratio between the mean and maximum velocity of the profile. For turbulent flows is $C \cong 1.2$, whereas for laminar flows $C \cong 2$ is valid. [14]

2.1.5 Flooding, slugging and air-entrainment into bottle

Since research on the drainage time for the specific case of a filled bottle was very scarce, this section will elaborate on most of the research that was found on this particular topic.

A specific experimental study has been performed to analyze the fluidics during the emptying of a bottle. This was done by Rohilla and Das [15], where they tried to visualize the fluid dynamics of bubbles entering the bottle and liquid flowing out of the bottle. They also tried to find the optimal drainage time with absence of rotation by altering the viscosity and the inclination of the bottle.

They found that the bottle emptying dynamics could be sorted into five stages on the basis of their distinct flow features, which are discussed below.
Stage 1, Air entry into the bottle: When the bottle is suddenly opened, the liquid inside the bottle starts to flow out, while simultaneously the air wants to penetrate into the bottle in the form of a gaseous finger. This results in the formation of an annular falling liquid film around the rising air bubble. When the bottle is straight-up, the bubble is symmetric, whereas the gaseous finger is asymmetric when the bottle is inclined. The complete establishment of the bubble marks the end of stage 1.
Stage 2, Bubble growth in the conical section: The bubble starts to expand radially as well as axially when entering the conical section of the bottle due to the continuously feed of the air outside. The annular film starts to collapse, which causes the air bubble to pinch off from the outside air.
Stage 3, Post pinch-off bubble: The exact location of the pinch-off is different for different viscosities of fluids. For water this is outside of the bottle, however for more viscous fluids such as glycerol, the pinch off occurs in the bottle opening. The collapse of the air bubble is driven by the hydrostatic pressure. Wrapping up of the air bubble in the bottle marks the end of stage 3.
Stage 4, Journey of the bottom end of the bubble: Wrapping the bubble up results in a streamlined discharge of the liquid. During this stage, only liquid is present at the bottle opening. Towards the end of this stage, the discharge of the liquid gets interrupted again by the rushing of outside air into the bottle. This results in the thinning of the liquid at the bottle mouth.
Final stage, Bubble evolution in the conical section: The last stage involves the formation, growth and disintegration of the ejector jet inside the pinched-off bottle. The ejector jet gets produced due to the collision of capillary waves in the collapsing bubble rear end. This ejector jet collides with the top of the bubbles, accelerating the free rising bubble inside the bottle. The leading bubble also effects the growth of the trailing bubble due to the oscillation triggered by the collision of the ejector jet.

The phenonema described above where the gas phase is flowing upwards and the liquid phase downwards is often described in the literature as flooding [16]. Slugging is for the specific case characterized by the presence of large bullet-shaped bubbles. Davies and Taylor [17] derived an equation for tubes which are of diameter $\geq$ 10 mm to determine the rising velocity of these gas slugs U_p:

$$U_p = 0.35\left(\frac{gd(\rho_l - \rho_g)}{\rho_l}\right)^{1/2} \tag{9}$$

Also different experiments were tested by Whalley [18] to see which parameters had influence on the drainage time. He found that using hot water had a significant effect on the emptying time: the hotter the water, the lower the emptying would be. Extending the bottle neck also resulted in a decrease of the emptying time. By inclining the bottle, Whalley found that the emptying time could be shortened, where the minimum emptying time occured at an angle of about 30°-45°to the vertical axis, whereas Rohilla and Das [15] found that the minimum emptying time had an asymptote at around 20° from the vertical axis. Whalley also observed that if he initialized the fluid with a certain swirl velocity, the emptying times were greatly affected. However no attempt was made by him to scientifically test the effect of swirl and publish the results.

Also, a general scaling law for the emptying time $t_{d,0}$ of cylindrical bottles with initial liquid level h and diameter of the bottle d_b was found and derived by Clanet and Searby [19]:

$$t_{d,0} \simeq 3.0 \frac{h}{\sqrt{g d_b}} d*^{-5/2} \tag{10}$$

where $d* = d_h/d_b$ is the normalized neck diameter, with d_h the bottle opening diameter. With this law, Clanet and Searby emphasized the fact that the geometrical ratio of the bottle neck diameter to the bottle diameter $d*$ played an essential role in the emptying dynamics of the bubble regime. How the emptying time in equation 10 is derived, can be explained with the volumetric flow rate Q in the bottle opening and the terminal rise velocity:

$$Q_{liquid} = Q_{air} = \frac{1}{4}\pi u_T d_h^2 \tag{11}$$

where u_T is the terminal rise velocity of a Taylor bubble, defined in equation 7, and d_h the bottle opening diameter. In the limit of the bubble diameter $d = d_h$, it is found by White and Beardmore [12] that $k = 0.34$, resulting in $u_T = 0.34\sqrt{g d_h}$. Since the volume of the liquid in the top bottle is defined as $V_{bottle} = Q_{liquid} t_{d,0}$, where $t_{d,0}$ is the emptying time of the bottle without rotation, the derivation of the emptying time is straightforward:

$$\begin{aligned} t_{d,0} &= \frac{V_{bottle}}{Q_{liquid}} \\ t_{d,0} &= \frac{\frac{1}{4}\pi d_b^2 h}{\frac{1}{4}\pi u_T d_h^2} = \frac{h}{u_T}\left(\frac{d_b}{d_h}\right)^2 \\ &= \frac{1}{0.34}\frac{h}{\sqrt{g d_h}}\left(\frac{d_b}{d_h}\right)^2 \simeq 3.0 \frac{h}{\sqrt{g d_b}}\left(\frac{d_h}{d_b}\right)^{-5/2} \end{aligned} \tag{12}$$

Equation 10 is a key result for this study, since the non-dimensional total drainage time $t*$ is the ratio between the drainage time and the drainage time for a stationary case (equation 10). In equation 10, the value of k is specifically for an air-water system. By testing the Morton and Eötvos numbers, the fluid properties will be altered, so the value of k and thus the value of the stationary drainage time will also change.

2.2 Drainage from an open reservoir in presence of rotation

After the review on the bubble regime, this subsection will discuss the effects of rotation on the fluid for an open reservoir. Many research efforts have been done in the literature to understand and describe the free-surface vortex in a rotating open reservoir. As a result of a lack of under-pressure generation in open containers, bathtub vortices will appear at relatively small angular velocities compared to closed containers.

2.2.1 Pressure behaviour in the air-layer

In the introduction of this subsection, it was stated that an under-pressure in the bottle prevents the liquid feed to flow continuously out of the bottle. Instead, a pulsating behaviour is noticed consisting of air bubbles that are entrained into the bottle. Before the free-surface vortex will be elaborated in this section, first the importance and the difference between an open reservoir and closed reservoir has to be discussed.

An open reservoir is defined as a geometry where a drain port is realized at the bottom and no end wall is present at the top. Therefore the pressure at the top and at the bottom is equal to the atmospheric pressure. This is illustrated in figure 7a, where at position 1 and 4, the pressure is equal the atmospheric pressure. Therefore, no pressure difference is present to entrain air into the geometry, resulting in an undisturbed liquid flow out of the geometry. However, for an closed reservoir, only a drain port is present at the bottom of the geometry. From a simple pressure analysis, the pressure difference can already be obtained. For the case with a closed geometry, the pressure difference between point 1 and 4 depicted in figure 7b is defined as:

$$\begin{aligned} p_1 &= p_2 = p_{atm} && \text{(zero curvature of the interface)} \\ p_2 &= p_3 + \rho g h && \\ p_3 &= p_4 && \text{(zero curvature of the interface)} \\ p_{atm} &= \rho g h + p_4 && \end{aligned} \tag{13}$$

From the calculation in 13, it can be observed that the pressure in the air layer at the top of the bottle is lower than atmospheric pressure. This results in the under-pressure sucking the air-bubbles into the bottle, preventing the continuous liquid feed and the formation of the air-core vortex for low angular velocities.

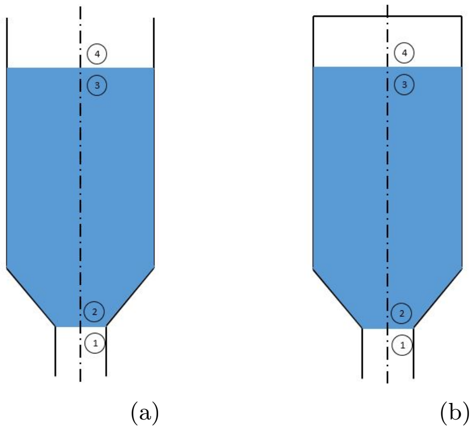

(a) (b)

Figure 7: Simplified view of the top bottle a) open reservoir b) closed reservoir

2.2.2 Anatomy of the free-surface vortex

Most of the previous studies investigating the free-surface vortex have had the same experimental setup where a fluid flow is initialized by a rotating container.[20] The drain hole at the bottom of the container will be opened after a certain time period, where the free-surface vortex will be generated and the outflow is driven by gravity. In literature, the free-surface vortex for low angular velocities is also sometimes defined as bathtub vortex. The evolution of the bathtub vortex is dependent on the rotational velocity. A small dimple on the free surface will appear with small rotation rate. By increasing the rotational velocity will the surface depression increase and a needle-like shaped dimple will appear growing into the drain hole. By further increasing the angular velocity, the dimple (air-core) will fully stretch into the drain hole. This is then defined as an air-core vortex.

Experimental studies have shown that the flow structure of the bathtub vortex is surprisingly complex. However, the flow can still be divided into three general regions. In the interior of the fluid, far away from the boundaries, the flow has no variation in the direction of the rotation vector. In the case of the bathtub vortex, the vertical direction. This is explained through the Taylor-Proudman theorem, that states that in a steady, inviscid, homogeneous rotating flow, the rotating flow is purely two-dimensional and thus behaves like a solid body rotation. This region, called the bulk flow, is balanced between the centrifugal force and pressure gradient, which is called the geophysical balance. More about the centrifugal force and the Taylor-Proudman theorem will be discussed in chapter 2.2.2.1 and chapter 2.2.2.2, respectively. Near the wall regions where the centrifugal and pressure gradient can not be balanced by each other, different shear layers are being formed on the bottom and on the sides of the container. In these layers, a balance between the centrifugal and viscous forces is noticed. In the bottom boundary layer it is noticed through experimental visualization that the fluid spirals inwards. Close to the drain hole, a large part of the fluid is directed upwards and goes down with the rest of the core, while the rest of the fluid goes directly down the drain. This phenomenon is called Ekman pumping. [21]

2.2.2.1 Centrifugal and Coriolis force

When looking in the theory of the bathtub vortex, the force balance inside the fluid is one of the important aspects in understanding the vortex phenomena. It is important to know when working with rotation and vorticity, in what kind of frame of reference the fluid flow is described in. Newton's laws of motion describe the motion of an particle or object in an inertial frame of reference. However, a proper analysis of rotating fluid flows is more convenient when it is carried out in a co-rotating frame of reference. although additional terms are needed to fully describe the Navier-Stokes equations. These forces are the centrifugal and the Coriolis force and are called pseudo or fictitious forces [22], as they do not arise from any physical interaction between two objects but rather from the acceleration of the non-inertial frame itself. The Coriolis force acts perpendicular to the axis of rotation, while the centrifugal force acts outwards in the radial direction.

The relation between the inertial and rotating frame of reference (denoted as subscript I and R respectively) is denoted below

$$\left(\frac{d\mathbf{r}}{dt}\right)_I = \left(\frac{d\mathbf{r}}{dt}\right)_R + \mathbf{\Omega} \times \mathbf{r} \tag{14}$$

where the vector notations are displayed as bold symbols, the rotating frame of reference is rotating with an angular velocity of $\mathbf{\Omega}$ and the position vector is defined as $\mathbf{r}$. Equation 14 can also be described as

$$\mathbf{u}_I = \mathbf{u}_R + \mathbf{\Omega} \times \mathbf{r} \tag{15}$$

The full Navier-Stokes equation in the rotating frame of reference is described as

$$\frac{\partial \mathbf{u}}{\partial t} + (\mathbf{u} \cdot \mathbf{\nabla})\mathbf{u} + 2\mathbf{\Omega} \times \mathbf{u} = -\frac{1}{\rho}\mathbf{\nabla} P + \nu \mathbf{\nabla}^2 \mathbf{u} \tag{16}$$

where $P = p - \frac{1}{2}\rho\Omega^2 r^2$ is the reduced pressure at a certain distance r from the rotating axis and $2\mathbf{\Omega} \times \mathbf{u}$ is the Coriolis acceleration.

It is commonly believed that the direction of the bathtub vortex is influenced by the Coriolis force due to the rotation of the earth. This may be indeed true for large-scale geophysical flows. However, in the case of small-scale phenomena such as the bathtub vortex, this is not always valid. Shapiro conducted experiments to investigate the Coriolis effect on the bathtub vortex and found indeed that only in extremely controlled conditions the counter-clockwise rotation during water draining was noticed.[23] He stated that the Coriolis effect was negligible due to the other effects simply being larger, such as initial fluid motion and non-uniformity of temperature inside the fluid. Tyvand and Haugen also found that the rotation of the earth cannot have a significant influence on the bathtub vortex.[24] They stated that the time scale of the generation of the bathtub vortex is much shorter than the time scale of the earth's rotation. The smallest net motion should already determine the direction of the vortex. In contrast to the Coriolis force does the centrifugal force play a key role in the generation of the bathtub vortex. It is expect that the centrifugal force should balance the radial pressure gradient in the liquid layer.

2.2.2.2 Taylor-Proudman theorem

At the beginning of this section, the Taylor-Proudman already got introduced. The Taylor-Proudman theorem states that for a steady, rotating, inviscid, homogeneous flow, the fluid velocity will be uniform along the axis of the rotation vector. To make the Taylor-Proudman theorem valid, the Coriolis term has to be larger than the non-linear and viscous terms (far from the wall) for rapidly rotating flows, which means that the Rossby number has to be sufficiently small ($U \ll \Omega L$).[25] Under these conditions, the momentum equation reads

$$2\mathbf{\Omega} \times \mathbf{u} = -\frac{\nabla p}{\rho} \tag{17}$$

By taking the curl on both sides,the following is obtained

$$\nabla \times (\mathbf{\Omega} \times \mathbf{u}) = 0 \tag{18}$$

and by simple mathematical manipulation, assuming that the rotational velocity Ω is constant and by using the continuity equation ($\nabla \cdot \mathbf{u} = 0$), the following is obtained:

$$\mathbf{\Omega} \cdot \nabla \mathbf{u} = 0 \tag{19}$$

$$\Omega_x \frac{\partial \mathbf{u}}{\partial x} + \Omega_y \frac{\partial \mathbf{u}}{\partial y} + \Omega_z \frac{\partial \mathbf{u}}{\partial z} \tag{20}$$

Now choose a coordinate system where the rotation of axis of the vortex is only around one single axis, for example the z-axis. Thus, where $\Omega_x = \Omega_y = 0$, we obtain that

$$\Omega_z \frac{\partial \mathbf{u}}{\partial z} = 0 \tag{21}$$

which means that the velocity field does not vary in the z-direction, if $\Omega_z \neq 0$. Thus, the Taylor-Proudman theorem states that for the geostrophical bulk velocity in the bathtub vortex, the fluid flow will be independent of the vertical axis and that the fluid flow will behave as a solid body rotation.

2.2.3 Shear layers

In the Taylor-Proudman theorem, it was assumed that the fluid flow was inviscid and that solid body rotation should be realized everywhere in the rotating container. However, this changes in the case when the viscosity can not be neglected. When a fluid passes over a solid boundary, a shear layer will develop due to the no-slip condition. However, the relation for the shear layers are different for a rotating flow and will be discussed in this subsection.

2.2.3.1 Ekman layer

The Ekman layer has been a familiar concept in geostrophysics and the theories by Ekman can be applied on geostrophical currents, where the viscous forces start to play an important role. The Ekman layer is known to play an important role in circular vortices such as the bathtub vortex, where the Ekman layer is one of the boundary layers in the rotating systems. These layers will start to develop on the bottom and sometimes on the top of the cylinder if the cylinder is fully filled.

To determine how high the thickness of the Ekman boundary layer is, an order of estimate is done where the friction force is assumed to be in the same order as the inertial force in the Ekman layer:

$$\frac{\nu}{\Omega \delta^2} \sim 1 \tag{22}$$

which leads to the boundary layer thickness δ:

$$\delta \sim \sqrt{\frac{\nu}{\Omega}} \tag{23}$$

In a typical rotating tank experiment with water as the rotating fluid, where $\nu = 10^{-6}\,\mathrm{m^2s^{-1}}$, $\Omega = 1\,\mathrm{s^{-1}}$, the Ekman layer thickness is in the order of 1 mm. As can be seen from equation 23, the depth scale of the Ekman layer in rotating fluids can be characterized by a fixed thickness. For equation 23 to be valid to estimate the boundary Ekman layer, a few conditions have to be satisfied.[26] First of all, the fluid is assumed to be bounded below by a solid surface. Also, the Rossby number has to be assumed relatively small, so that the motion will behave as a solid body rotation. Another condition that has to be applied, is that the initial height of the fluid is sufficiently large. This means that the Ekman number is also relatively small. The Rossby and Ekman number can be found in equation 32. Also, no excessive perturbations or oscillations should be present in the vortex flow. If all these conditions are applicable, equation 23 is valid to describe the Ekman boundary layer.

Next to the boundary thickness of the Ekman layer is the behaviour of the fluid velocity in the Ekman layer also important to mention. It is considered that the fluid velocity in the Ekman layer is only a function of the z-coordinate in the Cartesian coordinate system.[27] When considering a uniform flow in one direction above the Ekman layer, such that $\mathbf{u}_G = (u, 0, 0)$, then as z increases from zero to the top of the Ekman layer δ, the velocity profile in the Ekman layer will behave as a spiral, as depicted in figure 8.

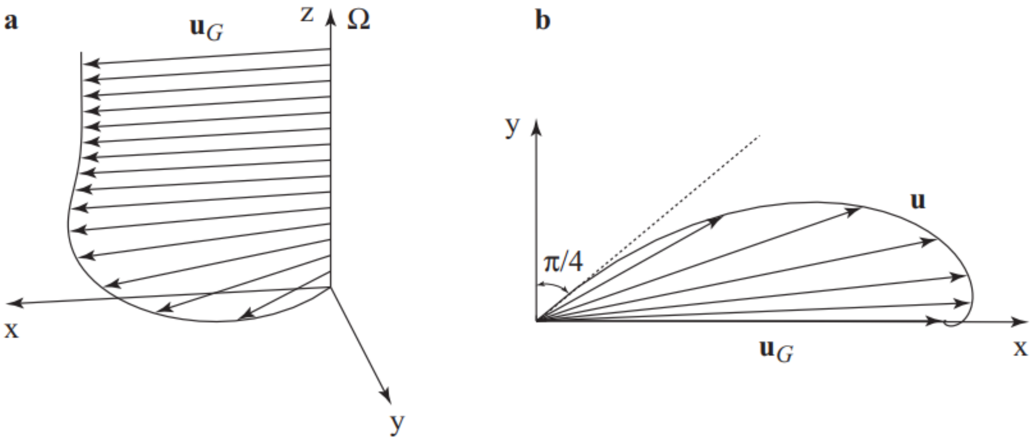

Figure 8: Ekman layers ($\Omega > 0$). (a) The velocity profile $\mathbf{u}(z)$. (b) The Ekman spiral projection on the (x, y)-plane. [27]

To understand why this Ekman spiral exists, the following simple model is used, where the velocity vector is described in cylindrical coordinates (r, θ, z). Consider a viscous fluid in a rotating cylinder with kinematic viscosity ν and with a uniform velocity $\mathbf{u}_G = (0, v_G, 0)$ above the Ekman layer ($z > \delta$). The fluid velocity in the Ekman layer is independent of θ and is defined as $\mathbf{u} = (u(r, z), v(r, z), 0)$. By solving the Navier-Stokes equations and applying the linear Ekman theory in the Ekman layer, the following is obtained

$$-2\Omega v = \frac{\partial}{\partial r}\left(\frac{p}{\rho}\right) + \nu \frac{\mathrm{d}^2 u}{\mathrm{d}z^2} \tag{24}$$

$$-2\Omega u = \nu \frac{\mathrm{d}^2 v}{\mathrm{d}z^2} \tag{25}$$

$$0 = \frac{\partial}{\partial z}\left(\frac{p}{\rho}\right) \tag{26}$$

The linear Ekman theory is only applicable in the region adjacent to the central core region. In the central core region, the non-linear terms must be included to model the bottom boundary layer close to the drain hole.[28] Since it is assumed that the vertical velocities are negligible, it follows from the axial Navier-Stokes equation 26 that the pressure is independent in the z-direction and thus the pressure gradient in the radial direction is equal in the bulk flow as in the Ekman layer. In the geostrophic bulk flow will the centrifugal force be balanced by the radial pressure gradient. However, in the Ekman layer can the centrifugal force not be balanced by the pressure gradient due to the extra viscous term in equations (24) and (25). Thus, radial inflow will happen in the Ekman layer due to the inbalance of the weaker centrifugal acceleration. With the boundary conditions $u(r,z) = v(r,z) = 0$ at $z = 0$ and for $z \to \infty$ $u(r,z) \to 0$ and $v(r,z) \to v_G$ the velocity profile in the Ekman layer can be described as [28]:

$$u(r,z) = -v_G e^{-z/\delta} \sin(z/\delta) \tag{27}$$

$$v(r,z) = v_G (1 - e^{-z/\delta} \cos(z/\delta)) \tag{28}$$

where δ is the height of the Ekman layer depicted in equation 23. For a detailed description on how these equations were obtained, the works by Andersen et al. is recommended.[28]

Another phenomena that should be mentioned is Ekman pumping. Lewellen found that the fluid flow right above the Ekman layer spirals upward around the axis of the direction of the vorticity close to the drain-hole. [29] A visualization with dye was done by Chen et al. and displayed in figure 9. [30] The mechanism which creates this upflow is called Ekman pumping. To explain the rise of velocity in the z-direction, the continuity equation in cylindrical coordinates will be used.

$$\frac{1}{r}\frac{\partial(ru)}{\partial r} + \frac{\partial w}{\partial z} = 0 \tag{29}$$

By using the boundary condition where $w(z) = 0$ at $z = 0$, it follows that [28]

$$w(r,z) = \frac{\delta}{2r}\frac{\mathrm{d}(rv_G)}{\mathrm{d}r}\big(1 - e^{-z/d}(\sin(z/\delta) + \cos(z/\delta))\big) \tag{30}$$

In the bulk of the fluid above the Ekman layer, thus in the limit of large z, the vertical velocity component w_G is defined as

$$w_G = \frac{\delta}{2}\omega_z \tag{31}$$

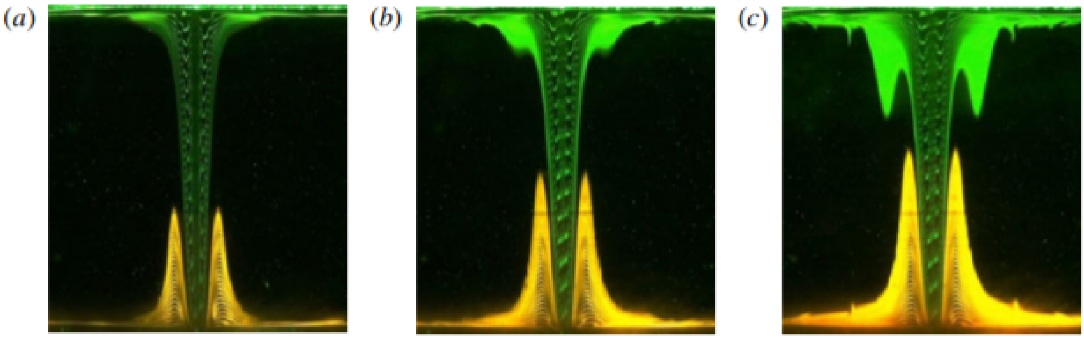

Figure 9: A sequence of flow visualizations for different time periods. The Ekman pumping is visualized with the yellow dye.[30]

This means that in the linear Ekman theory, the vorticity will give a rise to Ekman pumping. In the bathtub vortex, this will cause a weak upflow close to the central region, whereas the linear Ekman theory can not be applied in the central region where downflow is observed into the drain hole. The validity of the linear Ekman theory is only when the non-linear terms in the Navier-Stokes are negligible and the background rotation is weak, thus when the Rossby and the Ekman numbers are small. The local Rossby and Ekman numbers [31] are defined as:

$$\mathrm{Ro} = \frac{\omega - \Omega}{\Omega} \qquad\qquad \mathrm{Ek} = \frac{\nu}{2\omega r^2} \tag{32}$$

where ω is the local angular velocity of the fluid and Ω is the vorticity of the rotating cylinder and r the radius. Thus for non-linear instabilities to occur, the Rossby and Ekman numbers must be sufficiently large. Looking at equation 32, this is only valid when r is small.

In the final phase, right before the last part of the fluid is getting discharged, all fluid moves through the Ekman layer at the bottom, and accurate observations have shown that the direction of the flow can be reversed. [32]

2.2.3.2 Stewartson layer

Besides the horizontal Ekman shear layers, also vertical shear layers appear in rotating fluids. Stewartson was the first who could clearly describe the vertical shear layers in rotating fluids for low Rossby numbers.[33] He showed that shear layers would develop between two coaxial rotating planes where the center disks would rotate with a slightly different angular velocity than the rotating planes. Experimental investigation has also been done on a rotating disk with a finite radius placed in a cylindrical tank, where the cylindrical tank would rotate with a different angular velocity. They also showed the existence of the Stewartson layer.[34]

Stewartson found that the shear layer near the vertical wall is divided into two different sub layers. The main part has a thickness of $O(R_s^{-1/4})$ called the 1/4-layer, and the inner boundary layer located between the wall and the 1/4-layer, called the 1/3-layer whose thickness is $O(R_s^{-1/3})$, where $R_s = \frac{\Omega r^2}{\nu}$ with r the radius and Ω the angular velocity of the cylinder.

Hide suggested that the shear layer was dependent on the kinematic viscosity ν, the rotational velocity Ω and the initial height of the fluid H.[35] He derived an exact relation where the thickness of the Stewartson layer could be calculated as

$$\delta = 3H^{(1-2^q)}\left(\frac{\nu}{\sqrt{2}\Omega}\right)^q \tag{33}$$

with $q = 1/3$ for the 1/3-layer and $q = 1/4$ for the 1/4-layer, respectively.

Moore and Saffman [36] had a similar relation for the Stewartson layer. Their relation depended on the radius of the disk r and the Ekman number Ek:

$$\begin{aligned} \delta_{1/3} &= r\left(\frac{H}{r}\right)^{1/3} Ek^{1/3} \\ \delta_{1/4} &= r\left(\frac{H}{r}\right)^{1/2} Ek^{1/4} \end{aligned} \tag{34}$$

When considering a fluid flow with a free surface and thus only one Ekman boundary layer at the bottom, Andersen et al. found that the fluid flowing radially towards the wall due to the centrifugal force would be transported through the Stewartson layer downwards to the bottom Ekman layer.[28] The fluid was then transported radially inwards to the drain hole and discharged out of the rotating container. However, the vertical transport of the fluid is mainly done through the 1/4-layer, whereas the 1/3-layer is passive and no fluid enters the Ekman layer through the 1/3-layer.

2.2.4 Transient process of the bathtub vortex

The important flow phenomena and instabilities have been discussed in the previous subsections. Now it is important to understand how all the different forces and instabilities interact with each other during the draining process of the bathtub vortex.

In the case of a rotating cylinder with an open reservoir, only a small initial rotational velocity is needed to develop the bathtub vortex. This means that in this case the Rossby number is small. For very small Rossby and Ekman numbers, the inertial forces are small, and a geophysical balance in the bulk flow is maintained where the centrifugal force and pressure gradient force are in balance. Also, the friction forces are restricted to the boundary layers along the wall. Thus, $\mathrm{Ro} \ll 1$ and $\mathrm{Ek} \ll 1$, the vessel can be divided into three sub-regions, namely the Ekman layers at the bottom end-wall for a partial filled container, the Stewartson layer at the side wall, and the geostrophic bulk / interior fluid.

2.2.4.1 Spin-up

When the cylindrical container starts to spin and the valve at the drain port is still closed, a small thin shear layer of fluid forms around the walls of the cylinder. This shear layer will be influenced after a few rotations by the walls and the Ekman and Stewartson layers will start to develop. The timescale when the Ekman layer starts to form on the horizontal surface is when the Ekman spin-up time $t_{Ek} = O(1)$. The definition of the Ekman spin-up time is defined in equation 35. For the Stewartson layer, there are two basic stages in the transient development. When the time t_{Ek} satisfies $1 \ll t_{Ek} \ll Ek^{-1/3}$ an inviscid geostrophic stage occurs and a viscous stage is noticed until $t_{Ek} = O(Ek^{-1/3})$.[37] When the viscous forces are no longer negligible, thus when $t_{Ek} > O(Ek^{-1/3})$, the first Stewartson layer starts to form with a thickness of $O(Re^{-1/3})$. After some time will more parts of the fluid be influenced by the boundary layers and the rotating walls. This will in the end result in a solid-body rotation of the fluid. This transient process is called the spin-up.

However, to determine the exact moment when solid body rotation is achieved, two time-scales are important, namely the Ekman spin-up time and the radial diffusion time. The Ekman spin-up time depends upon the geometrical, kinematical and fluid parameters where the Ekman spin-up time is defined as:

$$t_{Ek} \sim Ek^{-1}\Omega^{-1} \tag{35}$$

The radial diffusion time depends on the parameters of the diffusion equation:

$$t_{dif} \sim \frac{a^2}{\nu} \tag{36}$$

When defining the dimensionless time parameter as $\alpha_0 = \frac{t_{Ek}}{t_{dif}}$, Watkins and Hussey [38] found that only for the case of $\alpha_0 > 1$, the diffusive time scale could accurately estimate the spin-up time. For the other cases, the solid body rotation is established much quicker, in the order of the Ekman spin-up time.[39] This is also the case for non-linear spin-up, thus for solid body rotations with big angular velocity differences. An example of non-linear spin-up is the spin-up of a stationary cylinder to a constant angular velocity, such as our case.

It is expected that during spin-up for a partial filled closed cylinder, the free surface at the top will deform in the form of a parabolic shape. A good visual representation is done experimentally by Basta et al. [40] and displayed in figure 10.

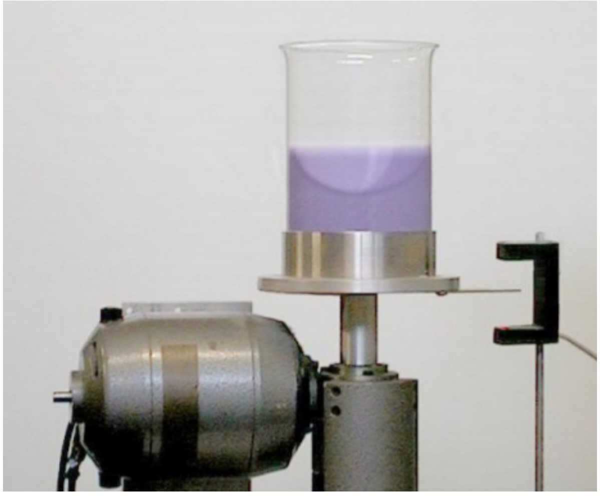

Figure 10: Experiment to visualize the parabolic free surface[40]

The shape of the surface can be explained with the Navier-Stokes equations. Consider a cylinder rotating around the z-axis, which is partly filled with liquid, the momentum equations are given as:

$$\frac{\partial P}{\partial r} = \rho\omega^2 r \qquad \frac{\partial P}{\partial \theta} = 0 \qquad \frac{\partial P}{\partial z} = -\rho g \tag{37}$$

By solving the equations given above, the following is obtained;

$$\begin{aligned} \rho\omega^2 r \mathrm{d}r &= -\rho g \mathrm{d}z \\ z(r) &= \frac{\omega^2}{2g} r^2 + h_0 \end{aligned} \tag{38}$$

where $r = 0$ in the center and $r = R$ at the wall, h_0 the height of the surface in the center and $z(r)$ is the height of the surface at a given radius. When looking at equation 37, it can be concluded that the height increases with a power of two and thus the surface indeed behaves as a parabola.

2.2.4.2 Drainage process (Spin-down)

When removing or opening the valve at the opening of the bottle, the fluid will start to flow out of the bottle, marking the start of the drainage process. After the draining starts, a dip is generated in the center of the free surface. The surface dip will be immediately pulled downwards and the depth of the surface dip is dependent on the rotational velocity of the liquid layer.

During the drainage process, the flow paths can be categorized into five different regions. (1) The first region is the fluid that flows over the bottom plate directly towards the drain hole through the bottom Ekman layer. (2) The second region is the fluid above the bottom Ekman layer that is subjected to the upward Ekman pumping, before it turns downwards to the drain hole. (3) The third region is the geostrophic bulk that is behaving as a solid body rotation. (4) The fourth region is the center vortex with the dimple and (5) the last region is the fluid next to the wall of the cylinder, which is the Stewartson layer. During the draining process will next to the first Stewartson layer also the second Stewartson boundary layer be formed with the thickness of $O(R^{-1/4})$.[37] The different regions are depicted in figure 11 to give a good visualization of the overall drainage process.

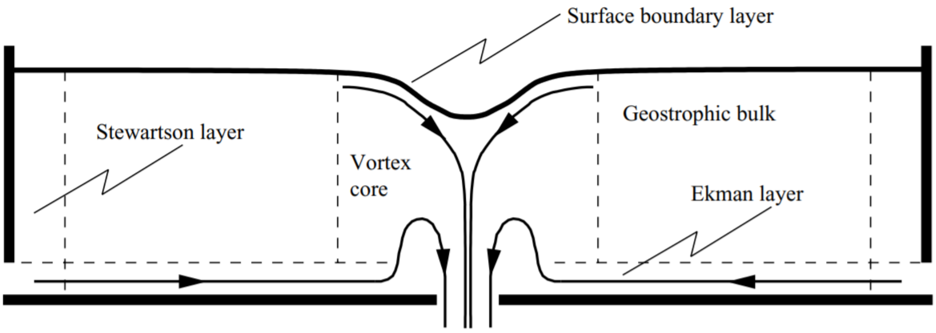

Figure 11: The characteristic flow regions of the bathtub vortex.[28]

2.2.5 Air-core vortex

It was found that for an open container, for a small rotation rate, a small dimple will appear on the free surface. The surface depression will increase by increasing this rotation rate until a needle-like shaped vortex will appear. At even higher values of the rotational velocity, air bubbles will detach from the tip due to vertical oscillations. When the rotation rate is increased further, the downward drag will become sufficiently large and overcome the buoyancy of the bubbles formed by the capillary instability and drag the bubbles downward. The air-filled core will then extend all the way down through the drain hole and a fully developed air-core vortex can be observed.[28]

A good visualization of the draining process with a fully-developed air-core is done by Son et al. depicted in figure 12.[41] 3D numerical results of the bathtub vortex were obtained, where the cylinder was initialized with a certain rotational velocity, until a steady-state was reached. At this point, the cylinder is stopped and the drain port at the bottom is opened.

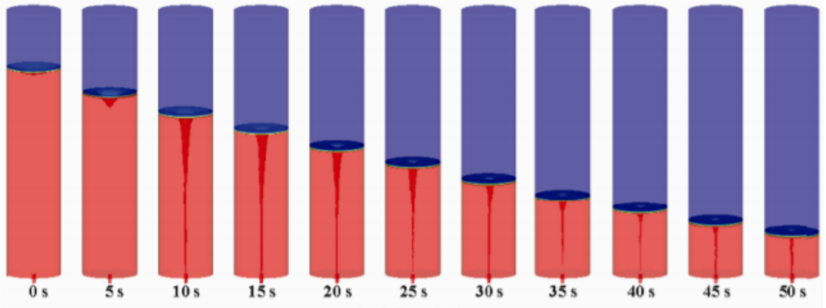

Figure 12: 3D numerical results of the progression of the free surface draining.[41]

When the air-core is fully developed, the under-pressure at the top of the bottle will disappear and atmospheric pressure is expected throughout the air-phase in the bottle. A good visualization of the pressure equality is done by Khoshkalam et al. and depicted in figure 13.[42] This is a key finding for this study, since the minimization of the drainage time is based on the pressure equality in the gas layer. As can be seen from figure 13, the pressure will be higher in the fluid at the bottom of the cylinder due to hydrostatic pressure, whereas the pressure will be uniform throughout the air phase. It is then expected that no difference will be noticed between the air-core vortices in the same geometry where the only difference would be the open and closed lid at the top of the geometry. Sohn et al. did experimental and numerical research for swirl and non-swirl flows with a drain port at the bottom and an open lid at the top (thus no under-pressure present). They found that in the case of non-swirl motion, the drain flow rate would decrease linearly. However, by initializing with a certain angular velocity, they obtained that the drain flow rate would decrease significantly due to the generation of the air-core vortex pushing the liquid to the side, preventing the liquid from flowing into the drain port.[43] Other instances of research have also shown that a fully developed air-core vortex would decrease the total outflow flux due to the narrowing of the discharging area.[20, 28, 41] Thus, in the case of the closed geometry, the air-core vortex should be generated to avoid the bubble regime, but the air entrainment should be as low as possible and the discharging area as big as possible to reach the maximum outflow and minimal drainage time. Also, it is expected that for a bigger liquid discharging area, the total effective friction due to wall effects will become smaller.

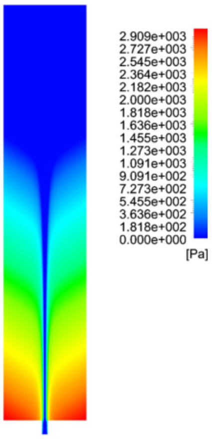

Figure 13: Pressure contour for a pre-rotated bathtub vortex in a fixed cylinder[42]

Several researchers have examined how to suppress or generate the air-core. Khoshkalam et al. found that the generation of the air-core vortex was independent of the wall geometry.[42] Sohn et al. investigated the air-core vortex as a function of the tank geometry and size. They found that the air-core vortex itself was affected by the tank rotation speed, tank size and the drain port size. Only the exact moment when the air-core vortex was observed in the simulation was independent of the tank size.[43] Ramamurthi and Tharakan found that during the liquid draining of the tank, the air-core vortex was strongly dependent on the size and shape of the drain port. A smaller diameter of the drain port would result in a larger draw down current, which means a faster generation of the air-core vortex. This was also confirmed by Sohn et al. where they found that the critical circumferential velocity to generate the air-core vortex increased exponentially as the drain port increases.[43] However, a smaller drain port diameter would mean that the effective area of the outflow would be smaller and thus decrease the outflow flux as well. Yukimoto et al. found through experimental and numerical results that the outflow through the drain hole is dependent on the rotational velocity. A smaller angular velocity would result in a higher outflow rate and vice versa.[44] Also, the influence of the temperature on the air-core vortex was studied. Properties such as the viscosity, surface tension and density change with the temperature. Nazir and Sohn investigated the influence of temperature and found that the temperature indeed influenced the drainage time.[45] From figure 14, it can be observed that a lower temperature would result in faster drainage time. It should be noted that figure 14 is for an open container, and thus the vortex regime is not a necessity to avoid the bubble regime. From temperatures of 10 °C and above, a fully developed air-core vortex was noticed. Below the 10 °C, it is believed that the flow regime would stay in the bubble regime for an closed container and thus increase the drainage time significantly. Since surface tension, density and viscosity all change with temperature, Nazir and Sohn both investigated which of these parameters had influence on the air-core vortex. They found that the appearance of the air-core vortex was unaffected by surface tension and density, while viscosity did indeed play a significant role. The viscosity of the fluid resist the motion of the fluid to move to the walls of the cylinder and thus reduce the flow mobility. The viscosity is low for high temperature cases, making it easier for the fluid flow to get pushed from the center and thus enhancing the generation of the air-core vortex. Thus, for the bottle case, the temperature of the fluid should not be too low, otherwise the air-core can not be generated.

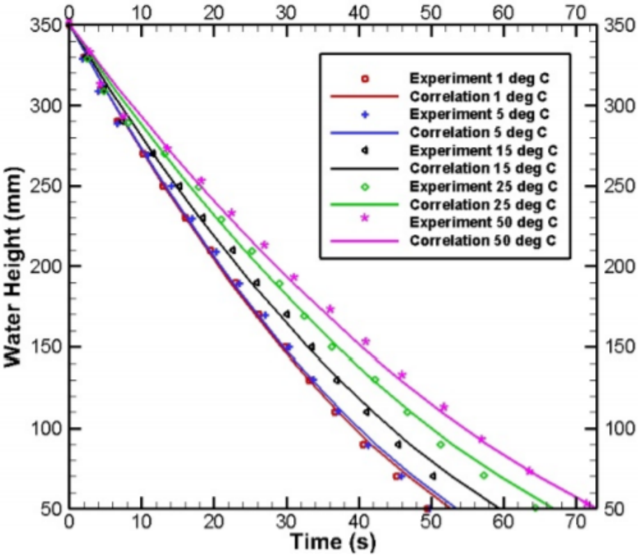

Figure 14: Experimental and correlation results for the height of the water level over time for different temperatures[45]

Other studies disagree with the statement that surface tension does not play a role in the generation of the vortex. Lundgren [46] and Anderson [28] both found that when surface tension is neglected, the surface depression of the air-core would reach the drain port faster than in the case when surface tension was included. Also, Khoshkalam et al.[42] found that when surface tension was present, the dip would become shorter and that the surface tends to prevent air to penetrate into the free surface. Thus, by decreasing the surface tension, it is believed that a fully developed air-core vortex is generated faster.

2.2.6 Critical submergence of the air-core vortex

When looking at air-core vortices in PET bottles, it is important to know when exactly the air-core vortex extends all the way down to the opening of the bottle. The flow regime will stay in the bubble regime, if the air-core vortex is not fully extended. Various studies have found different criteria / relations to predict the critical submergence of the air-core vortex in cylindrical geometries.

One of the first theoretical attempts to predict the condition when the critical vortex would appear was done by Odgaard.[47] He found a relation where he could estimate the critical depth of the liquid for different flow parameters and is depicted below:

$$h_c^2 = -0.9\frac{\gamma}{\rho g}\sqrt{\frac{u_z H_c}{\nu}} + 0.0043\frac{\Gamma^2 u_z}{g\nu} \tag{39}$$

where h_c is the critical submergence height, u_z the axial velocity near the drain hole and Γ the circulation. Odgaard based his model on the Rankine vortex model, where the radial velocity profile is linear, the axial velocity was determined through the continuity equation and the azimuthal velocity profile was expressed as a function of the radial position. By balancing the surface tension with the pressure gradient, he found the above relation to describe the free surface. However, equation 39 is only valid for a laminar core. When the vortex flow becomes turbulent, the eddy viscosity becomes more dominant. By replacing ν in equation 39 by the turbulent eddy viscosity ν_t, Odgaard proved that equation 39 can also be used for a turbulent core. The eddy viscosity is denoted as $\nu_t = \nu + k\Gamma$, where k is a factor of proportionality. Based on data provided in [47], the value of k is estimated to be $k = 6 \times 10^{-5}$. The relation stated by Odgaard was based on the assumption that the velocity field in the bathtub vortex was approximated by the Burgers vortex. However, the Burgers vortex equations can only be used when the free surface is planar, thus in the case when the dimple is small relatively to the total height of the fluid.[32] Even though the results of his criteria were in accordance with experimental results, the criterion is still inconsistent.

Another similar approach as Odgaard to theoretical determine the critical submergence was done by Hite and Walter. [48] The big difference in approach between Hite and Odgaard is that Hite modified the azimuthal velocity into:

$$u_\theta = \frac{\Gamma}{2\pi r_m}\frac{2\bar{r}}{1+2\bar{r}^2} \tag{40}$$

where u_θ is the tangential velocity, Γ is the constant circulation of the fluid, $\bar{r} = r/r_m$, r is the radius and r_m the radius at the maximum tangential velocity. He determined that for critical submergence, the highest azimuthal velocities should be at $r = 0$ and thus $\bar{r} = r/r_m \to \infty$ should be valid and determined that the relation for the critical submergence was equal to

$$h_c = \frac{1}{g}\left(\frac{\Gamma}{2\pi r_m}\right)^2 \tag{41}$$

Even though equation 41 agreed with their own experiments, the experiments were done in the regime where viscous terms and surface tension could be neglected.

Another theory of the bathtub vortex in a rotating vessel was done by Lundgren [46] and later further developed by Anderson [28]. He found that the order of magnitude of the depth of the central surface depression h_c is given by the following expression:

$$h_c = \frac{Q^2\Omega}{2\pi g\nu r_h^2} \tag{42}$$

where Q is the total flow rate, Ω the rotation rate of the container and r_h the radius of the drain hole. From the equation it follows that the central surface depression is more sensitive to the total flow rate than the rotation rate of the container. However, surface tension is neglected in equation 42, which causes equation 42 to overestimate the critical submergence of the air-core vortex. Baum and Cook carried out experiments and confirmed that indeed the surface tension plays a crucial role in the critical submergence of the air-core vortex.[2] To include surface tension, Anderson designed a numerical model, called the LABSRL-model to calculate the surface depression, where the surface tension and the viscous terms in the Ekman boundary layers was included. They also compared the LABSRL-model to real experiments and found that surface tension greatly affects both the whirlpool shape and its critical submergence.

Also, empirical relations have been obtained by studying experimental results of the bathtub vortices.[43, 49] Sohn et al. based it off on five non-dimensional parameters.[43] These non-dimensional parameters are the dimensionless critical distance and the diameter ratio of the tank to the drain port

$$L^* = \frac{H_i - h_c}{D} \qquad D^* = \frac{D}{d} \tag{43}$$

and the rotational Reynolds, Froude and Weber number

$$Re = \frac{\rho D^2\Omega}{\mu} \qquad Fr = \frac{D^2\Omega}{g} \qquad We = \frac{\rho D^3\Omega^2}{\gamma} \tag{44}$$

where H_i is the initial water height, h_c the critical submergence height, D the tank diameter, d the diameter of the drain port and Ω the initial rotational speed of the tank. With their numerical results, they obtained the following relation for the critical submergence

$$L^* = 83.339\big(D^{*-0.361}Re^{-0.00242}Fr^{0.222}We^{-0.346} - 0.0196\big) \tag{45}$$

Li et al. based it only of one dimensionless parameter, the Froude number.[49] The relation between the critical submergence H_c and the Froude number Fr is:

$$h_c = \frac{19921.84 + 7.54 \cdot \mathrm{Fr}^{7.06}}{573.81 + \mathrm{Fr}^{7.06}} \tag{46}$$

where the Froude number is defined as $\mathrm{Fr} = \frac{u}{\sqrt{gh}}$. The characteristic velocity u in the Froude number is the intake velocity, which could be attained by the intake diameter and by the flow rate. h is the total height of the fluid in the container.

The relation for the critical submergence of the air-core vortex depicted above where described for cases where nonlinear effects were ignored. However, when the Rossby number becomes larger, the nonlinear effects become more significant. Whitehead and Porter were one of the few that did research on these conditions.[50] They analyzed non-linear axisymmetric flow of an inviscid homogeneous fluid in a rotating cylindrical container. They found a relation where they could describe the free surface height h as a function of the radius r, $\dot{m}$ the total known mass flux and the potential head H:

$$g'h^3 - g'Hh^2 + \frac{\dot{m}^2}{8\pi^2 r^2} = 0 \tag{47}$$

where

$$H = h_1 + \frac{u_1^2 + v_1^2 + v_1 r_1 f + \frac{f^2 r_1^2}{2}}{2g'} - \frac{\left(v_1 r_1 + \frac{f r_1^2}{2}\right)^2}{2g' r^2} - \frac{f^2 r^2}{8}\left(\frac{1}{g'} - \frac{1}{g}\right) - \frac{f^2 r_1^2}{8g} \tag{48}$$

where h_1, u_1 and v_1 are the height and velocity in radial and azimuthal direction,respectively at the position of the source of fluid, $g' = \Delta\rho$, and $f = 2\Omega$ the Coriolis parameter.

2.2.7 Instabilities

As stated prior in the literature review, when the Rossby number becomes larger, instabilities can start to develop in the fluid flow. These instabilities can lead to a transition to weak turbulence. Studies have been performed to study the origin of these instabilities. These instabilities were explained with a lab experiment where a fluid was confined in a gap between two rotating cylinders. An example of the setup of these experiments is the experimental study on the different instabilities by Dherbecourt et al.[51] and is depicted in figure 15. The two cylinders would rotate with different angular velocities, resulting in different instability modes being observed. For low angular velocities is the fluid flow between these concentric cylinders steady, laminar and purely azimuthal. This state is referred as the Taylor-Couette flow in the literature.

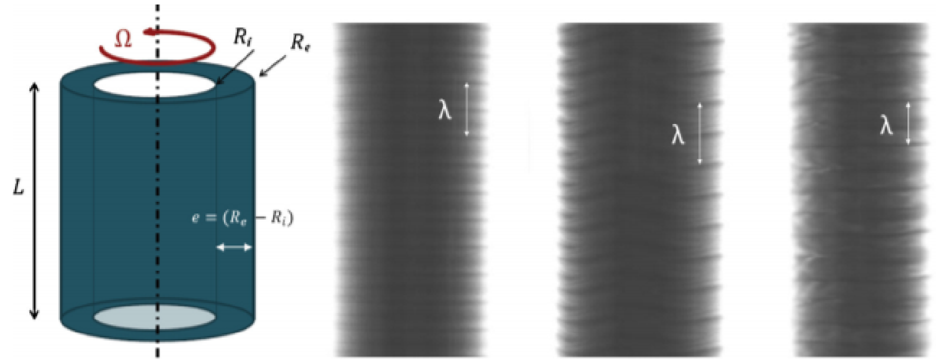

Figure 15: Left: Sketch of the experimental setup with water confined between two rotating cylinders. Right: Different flow instabilities due to the different rotational differences between the two cylinders.[51]

The criterion for when the flow becomes unstable in the absence of viscosity, was initially studied by Lord Rayleigh.[52] He found that the flow between two rotating cylinders would become unstable, if the inner rotating cylinder would spin faster than the outer rotating one. To summarize his criteria:

$$\frac{\mathrm{d}}{\mathrm{d}r}(u_\theta r)^2 < 0 \tag{49}$$

or

$$(r_i U_i)^2 > (r_o U_o)^2 \tag{50}$$

Thus, the fluid would become unstable if the angular momentum of the particle in the inner circle with a radius r_i and a velocity U_i would be larger than the particle at the outer circle with a radius r_o and a velocity U_o.

However, viscous forces tend to stabilize the fluid flow and damp the perturbations and turbulence. Thus, obtaining a dimensionless parameter containing the angular velocities and the viscosity might give a good insight on the development of these instabilities. Taylor found that when the angular velocity of the inner rotating cylinder was higher than a certain value (the critical Taylor number), an instability would occur where the flow would become unstable consisting of steady stacked axisymmetric counter-rotating vortices.[53] The instability grows further to un-axisymmetric perturbations by further increasing the rotational velocity. Azimuthal waves also start to develop on the vortex rings and eventually the flow becomes chaotic leading to a fully turbulent regime.[54] The Taylor-Couette flow becomes unstable, when the flow exceeds a certain value of the Taylor number. The Taylor number is a dimensionless parameter which characterizes the ratio between the centrifugal forces due to rotating of a fluid and the viscous forces. This dimensionless number is defined as:

$$\mathrm{Ta} = \frac{4\Omega^2 R^4}{\nu^2} \tag{51}$$

where R the characteristic length scale perpendicular to the rotating axis.

For the specific case when the fluid is between 2 concentric rotating cylinders, the Taylor number is defined as [55]:

$$\mathrm{Ta} = \frac{\Omega^2 R_i (R_i - R_i)^3}{\nu^2} \tag{52}$$

where $R_{i,o}$ are the radii of the the inner and the outer cylinder, respectively.

Another dimensionless parameter which combines the centrifugal force and the viscosity is the rotational Reynolds number. Large numbers of experimental and theoretical studies have been performed to study the critical transition value for when the fluid flow would become unstable through the Reynolds number. Andereck et al. determined transitions between different instabilities as functions of the inner and outer cylinder Reynolds numbers.[56] The Reynolds numbers are defined as:

$$Re_i = \frac{r_i (r_o - r_i)\Omega_i}{\nu} \tag{53}$$

$$Re_o = \frac{r_o (r_o - r_i)\Omega_o}{\nu} \tag{54}$$

where the subscripts i and o stands for the inner and outer, respectively, $Re_{i,o}$ the Reynolds number, $r_{i,o}$ the radii of the rotating cylinders and $\Omega_{i,o}$ the rotating velocities. The results of Andereck et al. about the different instability regions are depicted in figure 16.

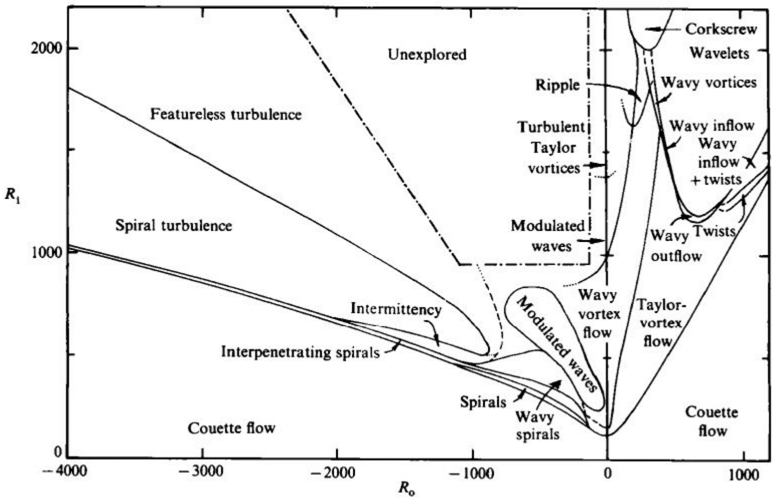

Figure 16: Regimes observed in flow between two rotating concentric cylinders by Andereck et al.[56]

The big difference between the experimental studies on the Taylor-Couette flow instabilities and this study, is that instead of an inner rotating cylinder, an air-core vortex is present. Taylor stated that by assuming the free-surface vortex as a virtual inner cylinder with a certain radius r_i and the cylindrical container with a radius r_o as the outer rotating cylinder, the theory stated in equation 50 and 52 is still applicable. [53] Mulligan found that in the presence of a free-surface vortex in a cylinder, instabilities such as the Taylor vortices would still appear. [57] He also proved that the instability mechanisms are indeed the same for two rotating cylinders as the free-surface vortex by considering Rayleigh's stability criterion.

2.2.7.1 Instabilities during spin-down

Before the instabilities can be analysed, first the time-frame when the instabilities starts to develop should be analyzed. In the case of the PET bottle, the spin-up process resembles the spin-up process for an open reservoir. It is expected that during the spin-up process, the difference in rotational velocity is not sufficiently large for instabilities to occur. When steady state is reached, which marks the end of the spin-up process, the bottle will be halted, the valve will be opened and the draining process will start. This draining process is referred as the spin-down process in the literature.[58]

The spin-down process occurs when the vessel abruptly stops rotating, while the fluid is still behaving as a solid body rotation. Similar to the drainage process of the open reservoir vortex, the Stewartson and the Ekman layer are present at the boundaries. However, the big difference between these two cases, is that during the spin-down process, multiple instabilities may occur.[58] As discussed before in chapter 2.2.7, instabilities will occur when the inner "cylinder" rotates faster than the outer cylinder. The inner "cylinder" (the air-core vortex) still rotates with a high rotational velocity, while the outer cylinder (the PET bottle) is stationary, which will indeed cause instabilities. Thus, when looking back at figure 16, the expected instabilities that should occur during spin-down should be where the outer rotating velocity is around zero and thus where the outer Reynolds number is $R_o = 0$.

Visualization on the spin-down process was done by Khoshkalam et al.[42] This is showed in figure 17. He tested two cases of the bathtub vortex, where in both cases the fluid was pre-rotated. The difference was that in one case, the side- and end-walls abruptly stopped rotating (spin-down), while in the other case the walls kept rotating at the same rotational velocity. As can be seen from the left side of the cylinder in figure 17, instabilities were noticed in the form of disordered vortices in the case of the stationary wall, while in the rotating wall (right side of the cylinder) no instabilities were noticed. Also, they found similarities between both cases. The tangential velocity profiles were very similar for small values of the ratio between the drain-port and the tank diameter r/R, thus proving that the sidewall rotation did not affect the air-core behaviour and the instabilities can only occur next to the central core.

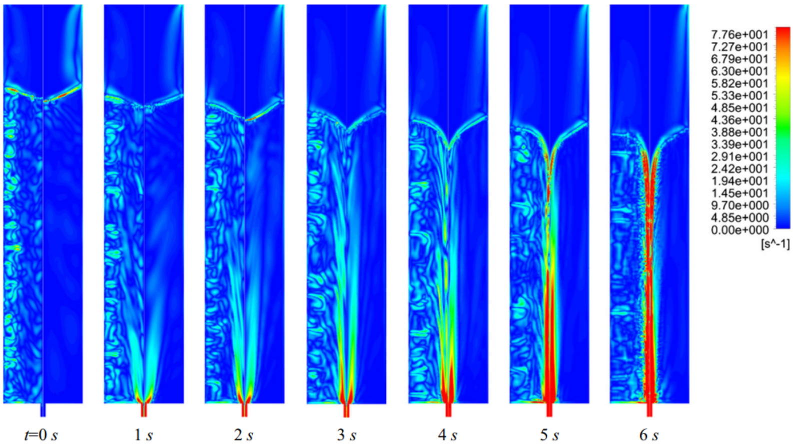

Figure 17: Tangential velocity contours at different times for a stationary wall (left) and rotating wall (right)[42]

Different instabilities consist of two modes. The first mode is the Taylor motion where waves move periodically in the axial direction and the second mode is a pattern of travelling periodic waves in the azimuthal direction. When increasing the angular velocity difference, the instabilities correspond to a combination of the two different waves in the flow. A good visualization of the different modes on the instabilities in the flow was numerically done for different Reynolds numbers by Dutta and Ray [59] and depicted in figure 18. As can be seen from figure 18, the flow for $Re = 177$ consists mainly out of Taylor waves in the azimuthal direction (Taylor vortex flow), whereas for $Re = 505$ that flow consists of both wave modes (wavy Taylor vortex flow).

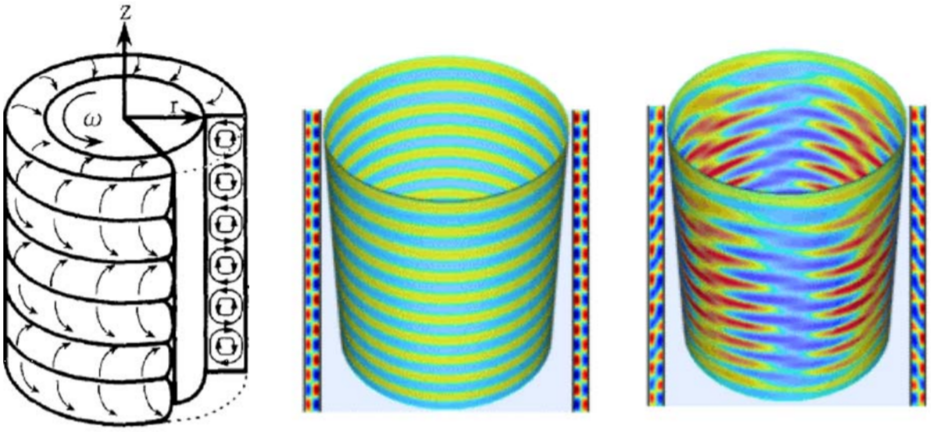

Figure 18: The flow configuration of different wave modes. The left picture describes the flow configuration of Taylor vortices. The middle and right pictures are numerical solutions for $Re = 177$ and $Re = 505$ by Dutta and Ray.[59]

Takeda also did an experimental and numerical study on the instabilities of the Taylor-Couette flow. However, the main focus of his study was to investigate the instabilities at higher Reynolds numbers.[54] The displayed Reynolds values depicted in figure 19 are the reduced Reynolds numbers defined as $Re* =$

Re/Re_c, where Re is the real Reynolds number and Re_c is the critical Reynolds number where instabilities start to occur.

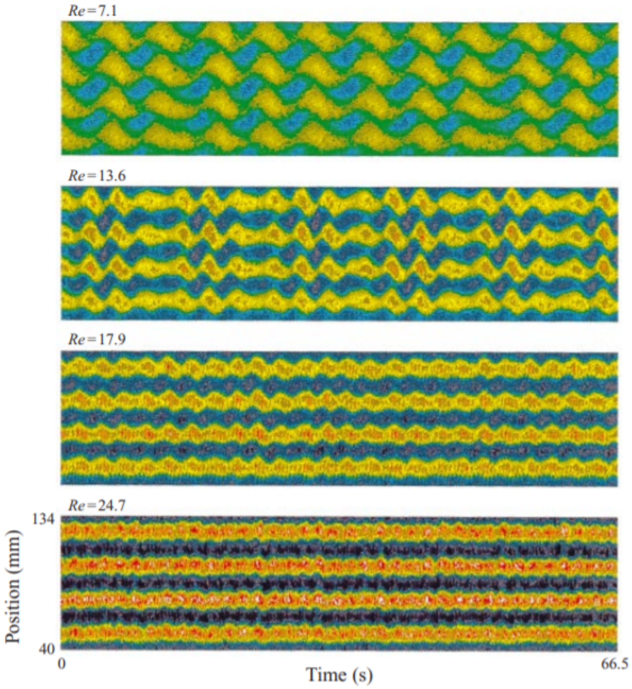

Figure 19: Measured velocity fields for different Reynolds numbers, where the outer Reynolds number is zero. Red-yellow is for positive and blue-green is for negative velocities.[54]

From figure 19, it can be seen that there is a clear distinction between the different regimes for $Re_o = 0$. The different regimes are defined in figure 16. The wavy vortex is at $Re* = 7.1$, the modulated wavy vortex flow are at $Re* = 13.6$ and $Re* = 17.9$, and at $Re* = 24.7$ are the turbulent Taylor waves displayed.

2.2.7.2 Taylor vortex flow

When increasing the inner angular velocity above the first critical inner Reynolds number $Re_i = 120$ for a stationary outer wall, the solid body rotation will become unstable. As can be seen from figure 16, the first instability state is called the Taylor vortex flow. This Taylor vortex flow is a three-dimensional, time-independent flow structure. It is a secondary steady state characterized by an axisymmetric cellular pattern stacked in the axial direction in which the fluid travels as a series of counter rotating vortices, known as Taylor vortices. These vortices can be considered as the effect of the no-slip condition on the stationary sidewalls to the adjacent fluids. Son et al. also noticed these instabilities in their numerical simulations. Taylor vortices were present near the wall in the case when the cylinder walls stopped spinning.[41] Their numerical results are depicted in figure 20.

Figure 20: Numerical results of the vortex streamlines[41]

Sohn et al. emphasized in a continuation on the research of Son et al. [41] where Sohn et al. stated that the Taylor vortex is the main reason of the air-core generation. They showed that when the air-core is being generated, the pushed fluid to the side wall immediately undergoes a strong vortexing flow with a tangential axis (the Taylor vortex). The streamline distribution in figure 21 showed that during the early stages of draining, these vortices are being generated and will remain in succession until the end of draining where they expand their sizes by combining with one another.

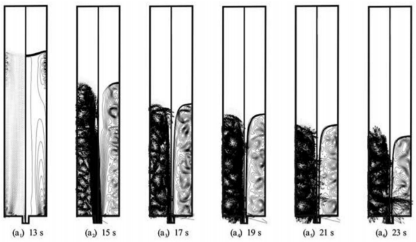

(a) Tank diameter is 90 mm

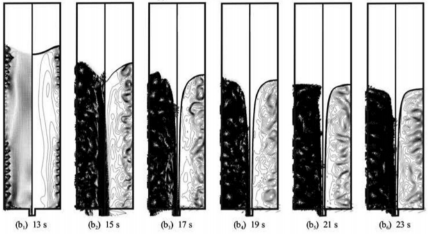

(b) Tank diameter is 120 mm

Figure 21: Progression of velocity vector and streamlines in a tank during draining[43]

However, Khoshkalam and Najafi also did numerical experiments on the generation of the air-core vortex, which are displayed in figure 17. They concluded that the Taylor vortices were not the only cause of air-core vortex generation.[42] Their experiments consisted of a bathtub vortex in a rotating cylinder and the bathtub vortex in a pre-rotated fluid where the cylinder was stationary during the draining process. They found that in both experiments, the air-core vortex was present, however only in the case of a stationary wall, there was presence of Taylor vortices.

2.2.7.3 Wavy vortex flow

Further increasing the inner angular velocity, an instability sets in that deforms the Taylor vortices to produce a time-dependent non-axisymmetric flow, which is called the wavy vortex flow. The flow develops significantly in the axial direction and a new regime is established which has periodic waves travelling in the azimuthal direction. For different initial conditions different stationary wavy vortex flows were noticed. [60] For the case of $Re_o = 0$, the wavy vortex flow is periodic over a wide range of Re_i and vortex sizes. Up to 26 different stable states for different Reynolds numbers were being noticed by Coles for an aspect ratio of $A* = 27.9$, where $A* = \frac{h}{r_o - r_i}$ is a height-radius ratio.[61] He stated that the frequency with which the waves pass a point of observation was characterized by one single frequency f_1.

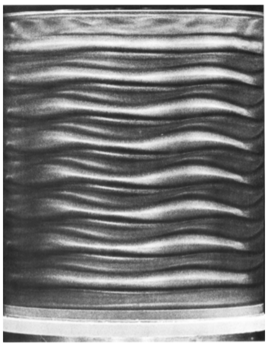

Figure 22: Photograph of the conventional wavy vortex flow by Gregeory et al. [62]

2.2.7.4 Modulated waves

By furtherly increasing the inner angular velocity, an additional wave mode appears that modulates the wavy vortex flow, where the waves oscillate azimuthally with respect to one another and a quasi-periodic regime is obtained, This is the last pre-turbulent flow regime for a stationary outer cylinder and is characterized by a second frequency f_2.[63] f_2 is the frequency of amplitude and frequency modulation on the azimuthal waves. Coles found that the axial wavelength increased with an increase of the Taylor number.[61] The wave flattens out at maximum amplitude modulation and fully disappears, which means that the flow goes into the turbulent state. A good visualization is done by Gorman et al. and depicted in figure 23, where 6 different waves were observed.[63]

Figure 23: Complete wavy modulated vortex pattern for six azimuthal waves [63]

2.2.7.5 Turbulent Taylor waves

For even higher Reynolds numbers, drastic changes are noticed in the flow. The fluid flow becomes turbulent, where first the waves modulated by f_2 and later at even higher values of the Reynolds numbers f_1 disappears. This means that the observed azimuthal waves disappear as well. The disappearance can be clearly seen in figure 19, where the coherent oscillatory motions disappear and the vortices become flat again. However, it was observed with velocity fluctuation power spectra that even though the waves were not visible, the Taylor vortices would still retain their basic toroidal structure.[60]. Experiments done by Koschmieder also showed that for a fluid in the gap between a rotating inner and stationary outer vertical cylinder, at very high Reynolds numbers well organized toroidal turbulent Taylor vortices with uniform size could be observed.[64]

2.3 Drainage from a closed reservoir in presence of rotation

In the previous section, the free surface vortex was discussed for open geometries with a drainage port. In these open reservoirs, an air-core vortex can already be formed for the slightest initial angular velocities. However, the formation of free-surface vortices at low angular velocities is not possible when considering the PET bottle or a cylindrical geometry with only one outlet. This is due to the under-pressure that arises at the top of the bottle. Instead of the small dimple bathtub vortex that is noticed in the open reservoir for a low angular velocity, a bubble regime emerges, as discussed in chapter 2.1. Taylor bubbles will rise upwards into the bottle, while fluid will simultaneously flow downwards out of the bottle. The vortex can only emerge in a closed geometry when the dimple stretches all the way down to the opening of the bottle and a fully developed air-core is present. As a result, for a fully developed air-core to be present, the initial rotational speed must be considerably higher than for the case of a small dimple. This means that the Rossby number, denoted in equation 32 will be higher than in the case of the open container, in which case the non-linear effects in the fluid flow can not be ignored anymore. Instabilities will start to develop in the fluid flow [50] and the 1/4-Stewartson layer breaks away from the sidewall and propagates into the bulk fluid as a detached shear layer. This also enhances the transfer of angular momentum into the fluid, which will expedite the spin-up process.[65]

2.3.1 Bubble growth suppression due to rotation

It was found in section 2.1.2, that by altering fluid properties, the growth rate of the Rayleigh-Taylor instability can be influenced significantly. However, it is believed that one other way to hinder the development and propagation of the bubble from the interface is to apply rotation in the direction aligned with the axis of rotation. El-Ansary et al. [66] found that for very low rotational velocities, the growth rate of the instability would increase with decreasing rotational velocities, up to where for the stationary case the maximum growth rate was achieved. Chandrasekhar concluded that the Coriolis force acting on the Rayleigh-Taylor instability could stabilise the system, but not indefinitely. [67] Carnevale et al. [68] obtained numerical results where they showed a comparison between the development of the bubble for no rotating and rotating system. In the case with no rotation (figure 24a), a mushroom-like cap has already formed, whereas in the case with rotation (figure 240b) the cap structure has not yet been formed and the deceleration of the growth of the bubble is clearly seen. Figure 24 a and b are taken at the same moment. The presence of rotation introduces a restoring force on the fluid layer moving perpendicular to the axis of rotation, namely the Coriolis force. When absent of rotation, the interface undergoes a rotation as shown in figure 25 due to gravity. The Coriolis force induces a flow in the opposite direction of this vortex, which causes the stabilizing effect on the Rayleigh-Taylor instability. From this, it is expected that the initial bubble growth into the top bottle is faster for the stationary case in comparison to the rotational cases. However, this conclusion is drawn for cases where the comparison is made between very low angular velocities and the stationary case. Since in this study the bottle will be initialized with a broad range of angular velocities, the behaviour of the Rayleigh-Taylor instability for high angular velocities is still unknown.

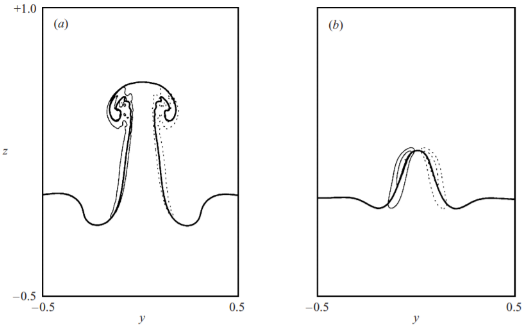

Figure 24: The growth of the interface instability a) no rotation b) with rotation around the vertical axis [68]

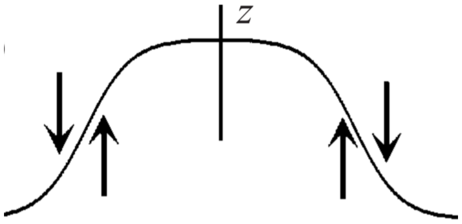

Figure 25: A vertical cross-section illustrating the vorticity effect on the interface due to gravity [68]

2.4 Summary literature review

To finalize the literature review, a short summary will be given on the most important findings that were obtained in this literature review.

From drainage with absence of rotation, equation 10 is a very relevant finding. It describes the emptying time of the bottle for the stationary case $t_{d,0}$. Since the aim of this study is to minimize the non-dimensional drainage time $t*$, where the drainage time is made dimensionless with the stationary emptying time, the emptying time for the different Π-numbers can be compared with equation 10 to obtain the dimensionless drainage time. Also, the parameter k in equation 10 changes in relation to the fluid properties. Therefore, by altering the Morton and Eötvos numbers, the dimensionless drainage time will also be influenced by the stationary time $t_{d,0}$.

Tons of research is already obtained on the generation and the flow dynamics of the free surface vortex in open reservoirs. The drainage process is divided into two stages, the spin-up and spin-down. The spin-up is defined as the stage, where the lid at the bottle opening is still closed and the whole bottle is initialized with a certain angular velocity. How the fluid flow behaves during spin-up was ellaborated in the literature review in the form of the Taylor-Proudman theorem and the interaction of the boundary layers to the fluid flow. When the bottle is stopped and the lid is opened, the stage is defined as the spin-down or drainage regime. Different instabilities during drainage are discussed, such as Taylor vortices, that can occur when the side and end walls are stopped abruptly. Also, different parameters that can suppress or generate the air-core were discussed. It was found that initial rotation speed, tank size, drain port size and fluid properties all can have significant influence on the drainage time and generation of the air-core vortex.

However, during this literature review, no paper or study was obtained that described the drainage process specific for a closed reservoir. It can be argued that when the air-core is formed in the closed geometry / bottle, the air-core vortex is identical as in an open geometry. However, the transient process due to the under-pressure as well as the existence of a minimal critical Π-number, makes this study different than for the case of an open container.

3 3D numerical analysis

In this research, a fully 3D flow simulation of the drainage process from a PET bottle will be performed. The calculation are done in the commercial CFD package, Ansys Fluent 19.2. To obtain accurate results, the correct mesh density and simulation strategy had to be come up with. This section will elaborate on the choices. A short summary of all the CFD-settings are given in appendix B.

3.1 Setup

To ensure that the numerical results obtained in this research could be validated with experimental results, the setup and the geometry/the dimensions of the bottle were already pre-fixed. The setup and geometry were based on the research projects conducted by the team of BSc students in the P&E department of the Delft University of Technology under supervision of dasr.ir. W.-P. Breugem, who previously investigated the bathtub vortex in an experimental manner. A short summary of their findings is shown in appendix A. This subsection will first provide a visualization of the experimental setup used by the students and afterwards the numerical setup will be shown.

To create the closed system, two PET bottles are connected with each other through a ball valve. To obtain the initial rotational velocity, both bottles are placed in a rotating frame which is driven by a motor. The motor starts spinning until solid body rotation has been achieved. During the spin-up regime, the ball valve is closed. Since it was difficult for the experimental setup to visually determine when solid body rotation had been reached, a pre-fixed spin-up time of 10 minutes was selected to ensure that solid body had been reached. The valve would then be opened and the drainage time would be measured. The drainage time was defined from the moment the valve was opened until the last liquid fraction had disappeared from the upper bottle. A representation of the experimental setup is made by the previous students and shown in figure 26.

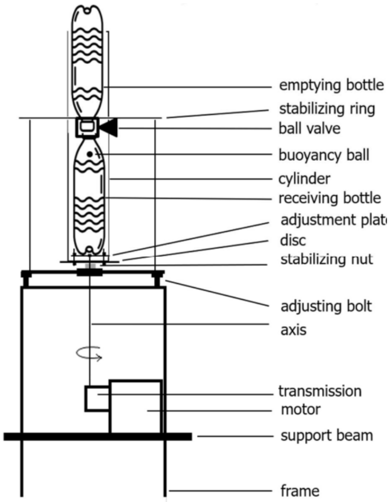

Figure 26: Experimental setup

As explained before, the dimensions of the experimental bottle were also used for this numerical study. The shape of the bottle was chosen to be relatively simple. The geometry and the dimensions of the bottle are depicted in figure 27. The diameter of the bottle is 73.5 mm and the height is 217 mm. The opening of the bottle is centered with a diameter of 21.5 mm. The angle between the wall and the opening of the bottle is 40 degrees. The initial water level is 200 mm, which is measured from the opening of the bottle. The bottle connector has the same inner diameter as the bottle opening and the height of the connector is 40 mm.

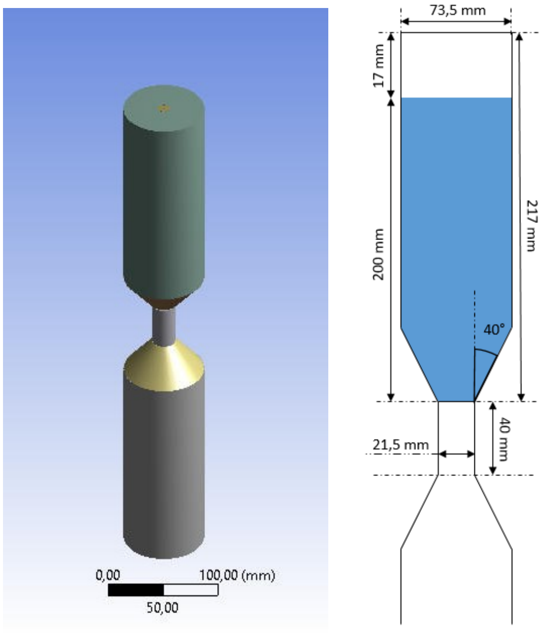

(a) (b)

Figure 27: (a) 3D view of the numerical case (b) intersection and dimensions of the bottle

3.2 Dimensional analysis of relevant flow parameters

To optimize the drainage time, the right parameters should be put in different test cases and be tested on their influence on the drainage time. This can be done by selecting suitable dimensionless groups based on these different parameters. However, to distinguish which parameters and dimensionless groups are useful, first the emptying sequence has to be classified into different stages. By matching the dimensionless parameters to the several draining sequences, the optimum can be found for every sequence and thus reduce the drainage time altogether. The bottle dynamics can be classified into four major stages on the basis of their flow dynamics, which will be discussed below. The four stages are based on observations from the experimental results. A visualization of the different regimes are depicted in figure 28.

Stage 1, Bubble regime: When the bottle is opened, the liquid inside the bottle starts to flow out, while simultaneously the air wants to penetrate into the bottle in the form of a symmetric gaseous finger. The bubble starts to grow at the bottle opening, until the surface tension can not hold the hydrostatic pressure anymore, which at that moment the bubble detaches from the outside air. Due to the under-pressure in the bottle, more bubbles will start to form in the same process. A more detailed description about the bubble regime was described in section 2.1.5 and in the works of Rohilla and Das [15].

Stage 2, Transition regime: More bubbles starts to rise to the top of the bubble. Bigger bubbles start to form that stretches down to the bottle neck due to the centrifugal force pushing the liquid to the side. This happens until a fully developed air column is noticed between the surface level and the outside air-stream in the lower bottle. The characteristics of the transition regime are defined as where the pressure difference between the atmospheric pressure in the bottom bottle and the under-pressure in the top bottle has disappeared. However, no fully developed air-core vortex has been noticed yet and the water layer keeps merging in the center of the bottle.

Stage 3, Vortex regime: The free-surface vortex is noticed in this stage. The vortex look stable and is fully-developed. A regular downward motion of liquid along the bottle wall is realized, which is accompanied with an upward motion of air through the core.

Final stage, Swirl regime: When the last fraction of fluid is left in the upper bottle, the fluid swirls around the vertical axis, until the fluid is slowed down sufficiently to exit the bottle through the opening.

This regime takes a significant amount of drainage time, whereas the volumetric flow rate of the fluid is minimal.

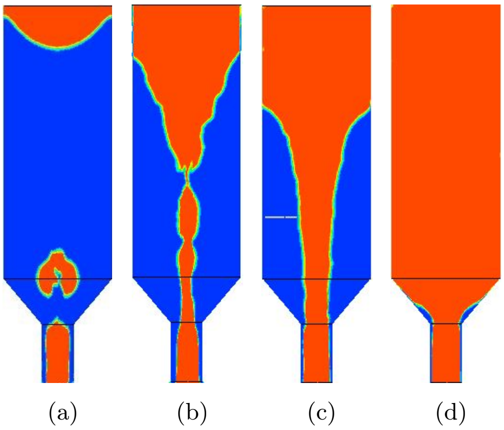

Figure 28: Visualization of the 4 stages a) bubble regime $t = 0.25$ s b) transition regime $t = 1.25$ s c) vortex regime $t = 3.5$ s d) swirl regime $t = 7.8$ s. The figure contours are part of the numerical results obtained for the Pi case of $\Pi = 0.6195$, where the initial angular velocity is 30 rad/s.

Since the different stages have been characterized, the multiple parameters can be selected. With these parameters different dimensionless groups can be formulated to describe the different stages, which can give an insight in the importance of the different parameters to the drainage time. The following parameters are considered to be of importance for the different stages:

Nozzle diameter	d_h	[m]
Bottle diameter	d_b	[m]
Nozzle angle	θ	[-]
Initial water level	h_0	[m]
Angular velocity	Ω	[s^{-1}]
Gravitational acceleration	g	[$m \cdot s^{-1}$]
Density liquid, gas	$\rho_{l,g}$	[$kg \cdot m^{-3}$]
Viscosity liquid, gas	$\mu_{l,g}$	[$kg \cdot m^{-1} \cdot s^{-1}$]
Surface tension	γ	[$kg \cdot s^{-2}$]
Drainage time	t_e	[s]

Table 1: Parameters

As seen in table 1, there are nine independent parameters with three base units. From Buckingham-Pi, this means that there are eight different dimensionless groups that can be formed. There are three numbers concerning the geometry of the bottle and two groups concerning the dynamic viscosity ratio and the density ratio, which are depicted in 55.

$$\frac{d_h}{d_b} \qquad \frac{h_0}{d_b} \qquad \theta \qquad \frac{\mu_g}{\mu_l} \qquad \frac{\rho_g}{\rho_l} \tag{55}$$

To keep the scope of this numerical investigation small, the bottle dimensions are kept constant. The dynamic viscosity ratio and the density ratio are significantly small and thus are left out as well. However, for the interested, Geiger et al. investigated the effect of bottle geometry ($\frac{d}{D}$) and inclination (θ) on bottle emptying processes with no initial rotation through a CFD approach. [69]

By keeping the five numbers stated in 55 constant, it means that there are four dimensionless groups remaining. The remaining dimensionless groups are the non-dimensional total drainage time, and the Eötvos, Morton and "Pi" numbers:

$$\begin{aligned} t^* &= \frac{t_e}{t_{e,0}} \\ Eo &= \frac{\rho_l g d^2}{\gamma} \\ Mo &= \frac{\mu_l^4 g}{\rho_l \gamma^3} \\ \Pi &= \frac{\Omega^2 \frac{1}{4} d_b^2}{g h_0} \end{aligned} \tag{56}$$

The dimensionless total drainage time is defined as the ratio between the emptying time with rotation t_e compared to the stationary emptying time $t_{e,0}$. The stationary emptying time is obtained from the literature depicted in equation 10. The emptying time is for the case when the Morton number is low and Eötvos number is high. Since the emptying time will be heavily influenced by the Π number and the value of k in equation 10 is dependent on the Morton and Eötvos number, it can be stated that the dimensionless total drainage time is dependent on the other three dimensionless parameters. Therefore, to study how each dimensionless parameter impact the non-dimensional drainage time, the effect of the Π, Morton and Eötvos will be separately investigated in this study.

From the literature review, it was already obtained that the bubble characteristics could be described through the use of the Eötvos and Morton numbers. The increase of the Morton number is paired with an increase in viscosity. It is believed that by increasing the Morton number, next to the change of bubble characteristics, also the overall velocity might decrease, causing a later generation of the air-core vortex and thus effecting the drainage time. The bottle is pre-rotated, thus it is also a necessity to investigate the role of the angular velocity on the drainage time. By comparing the ratio of the centrifugal force to the initial hydrostatic pressure (Π-number), characteristics in the vortex regime can be determined, such as the shape of the vortex and the thickness of the film in the nozzle.

3.3 Mesh

3.3.1 Mesh topology

To generate a 3D mesh that can accurately calculate the numerical solutions, first the different types of meshes have to be looked into. There are two main types of meshes, unstructured and structured meshes. Both of these meshes have their advantages and disadvantages. That is why choosing the correct choice of mesh type can improve the accuracy of the solution but also save computing and setup time. The big difference between structured and unstructured meshes is that the structured mesh is identified by regular connectivity, while the unstructured mesh is identified by irregular connectivity. The main motivations to choose structured over unstructured grids are that structured grids are highly space efficient, convergence is achieved faster and less numerical false diffusion. However, many numerical problems involve complex geometries, making it highly time-consuming or sometimes near to impossible to design structured grids for these complex geometries. In these cases, it is more efficient and convenient to use a unstructured mesh with triangular or tetrahedral cells. Another downside of building a structured mesh in complex geometries include over-stretched mesh cells and other mesh quality issues. However, this does not apply on the numerical model in this research, where the PET bottle consists of only standard geometries. Thus, a radial structured grid has been chosen as the type of mesh to ensure that less false numerical diffusion would occur.

Also, different type of cells can be chosen in 3D meshing: tetrahedral, hexahedral, polyhedral, pyramid, wedge cells or a combination of these. The hexahedral cells are shaped as a cube where the hexahedral cells are bounded by six other hexahedral cells. For the same amount of cells, the hexahedral meshes have the highest accuracy of the numerical solutions. Thus, a radial structured hexahedral mesh was chosen as the mesh for this case.

For cylindrical pipe geometries, different mesh structures can be applied to build a structured mesh. Three of those structured cylindrical pipe meshes are shown in figure 29. The first mesh that can be used is the cylindrical mesh called the O-grid mesh. The O-grid mesh consists of grid lines forming concentric circles around the centre and radially directed grid lines. The second mesh is based on a rectangular structure, called the H-grid. This grid adapts the rectangular grid to the cylindrical geometry. The last mesh is known as the butterfly grid, where a Cartesian mesh is used in the centre of the cylinder and surrounded by a cylindrical mesh structure.

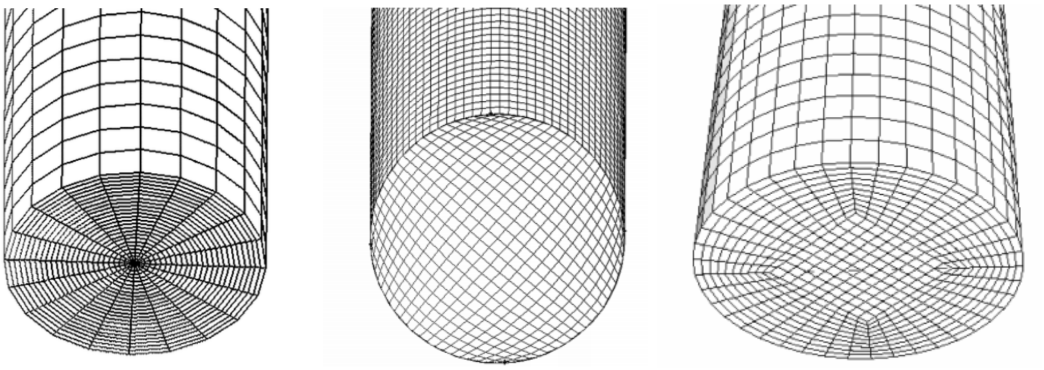
(a) (b) (c)

Figure 29: Different mesh structures for cylindrical geometry a) cylindrical b) rectangular c) butterfly

Hernandez-Perez [70] investigated the three mesh structures stated above for 3D two-phase flow in pipe geometries. The results showed that there was a strong dependency between the mesh and the flow behaviour. The best result was obtained when implementing the butterfly mesh, while a fully cylindrical mesh gave misleading results. The butterfly mesh allowed for refinement close to the wall and also prevented singularity at the centre of the pipe. Thus, the structured mesh that was designed in this study was based on the butterfly model depicted in figure 29c.

3.3.2 Design of the bottle mesh

To design the butterfly mesh, first the bottle was divided into five basic geometries: the cylindrical section (1,5), the conical section (2,4) and the bottle connector (3). The different segments are labeled in figure 30.

As stated in the previous section does the butterfly mesh consist of a Cartesian mesh at the centre of the cylinder, where it is surrounded by a cylindrical grid. Thus, the mesh of each segment consists of an inner cuboid (Cartesian mesh), where the inner cuboid is surrounded by the cylindrical geometry of the bottle (cylindrical grid). To refine the boundary layer, a cylindrical ring is established around the cylindrical geometry of the bottle. A good representation of the three different grids is depicted in figure 31 b. The inner cuboid is implemented in the geometry to make sure that everywhere in the mesh hexahedral cells were present. To reduce cross-flow diffusion, it is desired that the direction of the mesh cells are in the same direction as the flow direction. Therefore, the inner cuboid is made as small as possible to maximize the amount of radial mesh cells, since it is expected that the vortex flow is mainly dominated in the tangential direction. A visualization of the different segments and the different parts of the segments are depicted in figure 31.

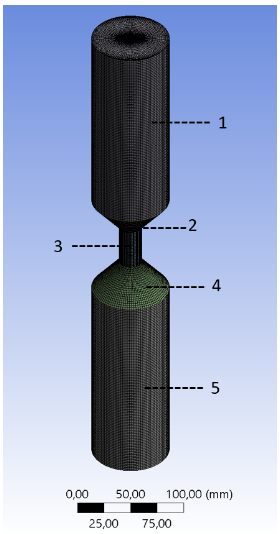

Figure 30: Experimental setup

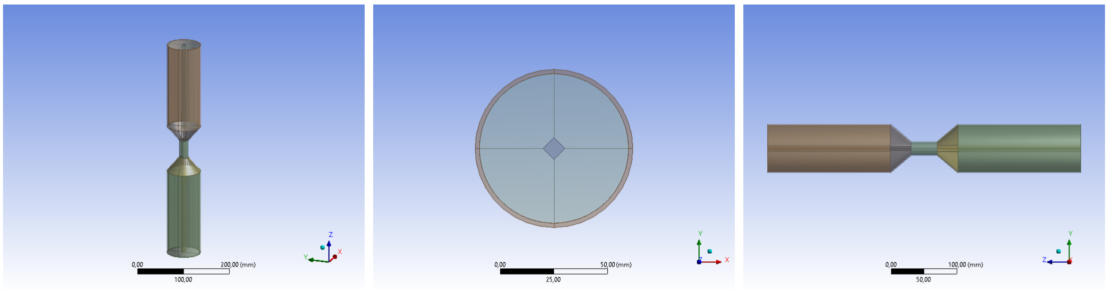

(a) (b) (c)

Figure 31: Representation of the different grids in a) Isometric view b) top view c) side view

Since the geometry consisted of multiple bodies with different geometries, MultiZone meshing was used to ease the design procedure of the mesh structure. The MultiZone approach automatically decomposes the geometry, which results in a directly generated structured mesh. The structured blocks can be meshed with Hexa or Hexa/Prism. As stated in the previous section was a hexahedral structured mesh desired to reduce false numerical diffusion. Thus, by using the hexa-dominant MultiZone approach, an almost fully structured hexahedral mesh was already established. To ensure that the mesh cells at the intersection between the different geometry segments would align with each other, local sizing with number of divisions was applied. Another advantage of local sizing is the elimination of sudden mesh density changes between the geometries. A smooth transition between the different bodies results in more accurate numerical results. Detailed views on the mesh are depicted in figure 32.

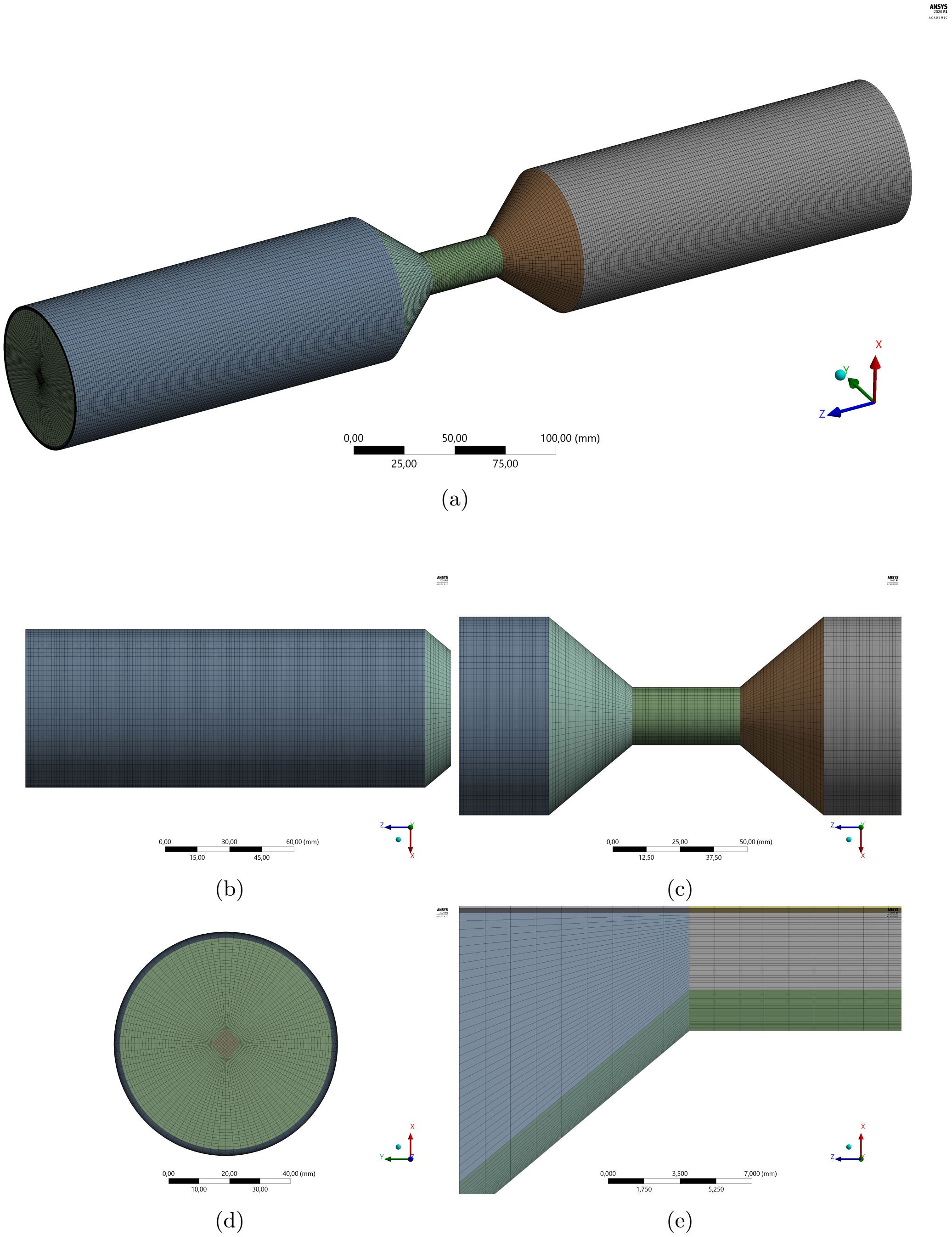

(a)

(b)

(c)

(d)

(e)

Figure 32: a) Isometric view b) Side view of cylindrical section c) Side view of conical and connector section d) Top view e) Cut view between connector and conical section

3.3.3 Boundary layer meshing

Next to the overall mesh structure should the boundary layer also be resolved correctly. Failure to resolve the boundary layer is known to affect the accuracy of the numerical solution. To characterize the effect of the boundary layer on a wall bounded flow in numerical simulations, the dimensionless wall unit y^+ can be used, which is given by:

$$y^+ = \frac{u_\tau \Delta y}{\nu} \tag{57}$$

where u_τ is the frictional velocity and Δy is the distance between the first cell height and the nearest wall. If no turbulence model has been selected, $y^+ < 1$ is required to accurately model the boundary layer. This is achieved by estimating the first cell height from the wall by rearranging equation 57 to

$$\Delta y = \frac{y^+ \nu}{u_\tau} \tag{58}$$

where the frictional velocity u_τ can be written as:

$$u_\tau = \sqrt{\frac{\tau_w}{\rho}} \tag{59}$$

and the wall shear stress τ_w can be calculated with the bulk velocity $u_{bulk} = 0.5\Omega D$ by:

$$\tau_w = 0.5\, C_f \rho u_{bulk}^2 \tag{60}$$

and finally the skin friction C_f can be estimated from the Schlichting skin-friction correlation [71] given as:

$$C_f = \left(2log_{10}Re_{bulk} - 0.65\right)^{-2.3} \tag{61}$$

The Reynolds number in the bulk fluid is defined as

$$Re_{bulk} = \frac{u_{bulk} L}{\nu} \tag{62}$$

where the effective length scale L was taken from the circumferential length / perimeter of the bottle $L = \pi D$.

As can be seen from the bulk velocity and the Reynolds number is the value for the first cell distance estimated for the case of spin-up. Spin-up is characterized where the fluid flow behaves like solid body rotation, hence $u = 0.5\Omega D$. However, from the literature review, it was already obtained that instabilities close to the boundary layer can be formed during spin-down. Therefore, also the first cell distance will be estimated for spin down. Equations 57 to 61 remain the same for spin-up and spin-down, only the Reynolds number changes. In section 2.2.7, the inner and outer Reynolds number are depicted, where it was explained that during spin-down, the outer Reynolds number is zero. Therefore, the inner Reynolds number should be used to estimate the first cell distance. The first cell distance will be calculated for both Reynolds numbers. The smallest cell height will then be selected to ensure that for spin-up and spin-down, the boundary layer is resolved correctly.

To provide a smooth transition from the reduced cell size in the boundary layer to the bulk stream cell size, an inflation layer was used. The size of the cells in the inflation layer would gradually increase until the bulk stream size was achieved. This was done by specifying the first cell height ($y+ = 0.9$) from the wall and applying an inflation growth rate of 1.05 in Ansys meshing. A closer view on the refined mesh cells in the boundary layer is depicted in figure 33.

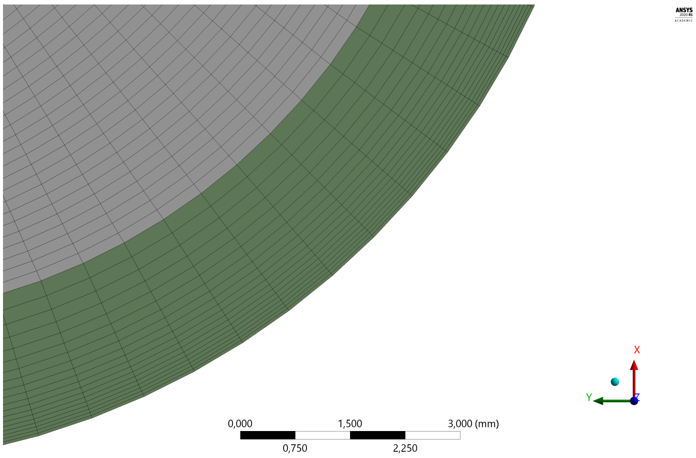

Figure 33: Wall refinement of the mesh

3.3.4 Mesh independence study

To ensure that accurate numerical results can be obtained, a mesh independence study has been performed on the designed mesh explained in the previous section. Details of the mesh used in this mesh independence study are shown in table 2.

Mesh case	Mesh name	No. of elements	No. of nodes
1	400	375552	383268
2	1mil	1091448	1106895
3	2mil	1934108	2046042
4	3mil	2893042	3016487

Table 2: Mesh sizes used to determine mesh independence

3.4 Simulation strategy and computation

3.4.1 Laminar and Turbulence models

The flow characteristics of the fluid is largely dependent on the rotational velocity of the air-core vortex and the wall. From the literature review, it was already obtained that figure 16 can be used to distinguish the different flow regimes for the Taylor-Couette flow. The distinguishment between the different flow regimes is dependent on two dimensionless parameters, the inner Reynolds number Re_i and outer Reynolds number Re_o, where

$$\begin{aligned} Re_i &= \frac{r_i(r_o - r_i)\Omega_i}{\nu} \\ Re_o &= \frac{r_o(r_o - r_i)\Omega_o}{\nu} \end{aligned} \tag{63}$$

However, by assuming that the air-core vortex mimics the same characteristics as an inner cylinder, figure 16 can also be used to determine the flow regime for the tested cases in this study. This is done by taking the inner radius as the bottle opening radius and the initial angular velocity as the inner angular velocity.

The whole process is divided into two distinct flow regimes, the spin-up and spin-down. Since these flow regimes have their own separate characteristics, both regimes will be evaluated separately to determine whether turbulence modelling is necessary for each regime. When looking at spin-up, the fluid behaves as a solid body rotation, where no air-core vortex is present in the bottle. Since there is no air-core vortex, the inner radius of the imaginary inner cylinder is zero and thus the inner Reynolds number is also equal to zero. This means that we are in the Couette flow regime, which is highlighted with the green box in figure 34. The Couette flow regime is defined as a laminar regime, thus no turbulence modelling is necessary for the spin-up process. For the spin-down regime, the air-core vortex is present in the bottle, which means that the inner Reynolds number can not be zero. However, in the spin-down regime, the wall of the bottle is stationary, which results in the angular velocity of the outer cylinder Ω_o being zero. Therefore, the outer Reynolds number Re_o is equal to zero and the corresponding flow regime is highlighted in the red box in figure 34. The red box is in the Turbulent Taylor vortices regime indicating that the fluid flow is turbulent and thus, for the spin-down regime, turbulence modelling is necessary.

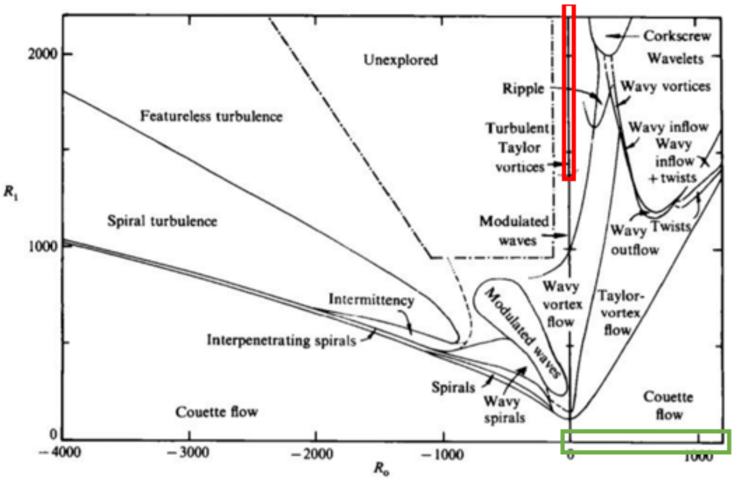

Figure 34: Flow regime graph for the different instabilities in the Taylor-Couette flow, where R_o is the outer Reynolds number and R_i is the inner Reynolds number

Based on previous studies that investigated the free surface air-core vortex in an open reservoir [72, 73], it was very likely that the standard RANS models would overestimate the turbulent kinetic energy, turbulent dissipation rate and turbulent viscosity in the core of the vortex. This is due to the weakness of eddy-viscosity models, which assumes that the turbulence is isotropic. Assuming isotropic turbulence can lead to overestimated diffusion in strong streamline curvature streams. Mulligan investigated the free-surface vortex for the case with no turbulence model, RNG $\kappa-\epsilon$, SST with and without curvature correction (SST and SST-CC) and the RSM turbulence models [74]. The RNG $\kappa-\epsilon$ exhibited extremely poor performance compared with to other models. SST with curvature correction significantly increased the computational accuracy in comparison without curvature correction. The solution without the use of a turbulent model yielded similar results as the SST-CC model when predicting the free-surface, but the accuracy of predicting the tangential velocity was higher when no turbulence model was selected. According to Mulligan, [74] the RSM turbulence model gave the most accurate results, whereas the SST-CC turbulence model and the model with no turbulence model were slightly less accurate. However, the computational cost were significantly higher for the RSM in comparison with the no turbulence model and the SST-CC models. Different studies also investigated LES models since LES models capture vortex characteristics more accurately than the other turbulence models. [75, 76] However, the increase in accuracy comes with an additional considerably higher computational expense. Sakai et al. and Muntean [77, 78] found that simulations of swirling flows in pipes, where no turbulence models were selected captured the characteristics of the vortex just as well as LES simulations with a fraction of the computational time, even if the flow outside the vortices is known to be turbulent.

In this study, simulations with no turbulence model, $\kappa-\epsilon$ models and the RSM model were all tried. The $\kappa-\epsilon$ models gave very nonphysical results where in some cases, the interface was impenetrable. This meant that the water would stay in the top bottle, while air stayed in the bottom bottle. Another error that was observed with the $\kappa - \epsilon$ models was the calculation of the turbulent viscosity. The turbulent viscosity ratio in every calculation would reach above 1e5 at a certain stage, which is very nonphysical in this test case. Even when initializing with a very low turbulent viscosity or refining the mesh, in the end the turbulent viscosity would still be unusually high. The RSM model was found to be highly unstable. Non-physical instabilities at the free surface started to develop, which caused the simulation to fail within a few time steps. The only solution to resolve these instabilities was to design a very fine mesh and decrease the time steps significantly. However, this made the model very computational expensive and not feasible to use in the time period for this study. These kind of instabilities that were obtained for the RSM model were also found by Mulligan [74] and Suerich [73]. Thus, the only viable model was the laminar viscous model (no turbulence model was selected) and therefore chosen as the viscous model for this study.

3.4.2 Multiphase Modelling

Several different methods have been developed in the past to simulate two-phase flow problems. The most used methods include the front-tracking method [79], the marker particle method [80], the volume of fluid (VOF) method [81] and the levelset (LS) method. Every method has their own advantages and disadvantages, this study will only elaborate further on the latter two, since they are mentioned the most in literature and already produce accurate results.

The VOF method has been widely used to solve the deforming free interfacial flows between immiscible fluids. A new parameter, the volume fraction α is introduced with this method. The volume fraction of phase k in every cell is calculated as follows:

$$\alpha_k = \frac{V_k}{V} \tag{64}$$

where V_k is the volume of phase k in one specific cell. When the volume fraction α is between 0 and 1 in a certain cell, a liquid-gas interface should exist. Cells that are not located on the free surface will either have $\alpha_w = 1$ or $\alpha_a = 1$. Also, the sum of both the volume fractions should always be 1, thus the following condition should always be satisfied in every cell:

$$\alpha_w + \alpha_a = 1 \tag{65}$$

where α_w and α_a are the volume fractions of water (liquid) and air (gas) respectively. The density ρ and dynamic viscosity μ in each cell is calculated as follows:

$$\begin{aligned} \rho &= \alpha_w \rho_w + \alpha_a \rho_a \\ \mu &= \mu_w \rho_w + \mu_a \rho_a \end{aligned} \tag{66}$$

The tracking of the interface between the phases is done by solving the transport equation for the volume fraction α of one of the phases:

$$\frac{\partial \alpha}{\partial t} + \nabla \cdot (\mathbf{u}\alpha) = 0 \tag{67}$$

Since for equation 67, the standard finite-difference approximation leads to smearing, a piecewise-linear approach is used to reconstruct the interface with the VOF method. The piecewise linear interface calculation (PLIC) technique approximates the interface in the cell by reconstructing the interface in a cell as a line (in two-dimensional space) or a plane (in three-dimensional space). The reconstruction of the interface is approximated by the idea that the normal vector plus the volume fraction α can determine the linear interface cutting from the cell, where the normal vector $\mathbf{n}$ can be computed from:

$$\mathbf{n} = \frac{\nabla C}{\mid \nabla C \mid} \tag{68}$$

However, the big drawback of the VOF method is that the volume fraction function is a step function, which makes it highly difficult to accurately predict the curvature of the interface, even with the PLIC method. [82] A direct consequence of this inaccuracy of the interface is the curvature of the free surface and the surface tension force.[83] Thus, another method has to be used to capture the interface accurately.

One method that can accurately compute the free surface is the Level Set method. Level-Set functions are based on the use of a continuous function ϕ to describe the interface between two different fluids. The interface is tracked by solving a transport equation for the signed-distance function to the interface:

$$\frac{\partial \phi}{\partial t} + \mathbf{u} \cdot \nabla \phi = 0 \tag{69}$$

where $\phi = 0$ corresponds to the interface, $\phi > 0$ and $\phi < 0$ corresponds to the liquid and gas phase respectively. Geometrical information about the surface such as the normal vector $\mathbf{n}$ and the curvature κ can be obtained with the Level-Set function [82]:

$$\begin{aligned} \mathbf{n} &= \frac{\nabla \phi}{\mid \nabla \phi \mid} \\ \kappa(\phi) &= -\nabla \cdot \mathbf{n} \end{aligned} \tag{70}$$

However, the drawback when using the Level-Set function is that it produces more numerical errors than the VOF method, especially when the interface undergoes stretching or tearing. A common inaccuracy of the Level-Set function is that it is not mass conserving, especially on a coarse grid.[84] Since VOF is mass conserving but has a diffusive interface, while the LS function can produce a sharp interface but is not mass conserving, a new method can be developed by combining both extensions and using both advantages. This new method is called the Coupled Level Set and Volume of Fluid method (CLSVOF).[82] Both the transport equations for the volume fraction α and the level set function ϕ are solved in this method and are coupled to the reconstructed interface, which results in a sharp interface without loss/gain of mass. To accurately track the free-surface without loss of mass conservation, the VOF method in combination with the Level-Set function was also used in this study.

An important dimensionless parameter that comes to play with multiphase modelling is the Courant number or CFL condition. This arises when using explicit time integration schemes. The CFL condition provides an upper bound limit for the timestep, wherein the numerical solution still provides accurate results [85]. The CFL condition is defined as:

$$\Delta t \leq C_{CFL} \frac{\Delta x}{u} \tag{71}$$

where Δt is the time step, Δx the length interval,u the velocity magnitude and C_{CFL} is the Courant number. For explicit timestepping, the typical Courant number should be smaller than 1 to ensure stability and accurate results. The easiest way to ensure that the CFL condition is satisfied, is to enforce that the maximum Courant number over all cells, should be smaller than 1. The length interval is taken as the cell length and the velocity magnitude is taken as the flow velocity of the fluid in the cell. The resulting time represents the time that it would take the fluid to empty out of the cell. In this study, the upper bound limit for the CFL number was kept at 0.25 to ensure accurate results.

A summary of all the multiphase settings are depicted in table 15.

3.4.3 Solution methods

To accurately solve the free-surface vortex numerically, the following governing equations were applied for a 3D, transient, incompressible, laminar flow:

Conservation of mass:

$$\frac{\partial \rho}{\partial t} + \frac{\partial}{\partial x_i}(\rho u_i) = 0 \tag{72}$$

Conservation of momentum:

$$\frac{\partial(\rho u_i)}{\partial t} + \frac{\partial(\rho u_i u_j)}{\partial x_j} = -\frac{\partial p}{\partial x_i} + \mu \frac{\partial}{\partial x_j}\left(\frac{\partial u_i}{\partial x_j} + \frac{\partial u_j}{\partial x_i}\right) + \rho g_i + F_i \tag{73}$$

where ρ is the density, μ the viscosity, p the pressure, t the time, x_i the position vector in the coordinate system, u_i the velocity vector, g_i the gravitational acceleration and F_i the volumetric surface tension force.

When enabling multiphase modelling in Ansys Fluent, different options and restrictions apply to the explicit VOF model. Only the pressure-based solver is available for multiphase modelling. The second-order implicit time-stepping formulation can only be used with the implicit scheme of VOF. Since explicit time-stepping is selected, for equations 72 and 73 only the first order time discretization could be used to solve the equations. The PISO algorithm was used for the pressure-velocity coupling. The central differencing method was applied for the momentum equation and the spatial discretization gradient was utilized with the least squares cell based.

To reconstruct the interface, the geometric reconstruction scheme from Ansys Fluent is used. The geometric reconstruction (Geo-Reconstruct) is based on the PLIC method described in the previous section, where the interface between two fluids has a linear slope within each cell. The position of the linear interface is calculated relative to the center of the mesh cell, which is based on the volume fraction and the normal vector. The level-set function was also selected, to ensure that the interface would be computed accurately (CLSVOF method). A summary of all the solution methods are depicted in table 14.

3.4.4 Boundary conditions

Since the two spinning bottles were connected with each other and thus formed a closed system, the boundary conditions in this numerical case were relatively simple. The closed system indicated that no inlet or outlet boundary conditions were needed, only wall boundary conditions were required. An initial rotational velocity was given to the wall boundary conditions and if needed, the wall surface roughness was defined. A wall / valve was placed between the top bottle and the connector so no fluid would drain to the bottom bottle during spin-up. When solid body rotation was achieved, the valve would then be opened to mark the start of the drainage time.

Every wall surface and material is characterized by irregularities that can cause the characteristics of the fluid flow to change. When the flow is considered to be laminar, the flow is independent on the wall roughness of the PET bottle. However, this does not apply for cases where the fluid flow becomes turbulent. When the wall is considered to be smooth, it can be assumed that the wall roughness is too small to affect the flow. However, when the wall surface is rough enough, the flow will be dominated by separating flow from the roughness elements and detached eddies will be generated. To determine what roughness height is considered to be smooth or rough, the wall Reynolds number can be used:

$$Re_{wall} = \frac{hu_\tau}{\nu} \tag{74}$$

where the wall Reynolds number can be defined as the ratio between the roughness height and the thickness of the viscous sub-layer ν/u_τ. If $Re_{wall} < 1$, it can be assumed that the wall surface is smooth enough to have no significant effect on the fluid flow. When $Re_{wall} > 1$, the height of the roughness elements are higher than the viscous sub-layer, resulting in change of the characteristics of the fluid flow and the viscous sub-layer can no longer be identified.[86] The wall velocity u_τ is defined in equation 59. It is found that in this study, the wall Reynolds number is too low and thus no wall roughness modelling is necessary.

3.4.5 Spin-up

The last subject that has to be discussed in this section is how the spin-up was realized in the numerical model. The flow was first initialized with the desired liquid level in the top bottle. After initialization, both the walls of the bottle and the valve started spinning with a certain angular velocity. The multiphase simulations were extremely sensitive to instability, especially when applying a sudden speed of rotation or degree of swirl during spin-up of the bottle. Therefore, to improve the stability of the simulation, a fraction of the total rotational speed was initialized and then gradually increased until the desired magnitude of the velocity was reached. The spin-up procedure was divided in ten steps, where the first step was initialized with 10% of the total rotational velocity. The simulation was then solved for a few small timesteps. Then for the second step, the speed of rotation was increased to 20% and again solved for a few timesteps. Then for the third step, the speed of rotation was increased to 30% until 100% of the desired rotational speed had been reached. The angular velocity and the free surface was monitored during the spin-up process. Spin-up was achieved when the angular velocity profile became linear (solid body rotation) and the parabolic free surface was noticed. It was also checked whether the velocity profile became independent of time. If the velocity profile looked like a steady-state solution, spin-up was achieved. The spin-up process was only done on the coarse mesh to be time-efficient and later interpolated on the fine mesh when the spin-up had been achieved.

4 Results and discussion

In this chapter, the results from the numerical study will be presented and discussed. The chapter is divided into three parts, where each part discusses the influence of the Π, Morton and Eötvos numbers on the drainage time, respectively. The numerically obtained results were conducted with mesh 2 (1mil mesh in table 2). The mesh independence study can be found in appendix C. Also, verification with the experimental results from the BSc group is done. This is shown in appendix D.

4.1 Case 1: Influence of the Π-number

In the first case, the effects of different rotational velocities are being studied to determine the correlation between rotational velocity and drainage time. A combination of 40%-glycerol and 60%-water was used in all the calculations for the Π-case. The fluid properties are shown in table 3. 6 different velocities were chosen and the corresponding dimensionless Pi-numbers are depicted in table 4.

Glycerol-%	40%
Eötvos [-]	61.5954
Morton [-]	4.5145e-09
Density [kg m^{-3}]	1100
Viscosity [kg $m^{-1}s^{-1}$]	0.00363
Surface tension [kg s^{-2}]	0.07

Table 3: Fluid properties of 40%-glycerol

Angular velocity [rad/s]	Π
0	0
10	0.0688
20	0.2753
30	0.6195
40	1.1014
50	1.7209

Table 4: Different testcases for the Π-case

4.1.1 Draining regimes

This section shows the influence of the Π-number on the duration of the different draining regimes. In section 3.2, the four different flow regimes and their characteristics were discussed. Table 5 shows the duration of every specific regime. Thus, for example in the bottom right corner, it means that for an angular velocity of 50 rad/s, the flow regime stayed for 7.65 seconds in the vortex regime. Figure 35 shows the flow rate of glycerine-water out of the bottle opening. A visual example of the distinction between the different flow regimes is given in figure 36. The example is given for the glycerine rate graph with an angular velocity of 40 rad/s, where the different flow regimes are divided into coloured areas. Figure 37 shows the area fraction of glycerine-water in the top bottle opening. It can be seen that for the glycerine area, the peaks in the bubble regime are rather random. This is due to the difference in frequency between the time steps ($\Delta t = 0.05$ s) and the bubble generation. It is believed that when the frequencies align between the time steps and the bubble generation, the line for area fraction would be more straight. Figure 38 shows how the liquid level grows through the drainage. The volume fraction is made dimensionless with the initial liquid volume in the top bottle and the drainage time is made dimensionless with the emptying time of the stationary case, depicted in equation 10. The value of the stationary emptying time from equation 10 is $t_{d,0} = 15.27$ seconds, whereas the numerically obtained stationary emptying time for 40%-glycerol is equal to $t_d = 16.9$ seconds.

Angular velocity [rad/s]	0	10	20	30	40	50
Drainage time [s]	16.9	12.5	6.275	8.075	8.25	9.15
Bubble regime [s]	16.9	12.5	2	1.05	0.7	0.55
Transition regime [s]	-	-	0.6	0.3	0.15	0.2
Vortex regime [s]	-	-	3.375	6.25	6.85	7.65
swirl regime [s]	-	-	0.3	0.475	0.55	0.75

Table 5: The time periods for the different draining regimes

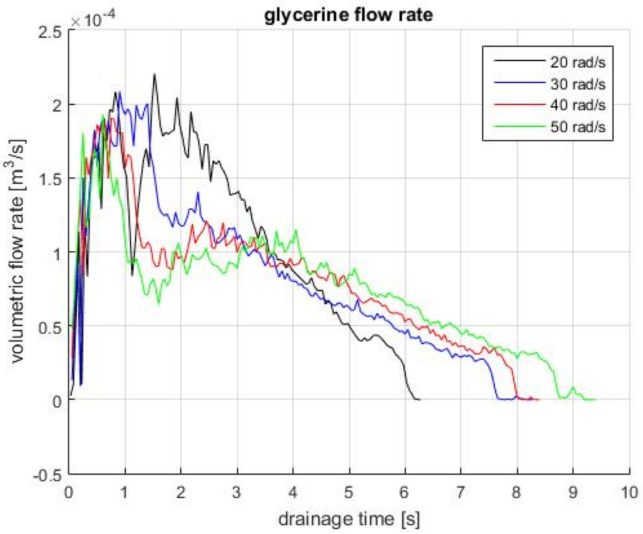

Figure 35: The flow rate out of the bottle for the different angular velocities.

Figure 36: The four different flow regimes for 40 rad/s are divided into four coloured areas for the glycerine flow rate graph.

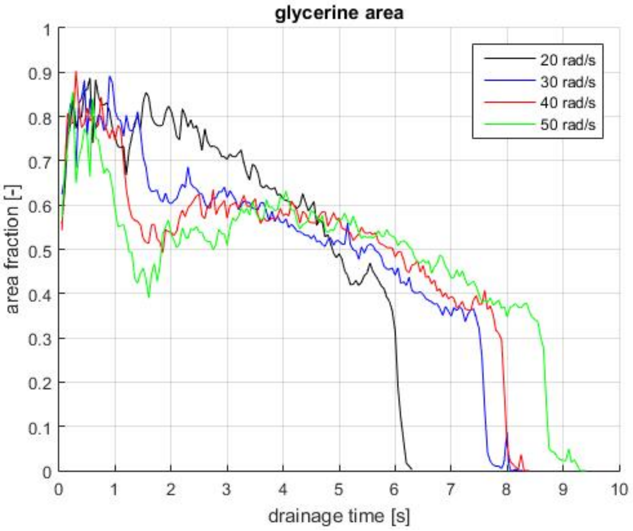

Figure 37: The liquid area in the bottle opening for the different angular velocities.

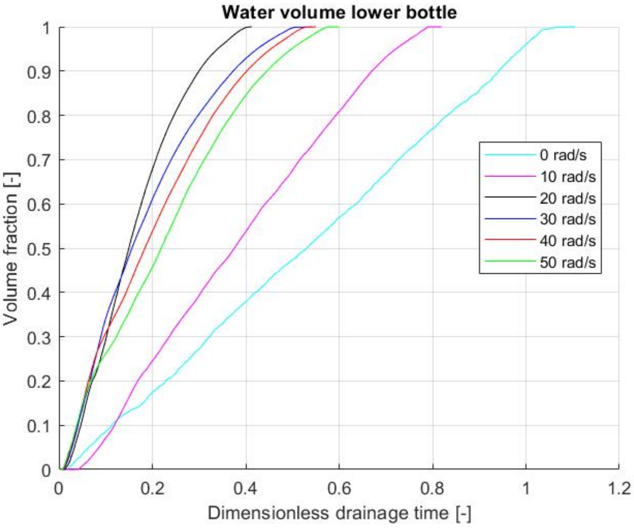

Figure 38: The dimensionless liquid level over the non-dimensional time in the bottom bottle for different angular velocities.

4.1.2 Bubble regime

The regime that is first noticed in the bottle is the bubble regime. Figure 39 shows how the bubble grows into the bottle at t=0.15 seconds after the bottle has been opened. It can be clearly seen that the bubble stretches more for an increase in angular velocity, with exception of the stationary case. The increase in angular velocity causes a stronger acting centrifugal force which pushes the fluid towards the wall of the bottle. From mass conservation and the weaker acting hydrostatic force on the bubble, it makes it easier for air to entrain, resulting in a further elongated bubble into the bottle. This is depicted in figure 40, where the bubble nearly reaches the parabolic surface at the top of the bottle for the highest angular velocity, whereas for the lower angular velocity cases, the bubble pinches off due to the hydrostatic force. The reason why the bubble grows faster in the bottle for the stationary case in comparison with the 10 rad/s is that rotation can have a stabilising effect on the unstable interface for certain low rotational values. [87] From the literature review, it was found that due to the Coriolis force, a vortex would be generated that would counter-act the vorticity, shown in figure 25, that would be developed due to gravity and the Rayleigh-Taylor instability. However, from the numerical results, it is obtained that the stabilizing Coriolis force only has significant effect on the 10 rad/s case. The centrifugal force overpowers the stabilizing force in higher rotational cases, which causes the increase in growth rate.

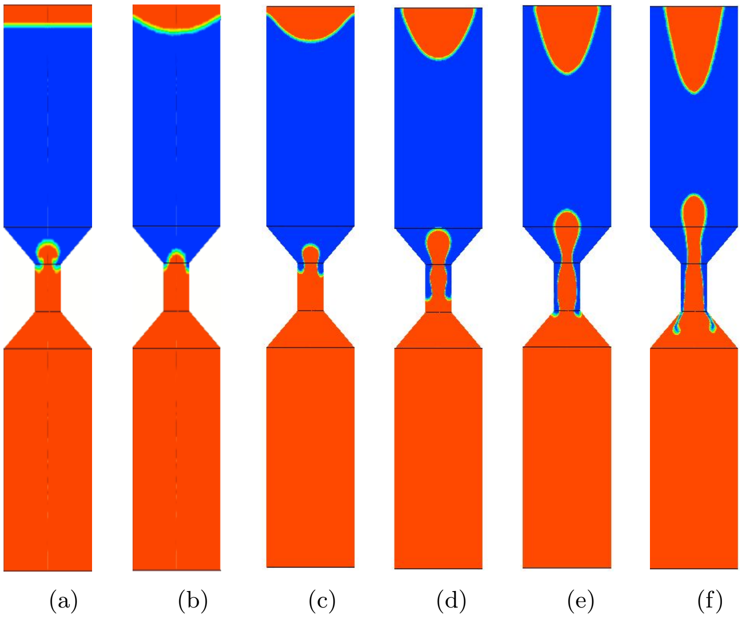

Figure 39: VOF contour (liquid=blue, air=orange) at 0.15 s after opening the bottle for a) 0 rad/s b) 10 rad/s c) 20 rad/s d) 30 rad/s e) 40 rad/s f) 50 rad/s

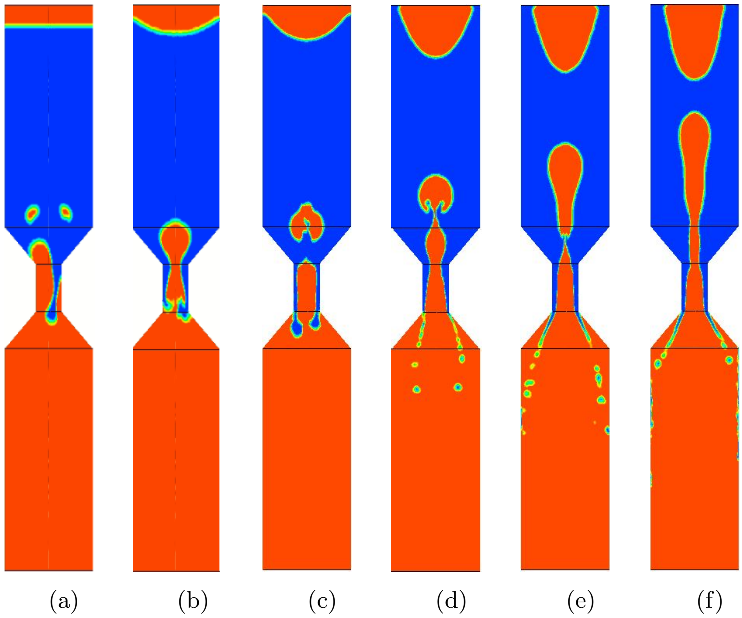

Figure 40: VOF contour (liquid=blue, air=orange) at 0.25 s after opening the bottle for a) 0 rad/s b) 10 rad/s c) 20 rad/s d) 30 rad/s e) 40 rad/s f) 50 rad/s

The height-time graph in figure 38 is enlarged in figure 41 to highlight how the liquid level in the bottom bottle behaves relative to the Π-number in the bubble regime. From figure 41, it appears that an increase in the Π-number (except for 10 rad/s) results in a higher liquid flow rate based on the higher liquid level at the same instant. The increase in liquid flow rate can be explained with the conservation law, which states that the total volume in a closed system can not change. As stated at the beginning of this subsection, due to the stronger centrifugal force, it is easier for the air bubble to elongate into the top bottle. An increase in circumferential velocity induces a stronger centrifugal force and therefore results in more air entrainment. Due to volume conservation, it can be concluded that the same volume of liquid should flow out, generating a higher liquid flow rate out of the top bottle. The stabilizing effect on the growth rate of the Rayleigh-Taylor instability can be clearly seen in figure 41. The first drainage moment for 10 rad/s is significantly later than for the rest of the cases, indicating that the initial rotation stabilized the Rayleigh-Taylor deformation, causing the later starting point of drainage.

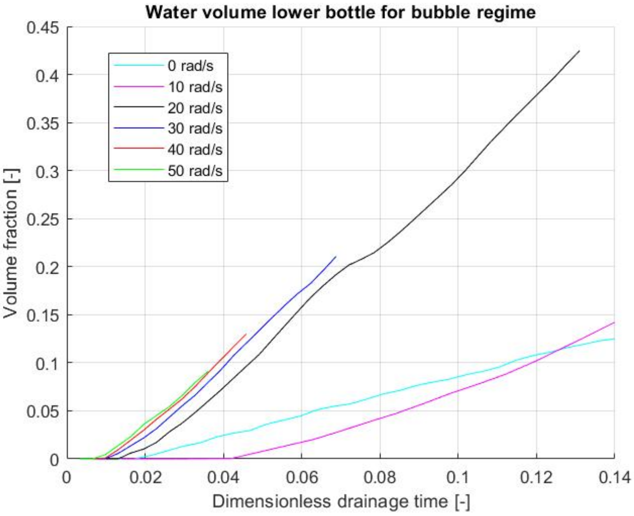

Figure 41: Amount of volume in the bottom bottle during the bubble regime

4.1.3 Transition regime

The transition regime in this study is characterized as where the pressure difference between the atmospheric pressure in the bottom bottle and the under-pressure in the top bottle has disappeared. However, no fully developed air-core vortex has been formed yet. The water layer keeps merging in the center of the bottle. A visual example is shown in figure 42. The hydrostatic force from the liquid layer is stronger than the centrifugal force, which causes the water layers to collapse on each other at the center-line of the bottle. Since the two lowest Π-cases ($\Pi = 0$ and $\Pi = 0.0688$) only stayed in the bubble regime, from here on only the four higher Π-numbers will be discussed.

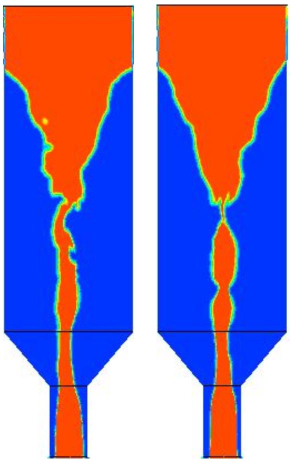

(a) (b)

Figure 42: VOF contour in the transition regime for 30 rad/s a) t=1.05 s b) 1.15 s

What is interesting to notice in this regime, is the volumetric flow rate of glycerine. Since the pressure difference everywhere in the air-layer is close to zero with respect to the atmospheric pressure, it can be assumed that the draining process acts the same as for an open container. In the case for an open container, it is expected that the centrifugal force will only hinder the flow rate and prolong the drainage time. This is due to the centrifugal force pushing the liquid to the wall, which decreases the downward axial velocity. Also, by pushing the liquid to the side, the effective area at the bottle opening of the top bottle will become smaller and thus reducing the liquid flow rate out of the bottle. This was also perceived in figure 37, where the highest area fraction is achieved for $\Pi = 0.2753$ with an initial angular velocity of 20 rad/s in the transition regime ($2 \leq t \leq 2.6$). Comparing this to the graphs shown in figure 43, the flow rate is indeed the highest in the transition regime for 20 rad/s. Especially, from figure 43b it can be seen that the water volume in the bottom bottle was the lowest throughout the bubble regime for 20 rad/s. However, this changes when for 20 rad/s, the flow enters the transition regime, which causes the sudden increase in volumetric flow-rate into the bottom bottle. The slope of the height-time graph shown in figure 43b determines how fast the liquid flows out of the top bottle. The steepness in the transition regime are 0.2293, 0.2161, 0.2046 and 0.2037 L/s for the angular velocities of 20, 30, 40 and 50 rad/s, respectively. From this, it can be concluded that the highest volumetric flow rate is achieved at the beginning of the transition regime, where the centrifugal is relatively weak. During draining, the hydrostatic force becomes weaker, until the centrifugal force is strong enough to fully establish the air-core vortex, which in this specific case lowers the liquid flow rate.

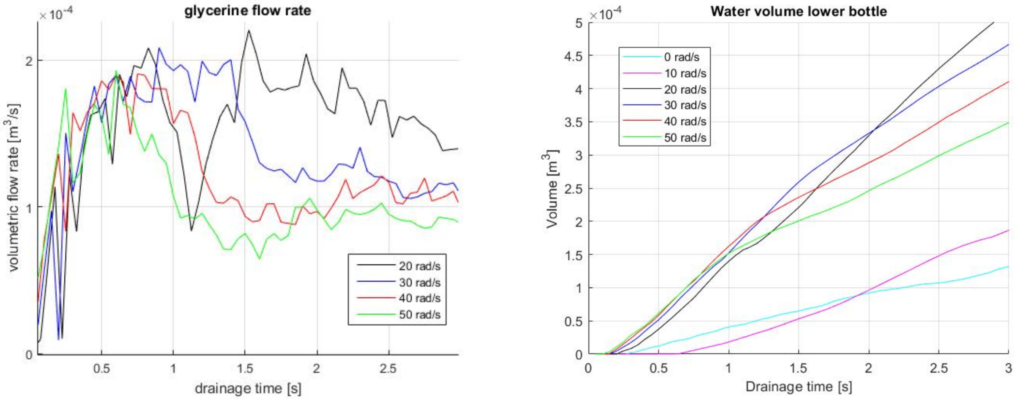

(a) (b)

Figure 43: Enlarged version on the transition regime of the a) glycerine flow rate b) water volume

4.1.4 Vortex regime

The dimensionless parameter Π is a ratio between the centrifugal forces and the hydrostatic forces acting on the fluid. Since it is believed that in the vortex regime a balance is obtained between these two forces, the influence of the Π-number on the characteristics of the vortex flow is investigated in this section.

4.1.4.1 Hypothesis of the force balance in the vortex regime

A hypothesis was made for the vortex regime during the opening section, which stated that the optimal initial rotational velocity should be just high enough to create a small hole at the opening of the bottle, to ensure that the air-core vortex can fully develop into the top of the bottle and erase the under-pressure in the bottle. From this hypothesis, it is expected that the drainage times should be the highest for the cases where no air-core vortex could be generated. This is up until the critical / optimal angular velocity is found, for this case, the drainage time should be the lowest. From there on, an increase in angular velocity should result in an increase of drainage time as well. This theory agreed with the numerical results, as can be seen in table 5, where the lowest drainage time was found for $\Pi = 0.2753$ (20 rad/s).

The hypothesis was based on a simple force balance derived from the cylindrical Navier-Stokes depicted in equations 75-77.

$$\begin{gathered}\rho\left(\frac{\partial u_r}{\partial t}+u_r\frac{\partial u_r}{\partial r}+\frac{u_\theta}{r}\frac{\partial u_r}{\partial \theta}-\frac{u_\theta^2}{r}+u_z\frac{\partial u_r}{\partial z}\right)= \\ -\frac{\partial P}{\partial r}+\rho g_r+\mu\left[\frac{1}{r}\frac{\partial}{\partial r}\left(r\frac{\partial u_r}{\partial r}\right)-\frac{u_r}{r^2}+\frac{1}{r^2}\frac{\partial^2 u_r}{\partial \theta^2}-\frac{2}{r^2}\frac{\partial u_\theta}{\partial \theta}+\frac{\partial^2 u_r}{\partial z^2}\right]\end{gathered} \tag{75}$$

$$\begin{gathered}\rho\left(\frac{\partial u_\theta}{\partial t}+u_r\frac{\partial u_\theta}{r}+\frac{u_\theta}{r}\frac{\partial u_\theta}{\partial \theta}+\frac{u_r+u_\theta}{r}+u_z\frac{\partial u_\theta}{\partial z}\right)= \\ -\frac{1}{r}\frac{\partial P}{\partial \theta}+\rho g_\theta+\mu\left[\frac{1}{r}\frac{\partial}{\partial r}\left(r\frac{\partial u_\theta}{\partial r}\right)-\frac{u_\theta}{r^2}+\frac{1}{r^2}\frac{\partial^2 u_\theta}{\partial \theta^2}-\frac{2}{r^2}\frac{\partial u_r}{\partial \theta}+\frac{\partial^2 u_\theta}{\partial z^2}\right]\end{gathered} \tag{76}$$

$$\begin{gathered}\rho\left(\frac{\partial u_z}{\partial t}+u_r\frac{\partial u_z}{r}+\frac{u_\theta}{r}\frac{\partial u_z}{\partial \theta}+u_z\frac{\partial u_z}{\partial z}\right)= \\ -\frac{\partial P}{\partial z}+\rho g_z+\mu\left[\frac{1}{r}\frac{\partial}{\partial r}\left(r\frac{\partial u_z}{\partial r}\right)+\frac{1}{r^2}\frac{\partial^2 u_z}{\partial \theta^2}+\frac{\partial^2 u_z}{\partial z^2}\right]\end{gathered} \tag{77}$$

When looking at equation 75, it is assumed that the radial pressure gradient $\frac{\partial P}{\partial r}$ will be balanced mainly by the centrifugal force term $\frac{u_\theta^2}{r}$, which results in the following force balance:

$$\rho \frac{u_\theta^2}{r} \sim \frac{\partial P}{\partial r} \tag{78}$$

Based on previous research on velocity profiles in the Taylor-Couette flow [88], it is taken for this hypothesis that the circumferential velocity is only a function of the radius and the angular velocity. The angular velocity of the interface is assumed to be equal to the initial rotational velocity. Therefore, the circumferential velocity can be rewritten as

$$u_\theta(r) = \Omega \cdot r \tag{79}$$

Substituting this in equation 78 and integrating over the radius, the final form of the radial force balance is obtained:

$$\frac{1}{2}\rho\Omega^2(r^2 - r_i^2) \sim P|_r - P|_{r_i} \tag{80}$$

where r is the bottle radius and r_i is the radius of the air-core vortex, $P|_r$ is the pressure at the wall of the bottle, $P|_{r_i}$ pressure at the interface of the air-core vortex and Ω is the angular velocity of the air-core vortex.

When looking in the axial direction of the cylindrical Navier-Stokes equation (equation 77), the assumption is made that the axial pressure gradient $\frac{\partial P}{\partial z}$ will be mainly balanced out by the hydrostatic pressure term ρg_z:

$$\frac{\partial P}{\partial z} \sim \rho g_z \tag{81}$$

By integrating equation 81, the pressure balance in the axial direction is obtained:

$$P|_{z_2} - P|_{z_1} \sim \rho g(z_1 - z_2) \tag{82}$$

In this hypothesis, it is also assumed that the pressure in the air-layer is uniform and equal to the atmospheric pressure, and that the surface tension force due to the curvature of the gas-liquid interface can be neglected.

Figure 44 shows a fully developed air-core. The air layer is shown in orange and the water layer is shown in blue. With the assumption that the LaPlace pressure can be neglected, it can be taken that the pressure on both sides of the interface are the same. This results that the pressure at point 1 and 3 in the liquid layer can be taken to be equal to the atmospheric pressure as well. This is applicable throughout the whole interface, thus $P|_{r_i} \sim P_{atm}$. Rewriting these conditions into equations 80 and 81, the following equations are obtained:

$$P(x,r) \sim P_{atm} + \frac{1}{2}\rho\Omega(r^2 - r_i^2) \tag{83}$$

$$P(x,r) \sim P_{atm} + \rho g \Delta z \tag{84}$$

Combining equations 83 and 84, a balance between the centrifugal and hydrostatic pressure is obtained:

$$\frac{1}{2}\rho\Omega^2\,(r_i^2|_{z+\Delta z} - r_i^2|_z) \sim \rho g \Delta z \tag{85}$$

By dividing the left hand side of equation 85 with the right hand side, the non-dimensional rotational number Π is obtained:

$$\begin{aligned}\Pi &\sim \frac{\rho\Omega^2\,(r_i^2|_{z+\Delta z} - r_i^2|_z)}{\rho g \Delta z}\\ &\sim \frac{\Omega^2 R^2}{gh}\end{aligned} \tag{86}$$

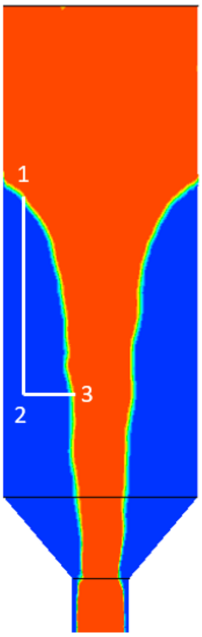

Figure 44: VOF contour with reference points

From equation 85, it can be concluded that the angular velocity (centrifugal force) and the height of the fluid (hydrostatic pressure) are the key parameters for the generation and the shape of the air-core vortex. Equation 85 is the final analytical result of this hypothesis. From this, it is evident that a certain minimum angular velocity is necessary to balance out the hydrostatic pressure to maintain the air-core vortex. After this minimum angular velocity has been reached, an increase in angular velocity results in a stronger centrifugal force overpowering the hydrostatic pressure due to the same initial liquid level. This implies that more liquid will be pushed to the sidewall hindering the fluid from flowing down, resulting in an increase in the drainage time. Thus, after an air-core vortex has been realized in the bottle, it can be expected that an increase in initial angular velocity will be coupled with an increase in drainage time.

4.1.4.2 Proving hypothesis with numerical results

Basing of on the results shown in table 5, it can be concluded that on first sight, the hypothesis conducted in the previous section between the angular velocity and the drainage time is true. However, the hypothesis is based on a few assumptions, such as the fact that the centrifugal force is the only driving force to push the liquid to the sidewall. In this section, the assumptions that were made for the hypothesis will be analyzed and checked whether they were correct or not. With this, more insight will be gained behind the physics and fluid dynamics of the air-core vortex in the bottle.

The first assumption that was established, was that the flow could be characterized as a solid body rotation. The circumferential velocity u_θ in solid body rotation is defined as a function of the angular velocity Ω and the radius r, see equation 79. During the spin-up process, the angular velocity is constant and thus the radial pressure gradient is only a function of the difference in distance in the radial direction. This was verified with the numerical results. In figure 45 it can be seen that the calculated pressure differences based on the assumption, labeled as "matlab" in the figure, and the pressure difference shown in Ansys Fluent, labeled as "ansys", were nearly identical. Only a small difference was noticed, which could be blamed on the coarser mesh that was utilized during the spin-up regime.

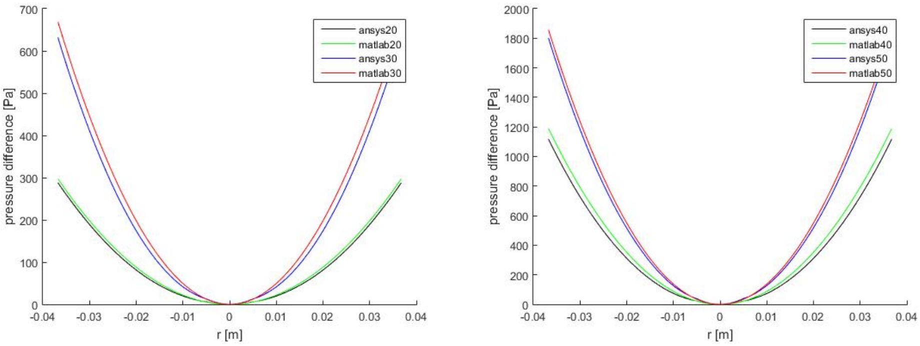

(a) (b)

Figure 45: The radial pressure distribution prior to the drainage (spin-up), taken over a line vector in the x-z plane at a constant height in the middle of the bottle ($x_{\min}$=-0.03675 $x_{\max}$=0.03675 y=0 z=0.3). The reference pressure was taken as 0 at the center point at this height. a) Pressure distribution of angular velocities 20 and 30 rad/s b) Pressure distribution of angular velocities 40 and 50 rad/s

To examine whether the fluid flow still behaves like a solid body rotation during the spin-down process, the circumferential velocity and the angular velocity should still relate with each other by equation 79. The distinction between spin-up and spin-down is that during the spin-down process the angular velocity exhibits transient behaviour due to the instabilities caused by the no-slip boundary condition at the wall. The no-slip boundary condition can be clearly seen in the time-averaged circumferential velocity profile in figure 46b. Hence, it can be concluded that during drainage the fluid flow does not behave as a solid body rotation. Figure 46a displays the circumferential velocity contour at a horizontal plane in the middle of the bottle. From the circumferential velocity contour, it appears that the circumferential velocity is close to being independent of the azimuthal direction and only on the certain height and radius, thus $\sim u_\theta(r, z)$.

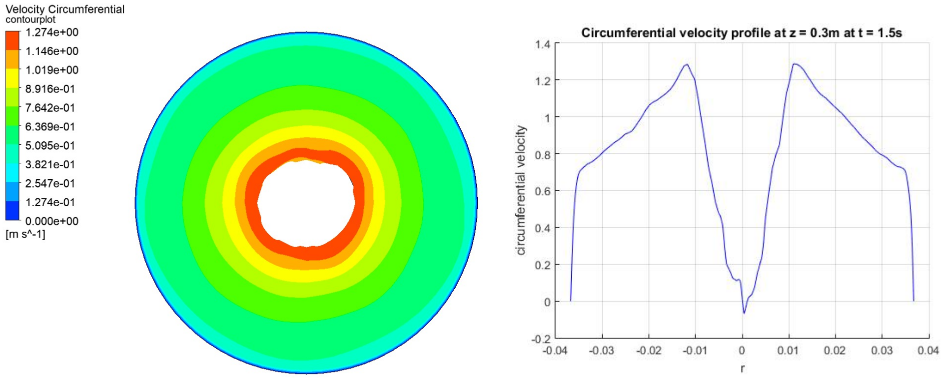

(a) (b)

Figure 46: Circumferential velocity profile at z=0.3 m at t=1.5 s a) Circumferential velocity contour b) Time-averaged circumferential velocity profile

Since it has been established that solid body rotation is not valid, it is interesting to examine how the angular velocity relates to the circumferential velocity. It is expected that the circumferential profile should still look like equation 79, however the angular velocity is not constant anymore, resulting in the following equation:

$$u_\theta(r, z) = \Omega(r, z) \cdot r \tag{87}$$

Since for the Π-number, the interest lies whether the centrifugal force is strong enough to split the fluid interface into the free-surface vortex, first equation 87 was examined and checked whether the relation between the circumferential velocity and the angular velocity at the interface was correct. The result is shown in figure 48. The blue line in the graph shows the numerically calculated value of the circumferential velocity at the corresponding height on the interface. The orange line displays the value of the circumferential velocity by using equation 87, the numerically calculated angular velocity and the radius at the interface. To clarify the values of the height of the bottle displayed on the vertical axis in figure 48, the shape of the interface as well as characteristic points for certain heights are marked in figure 47. From the graph in figure 48, it is visible that the numerically obtained velocities correlate well with equation 87. Therefore, equation 80 is still valid and the centrifugal force can still be expressed with the angular or circumferential velocity.

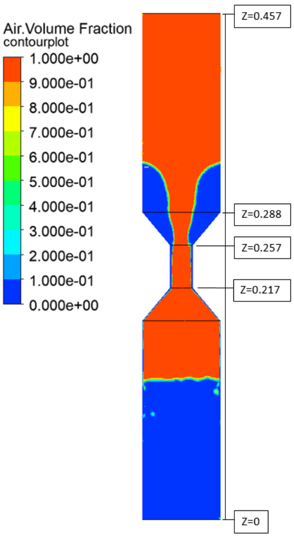

Figure 47: Clarification of the vertical axis of figure 48. All the z-values are in meters.

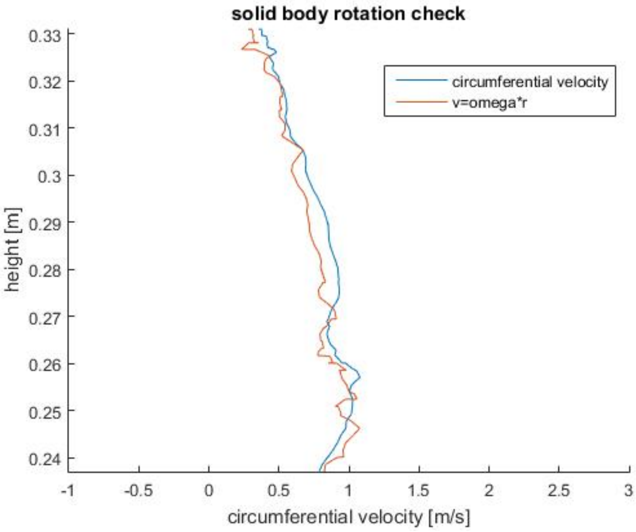

Figure 48: The circumferential velocity plotted against the height of the interface for 50 rad/s

The Π-number consists of two driving forces, the centrifugal force and the hydrostatic force. Before the bottle is opened, everywhere in the bottle, hydrostatic pressure is achieved as shown in figure 50a. Due to the parabolic shape of the interface and the contraction part in the bottle, the pressure contour might seem odd. Nonetheless, $p_{hydro} = \rho g h$ was checked and it was obtained that it was applicable everywhere in the domain. This is different for the case when the drainage process has started. From figure 50b it seems that the pressure close to the side-wall is still hydrostatic. Closer to the centreline, near the bottle opening, this changes into a dynamic pressure gradient, due to no end wall being present. By plotting the hydrostatic pressure over vertical lines in the computational domain, it was obtained that $p_{hydro} = \rho g h$ was applicable everywhere in the fluid except for radii around and smaller than the drain port radius. This is displayed in figure 49. The dotted line labeled as calculated is referred to how

$p_{hydro} = \rho g h$ is calculated, where h is taken as the height difference of the fluid in the computational domain for the different radii. The straight line displays the pressure values shown in figure 50b for different vertical lines. It can be stated that hydrostatic pressure was achieved for all radii ($r > 0.02$ m), except for the radii close to the drain port. Especially for $r = 0.01075$ m, it can be seen that the dynamic pressure gradient influences the fluid significantly, resulting in the big difference between the calculated hydrostatic pressure and the numerically obtained pressure values.

Nonetheless, it can still be established that hydrostatic pressure is valid through most part of the fluid layer. Only the part in the bottle opening where the thin fluid layer flows into the connector, no hydrostatic pressure is present. Hence, it can still be presumed that the driving force pushing the fluid downwards is due to the hydrostatic force, and that the overall force balance between the hydrostatic force and the centrifugal force is still plausible.

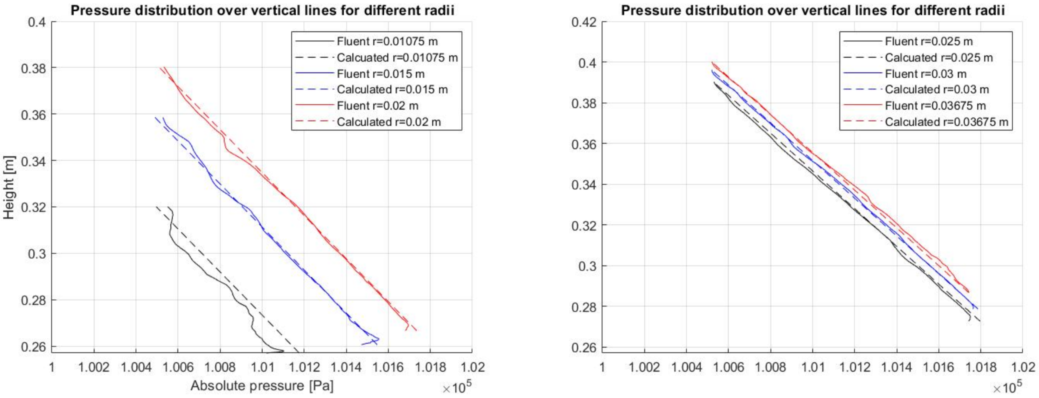

(a) (b)

Figure 49: The pressure distribution over vertical lines over different radii during drainage for Π = 1.7209 at t=1.3 s

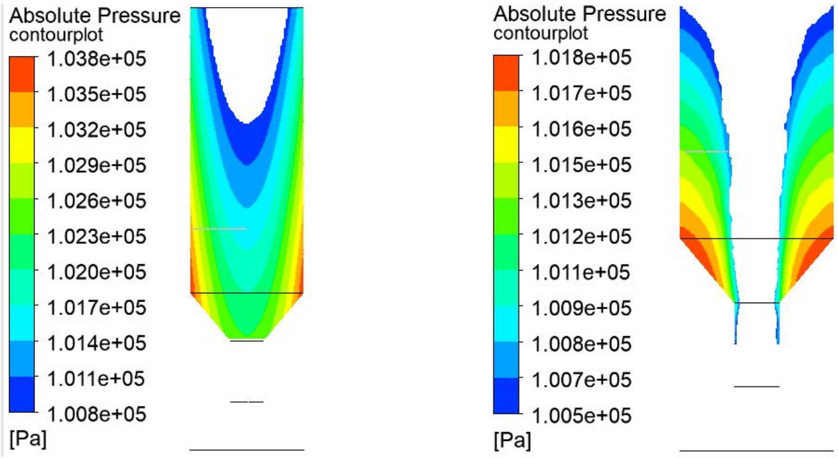

(a) (b)

Figure 50: Absolute pressure contour for the liquid layer for Π = 1.7209 a) before draining b) during draining at t=3.3 s

Even so, the numerical results differed from the hypothesis. The two forces did not balance each other out. The calculated radial pressure difference using equation 80 and the numerically obtained radial pressure difference differed significantly. This is shown in figure 51, where the black line is the pressure difference calculated with equation 80 and the red line is the pressure difference obtained from Ansys. The pressure difference is taken between the interface and the side-wall. The gap between the two lines widens the further it goes down in height, where the largest gap between the two lines was realized right above the connector (z=0.257 m). From there on, in the connector ($0.217 < z < 0.257$), the difference between the two lines became relatively small again. This implies that an extra source or force term that was not accounted for should be considered to equalize the pressure difference above the bottle opening.

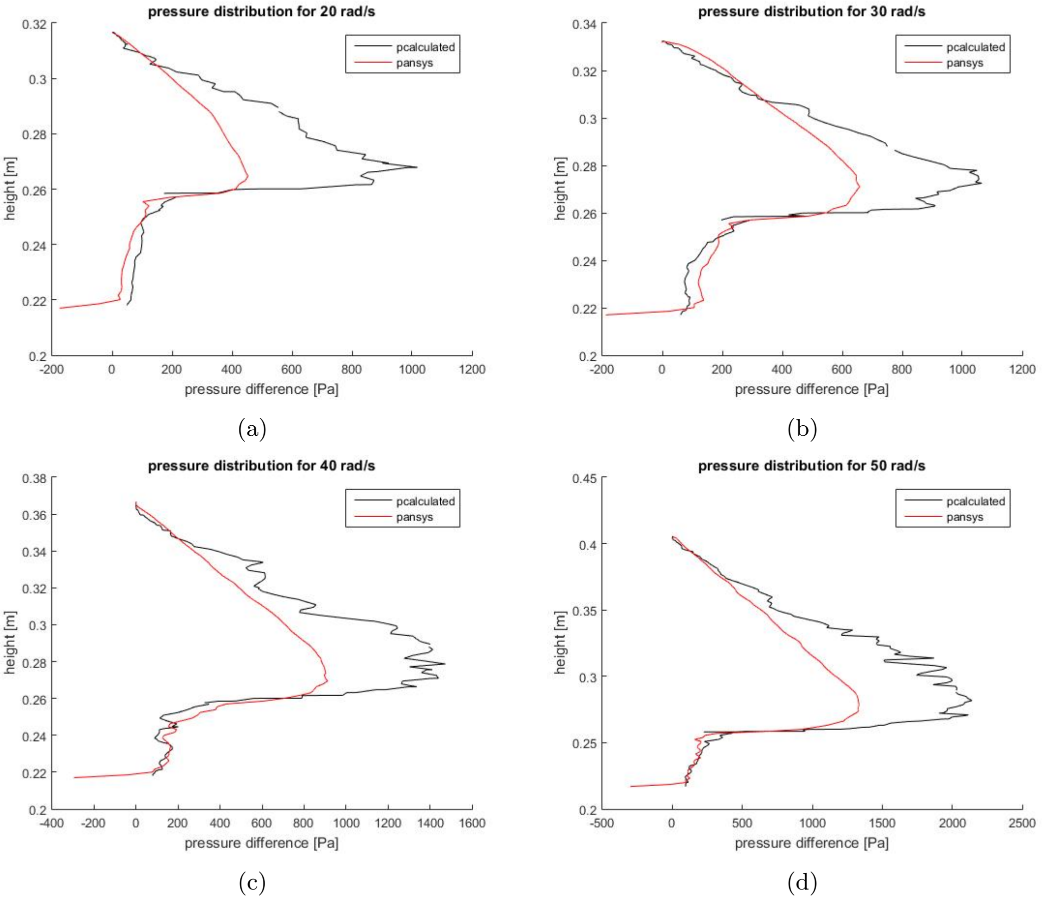

(a) (b) (c) (d)

Figure 51: The radial pressure difference between the interface and the wall of the bottle. The pressure reference point was taken at the highest point of the interface. This is done for the angular velocities at t=2.85 s a) 20 rad/s b) 30 rad/s c) 40 rad/s d) 50 rad/s

When going back to the hypothesis, a few other assumptions were made that have not been verified yet. The first assumption was that surface tension was negligible. The surface tension of 40%-glycerol and 60%-water is 0.07 N/m. The biggest LaPlace pressure jump should be located, where the smallest radius of the interface is, which was around 8 mm. Since at this radius, the curvature in the vertical direction was almost flat, the vertical curvature can be taken as 0. So a quick estimation gives the pressure difference due to the interface at:

$$\Delta p_{Laplace} \approx \gamma \frac{1}{R} = 8.75\,\mathrm{Pa} \tag{88}$$

It can be directly concluded that surface tension alone could not explain the huge pressure difference that is noticed in figure 51. The second assumption was that the radial and axial velocity component had no influence on the force balance and that the fluid flow would remain in solid body rotation.

However, as can be seen from figure 46, the wall effects influence the fluid flow, resulting in deceleration of the fluid flow closer to the wall regions. This results that close to the wall regions, the viscous force term causes the centrifugal and the radial force to be imbalanced, which explains why the overall pressure distribution is lower compared to the expected pressure distribution. When reflecting back to the literature review, another effect occurs due to the stationary wall, which is the generation of Taylor vortices. This is clearly seen in figure 52. Part of the overall velocity will feed the Taylor vortices, resulting in a reduced circumferential velocity and therefore a weaker centrifugal force, which could explain the expected pressure distribution to be lower. From figure 53, it can be observed that the Taylor vortices only influenced the velocity profiles in the mid section of the bottle. No Taylor vortices were observed in the connector part of the water layer depicted in figure 53c ($z < 0.257$) and at the top part of the water layer (figure 53a). This could give a good plausible explanation on why the difference between the black and red line were the highest in the thickest part of the water layer in the bottle and explain why the difference between the two lines are barely noticeable in the connector and the top section of the bottle.

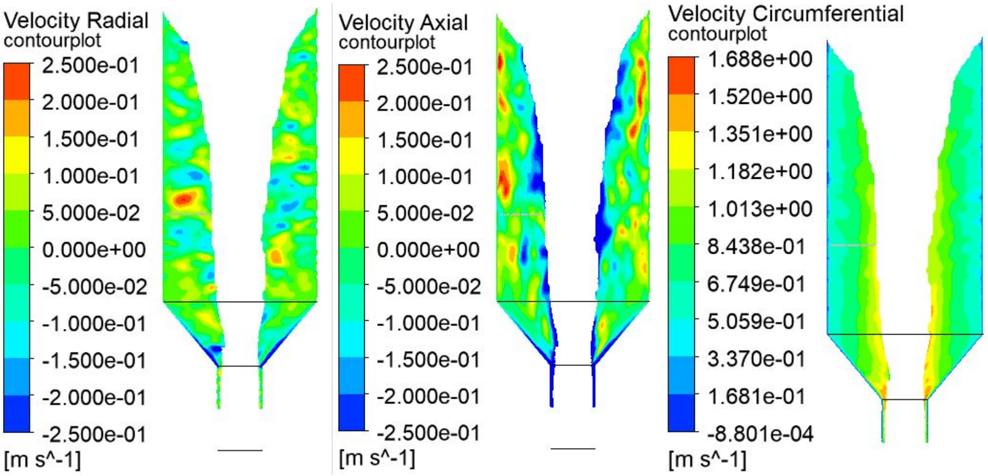

(a) (b) (c)

Figure 52: The velocity contour of the liquid layer at t=2 s for $\Pi = 1.7209$ a) radial b) axial c) circumferential

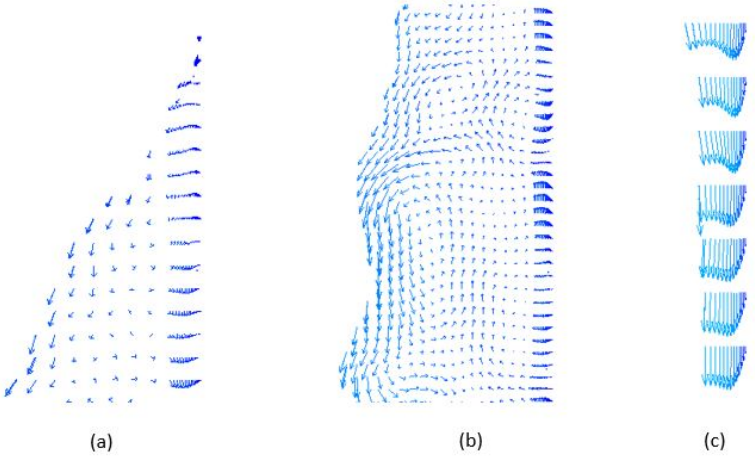

Figure 53: Velocity vector field at t=2 s for $\Pi = 1.7209$ a) Top part of the water layer b) Middle part of the water layer c) Connector part of the water layer

Another effect due to the Taylor vortices is that the flow regime becomes turbulent, which leads to the third and fourth assumptions in the hypothesis. These assumptions were based on the fact that the flow was laminar and viscosity was negligible. To account for the turbulent terms, Reynolds decomposition was used on the radial Navier-Stokes equation, where the velocity is decomposed as $u = \overline{u} + u'$ and $\frac{\partial u_\theta}{\partial \theta} = 0$ is applied.

$$\rho\left(\frac{\partial \overline{u_r}}{\partial t} + \frac{\overline{u_r^2} - \overline{u_\theta^2}}{r} + \frac{\partial \overline{u'_r u'_r}}{\partial r} + \frac{\partial \overline{u'_z u'_r}}{\partial z}\right) = -\frac{\partial \overline{P}}{\partial r} + \mu\left(\Delta \overline{u_r} - \frac{\overline{u_\theta}}{r^2}\right) \tag{89}$$

It is assumed that when the air-core vortex is formed during drainage, the temporal variation in the mean flow is weak and therefore the unsteady term can be neglected. Also, it is expected that the effect of viscous diffusion is negligible in the mean flow. Only close to the wall region will the viscous term influence the flow. This was also compared with the numerical results. The viscosity term in equation 89 consists of two terms. It was found that the first term $\mu\Delta\bar{u}_r$ was close to zero in the bulk region. The second viscosity term in equation 89 ($\mu\frac{\overline{u_\theta}}{r^2}$) resembles the centrifugal force term with an additional viscosity term. It was calculated that due to the value of viscosity (μ=3.63e-03 kg/ms), the second viscosity term was significantly smaller than the centrifugal force in the bulk region. Therefore, the viscous term in equation 89 will also be neglected. This reduces equation 89 to:

$$\rho\left(\frac{\overline{u_r^2} - \overline{u_\theta^2}}{r} + \frac{\partial \overline{u'_r u'_r}}{\partial r} + \frac{\partial \overline{u'_z u'_r}}{\partial z}\right) = -\frac{\partial \overline{P}}{\partial r} \tag{90}$$

When we compare this to equation 78, three new terms appears in the force balance. The first term is the $\frac{\overline{u_r}^2}{r}$. A comparison between this term and the centrifugal term was made. From the numerical results, it was found that the mean circumferential velocity was 25 times larger than the mean radial velocity in the liquid layer, which implied that $u_\theta^2 \gg u_r^2$ and thus the first term was negligible. The second and third term are the fluctuating velocity terms, which arises when Reynolds decomposition is applied on the Navier-Stokes equation. A possible reason behind the difference between the calculated pressure difference and the numerically obtained pressure difference is due to the turbulent nature of the flow regime. Part of the kinetic energy driven due to the centrifugal force can get lost to generate the Taylor vortices and feed the turbulent flow. Therefore, more centrifugal force is necessary to push the fluid to the side. Even though the turbulent nature and the wall region influences the radial pressure gradient, it can be fair to say that the two driving forces generating the air-core vortex are still the centrifugal force and the force due to the hydrostatic pressure. Note that when the turbulent fluctuations can be ignored in equation 90, equation 78 is obtained and ergo the Pi number.

4.1.4.3 Π-criterion

Since it was validated in the previous section that the balance between the centrifugal force and the hydrostatic force is still crucial for the generation of the air-core vortex, the next logical step is to determine whether a critical Π-number exists. The critical Π-number is defined as the number where below the critical Π-number, the fluid flow will stay in the bubble regime, whereas the air-core vortex should be present in the system for values above the critical Π-number.

A strong correlation was already obtained from the numerical results between the moment when the air-core vortex was present in the bottle and the angular velocity. The lower the angular velocity, the later the air-core vortex was realised. The exact moment when the air-core vortex was realised for the first time is shown in table 6.

Angular velocity [rad/s]	Timestamp [s]
20	2.6
30	1.25
40	0.85
50	0.7

Table 6: The earliest time value for when a fully developed air-core vortex is noticed

The decrease of the necessary time to generate the air-core with an increase in angular velocity can be explained using the force balance. By initializing the bottle with a lower angular velocity, the centrifugal force also becomes weaker. If the centrifugal force is weaker than the liquid layer pushing from above due to the gravitational force, the fluid flow will stay in the bubble regime. The flow will continue to remain in the bubble regime, until the liquid level has descended sufficiently for the hydrostatic force and the centrifugal force to be in balance. When the balance is achieved, the first part of the of the air-core vortex formation should be noticed in the bottle. Thus, initializing with a low angular velocity means that more liquid has to flow out of the bottle before a balance between the centrifugal force and the hydrostatic force is obtained. This implies that the generation of the air-core vortex will happen in a later stage for the lower angular velocity compared to the higher angular velocity cases. This can also be seen in figure 54, where the circumferential velocity contours for each of the angular velocities are depicted at the timestamp shown in table 6. The color contour is the same for every sub-figure. As can be seen from figure 54, the higher the liquid level, the higher the circumferential velocity has to be for the air-core to appear. This all proves that the Π-number has a significant effect on the generation of the air-core vortex and a critical value for the Π-number should exist. The study on the critical Π-number will be continued and discussed in more detail in section 4.1.6 and 4.1.7.

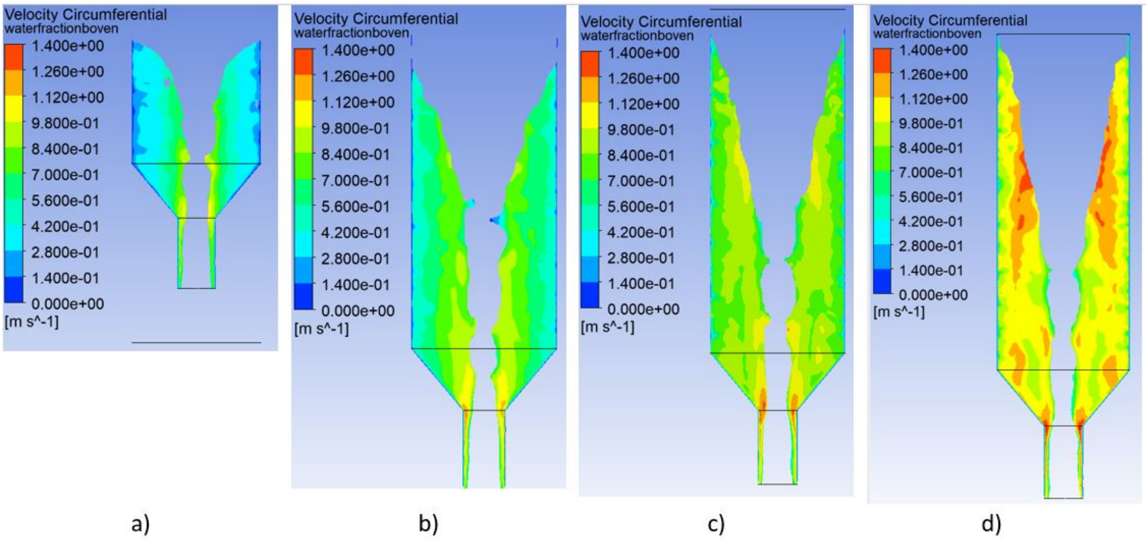

Figure 54: The circumferential velocity contour where the contours match the time values depicted in table 6 a) 20 rad/s b) 30 rad/s c) 40 rad/s d) 50 rad/s

It is also interesting to study how the value of Π behaves with the onset of the vortex regime. The onset Π-number is defined as how the centrifugal force relates to the hydrostatic force at the exact moment when the air-core vortex is generated. Ideally, it is expected that the ratio between these two forces should remain the same for all the cases, meaning an increase in angular velocity should result in the same increase of hydrostatic force at the moment the air-core vortex is generated. The onset Π-number is defined as the averaged circumferential velocity of the liquid layer at the moment the vortex is formed (Ω_{mean}) times the averaged interface radius (R_{mean}) divided by the gravity times the liquid level difference ($h(z) - h_0$) at the moment the air-core is generated:

$$\Pi_{onset} = \frac{(\Omega_{mean} R_{mean})^2}{g(h(z) - h_0)} \tag{91}$$

where h_0 is the height at the bottle opening at z=0.257 m (see figure 47 for a clarification of the height).

It is observed that the onset Π-number fluctuates between the different cases, shown in figure 55. From figure 55, it can be observed that more data points are taken than previously discussed. Next to the

Π-numbers shown in table 4, additional Π values of 0.4302, 0.8432 and 1.3939 were studied on the onset Π-numbers. Even though the results fluctuated, the deviation is relatively small between every case (red line) and the mean value (blue dotted line) of these cases, where the mean onset Π-number is equal to 0.3845. Therefore, it is believed that when the air-core vortex is created, the onset Π-number should be around the same value for every case, despite no exact value was obtained for the onset Π-number.

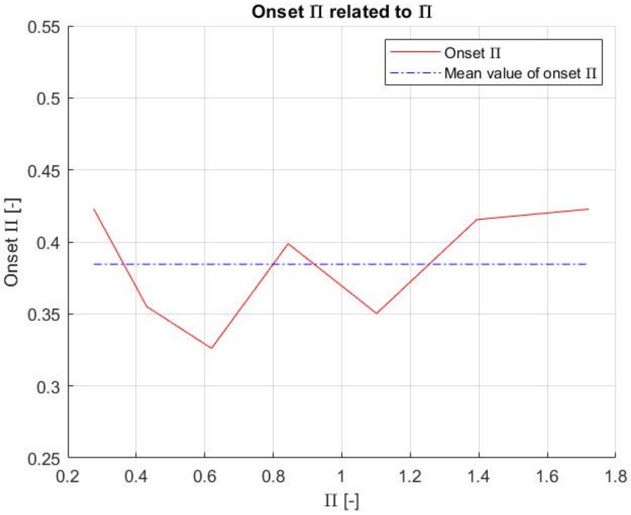

Figure 55: The critical Π-number (red) and the onset Π-number (blue) related to the initial angular velocity Ω.

4.1.5 Swirl stage

The last stage in the draining process is defined as the swirl stage. The swirl stage is characterized as the draining period, where the last fraction of the liquid gets stuck in the top bottle due to the fluid circulating in the contraction part. A part of the swirl stage is visualized in figure 56. Due to the absence of the hydrostatic force, the centrifugal force has free rein, resulting in the fluid just spinning around its vertical axis without moving down. To obtain a better understanding on how strong the centrifugal force is with respect to the hydrostatic force, the onset Π-number in this stage is around 8, whereas the onset Π-number was not even higher than 0.45 in the beginning phase of the vortex regime. From figure 88, it can be seen that in the swirl stage, no glycerine is flowing out of the bottle, up until the liquid fluid has decelerated enough. The remaining fluid then drops down into the bottom bottle, which explains the peak in the flow rate right before the end. However, prior to the peak, a certain amount of time passes with no flow rate and thus this stage is characterized as the most inefficient draining period. From table 5, it can be seen that an increase in angular velocity results in a longer drainage time for the swirl stage. This is due to the fact that an increase in angular velocity results in a longer deceleration time before the fluid is able to fall down into the connector.

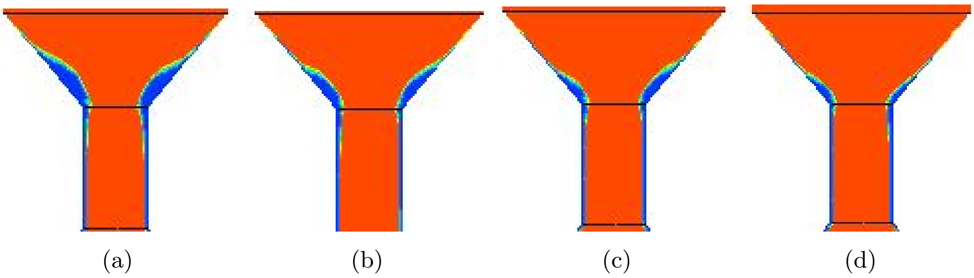
(a) (b) (c) (d)

Figure 56: swirl stage of 50 rad/s with a time-interval of 0.1 s

4.1.6 Hypothesis: relation between Π and drainage time

An analytical attempt is made to describe how the Π-number is related to the drainage time. The relation is based on the analytical results obtained in this section. This will be compared with the numerical results in the next section.

From equation 85, the force balance for the generation of the air-core vortex is obtained. By applying the force balance for the bottle opening, the following is acquired:

$$\frac{1}{2}\rho\Omega_h^2(r^2 - r_i^2) \sim \rho g h \tag{92}$$

where Ω_h is the angular velocity of the interface at the bottle opening. The radius difference between the bottle neck and the interface $(r^2 - r_i^2)$ can be rewritten as: $((r_i + \delta)^2 - r_i^2)$, where r_i is the radius of the interface from the center-line and δ the boundary layer thickness taken between the interface and the wall. It is assumed for the simplicity of this analytical analysis that the boundary thickness is significantly smaller than the interface radius, therefore ($\delta^2 \simeq 0$ and $r_i \simeq r_h$). The sizes are displayed in figure 57a to obtain a better visualization of the different radii and the boundary layer.

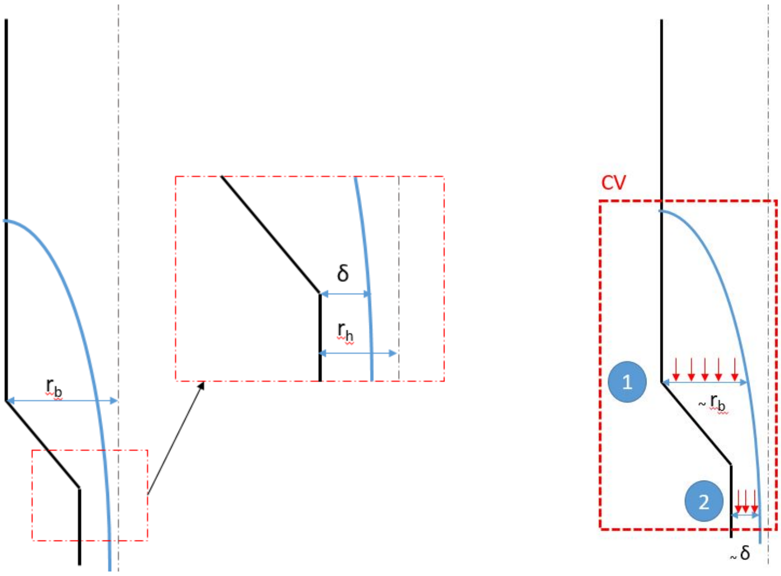

(a)

(b)

Figure 57: a) Elaboration of important parameters b) Control Volume over the top bottle

Applying the simplicity assumption about the boundary layer ($\delta^2 \simeq 0$ and $r_i \simeq r_h$), the radius difference can be written as:

$$(r_i + \delta)^2 - r_i^2 \sim 2r_i\delta \sim 2r_h\delta \tag{93}$$

Substituting this into the force balance equation (equation 92), a relation between the boundary layer and the local Π-number in the bottle opening is found:

$$\begin{gathered}\rho_l\Omega_h^2 2r_h\delta \sim \rho_l g h \\ \delta \sim \frac{gh}{\Omega_h^2 r_h}\end{gathered} \tag{94}$$

Applying conservation of momentum, the boundary layer thickness can be expressed with the Π-number:

$$\begin{gathered}\Omega_h r_h^2 \sim \Omega_b r_b^2 \\ \delta \sim \frac{ghr_h^3}{\Omega_b^2 r_b^4} = \frac{1}{\Pi}\frac{r_h^3}{r_b^2}\end{gathered} \tag{95}$$

Note that the boundary layer thickness increases for a decrease in the initial angular velocity. This still satisfies the underlying physics of the air-core vortex. Since a relation between the boundary layer thickness and the Π-number is already attained, the next step is to link the drainage time with the boundary layer. For this, a control volume is taken over the whole top bottle. The control volume is displayed in figure 57b. With this control volume, the boundary layer can be expressed in the mass balance. Integrating this over time and a relation between the drainage time and Π is obtained. It is assumed that the fluid layer moves down with an average bulk velocity of $-\frac{dh}{dt}$ and the area where the fluid flows down through scales in the same order as with the radius of the bottle radius ($\sim r_b$), resulting in the following mass balance:

$$-\frac{dh}{dt}r_b^2 \sim u_h((r_i+\delta)^2 - r_i) \tag{96}$$

where u_h is the velocity out of the bottle opening of the fluid layer. The left side of equation 96 represents the mass flow at layer 1, shown in figure 57b, whereas the right side represents the mass flow out of the top bottle at layer 2.

4.1.6.1 Laminar regime

The velocity u_h can be expressed by applying the vertical force balance in the bottle opening between the wall shear force and the hydrostatic force. Note that the relation for the wall shear stress, depicted in equation 97 is only valid when the flow is laminar in the bottle connector.

$$\begin{aligned} \rho_l g r_h \delta L &\sim \tau_w r_h L \\ \tau_w &\sim \mu \frac{u_h}{\delta} \end{aligned} \tag{97}$$

Substituting the wall shear stress and a relation is found between the bottle opening velocity and the boundary layer:

$$u_h \sim \frac{g\delta^2}{\nu} \tag{98}$$

Substituting equation 98 into equation 96 and integrating over time, the relation between the liquid level and the drainage time is obtained:

$$\begin{aligned} -\frac{dh}{dt}r_b^2 &\sim \frac{g\delta^2}{\nu} r_h \delta \\ \frac{h}{h_0} &\sim \frac{1}{\sqrt{1+\beta h_0^2 \frac{g r_h}{\nu r_b^2}\left(\frac{g r_h^3}{\Omega_b^2 r_b^4}\right)^3 t}} \end{aligned} \tag{99}$$

where β is a coefficient that has to be determined empirically. Rewriting this in a more general form, the following is obtained:

$$\frac{h}{h_0} \sim \frac{1}{\sqrt{1+\frac{t}{t_{d,lam}}}} \tag{100}$$

where the typical laminar drainage time $t_{d,lam}$ is defined as:

$$\begin{aligned} t_{d,lam} &\sim \frac{1}{h_0^2 \frac{g r_h}{\nu r_b^2}\left(\frac{g r_h^3}{\Omega_b^2 r_b^4}\right)^3} \\ &\sim \Pi^3 \, \frac{\nu}{g} \frac{r_b^8 h_0}{r_h^{10}} \end{aligned} \tag{101}$$

Fastest drainage is obtained when the boundary layer in the bottle opening is approximately equal to the radius of the bottle opening, thus $\delta \sim r_h$. Therefore, by substituting this boundary layer thickness into equation 99, the minimal drainage time $t_{min,lam}$ can be obtained:

$$\begin{aligned} -\frac{dh}{dt}r_b^2 &\sim \frac{gr_h^2}{\nu}r_h^2 \\ \frac{h_0}{t_{min,lam}} &\sim \frac{g}{\nu}\frac{r_h^4}{r_b^2} \\ t_{min,lam} &\sim \frac{h_0 \nu r_b^2}{g r_h^4} \end{aligned} \tag{102}$$

How the drainage time grows with the minimal drainage time turns out to be a function of the Π-number. This is displayed below:

$$\begin{aligned} \frac{t_{d,lam}}{t_{min,lam}} &\sim \frac{\Pi^3 \frac{\nu}{g}\frac{r_b^8 h_0}{r_h^{10}}}{\frac{h_0 \nu r_b^2}{g r_h^4}} \\ &\sim \Pi^3 \left(\frac{r_b}{r_h}\right)^6 \end{aligned} \tag{103}$$

4.1.6.2 Turbulent regime

In the previous analytical solution, it was taken that the flow in the bottle connector is laminar. However, the fluid flow can also become turbulent in the bottle connector. Therefore, an analytical solution is also obtained for the turbulent regime. Up until equation 96, the solution remains the same for both regimes. The difference between the laminar and turbulent solution is obtained when defining the wall shear stress. From equation 60, it was already found that the turbulent shear stress relates to the velocity as:

$$\tau_w \sim c_f \rho u_h^2 \tag{104}$$

Substituting this in the axial force balance in equation 97, the following relation is acquired:

$$u_h^2 \sim \frac{g\delta}{c_f} \tag{105}$$

When applying the new relation for the bulk velocity in the mass balance, the turbulent relation between the liquid level and the drainage time is obtained:

$$\begin{aligned} -\frac{dh}{dt}r_b^2 &\sim \sqrt{\frac{g\delta}{c_f}}r_h\delta \\ \frac{h}{h_0} &\sim \frac{1}{(1+\gamma\frac{g^2 r_h^{11/2} h_0^{1/2}}{\Omega_b^3 r_b^8 \sqrt{c_f}}t)^2} \\ &\sim \frac{1}{(1+\frac{t}{t_{d,turb}})^2} \end{aligned} \tag{106}$$

where γ is an empirical coefficient. The turbulent drainage time $t_{d,turb}$ can then be defined as:

$$\begin{aligned} t_{d,turb} &\sim \frac{\Omega_b^3 r_b^8 \sqrt{c_f}}{g^2 r_h^{11/2} h_0^{1/2}} \\ &\sim \sqrt{\frac{c_f}{g r_h}} h_0 (\frac{r_b}{r_h})^5 \Pi^{3/2} \end{aligned} \tag{107}$$

It is believed that $r_h \simeq \delta$ has to be satisfied to obtain the minimum drainage time. Rewriting equation 106 in terms of the minimal drainage time, the following is obtained:

$$\begin{aligned} \frac{h_0}{t_{min,turb}} &\sim \sqrt{\frac{g\delta}{c_f}} r_h \delta \frac{1}{r_b^2} = \sqrt{\frac{g}{c_f}} \frac{r_h^{5/2}}{r_b^2} \\ t_{min,turb} &\sim \sqrt{\frac{c_f}{g}} \frac{r_b^2 h_0}{r_h^{5/2}} \end{aligned} \tag{108}$$

How the drainage time grows with the minimal drainage time turns out to be a function of the Π-number. This is displayed below:

$$\frac{t_{d,turb}}{t_{min,turb}} = \frac{\frac{\Omega_b^3 r_b^8 \sqrt{c_f}}{g^2 r_h^{11/2} h_0^{1/2}}}{\sqrt{\frac{c_f}{g} \frac{r_b^2 h_0}{r_h^{5/2}}}} \simeq \Pi^{3/2} \tag{109}$$

So, to summarize the findings:

$$t_{drainage} \sim \Pi^3 \qquad \text{for laminar regime} \tag{110}$$

$$t_{drainage} \sim \Pi^{3/2} \qquad \text{for turbulent regime} \tag{111}$$

It can be stated from the analytical results that the drainage time is a function of the Π-number to the power of 3 if the flow regime in the bottle connector is laminar, if it is turbulent the drainage time is a function to the power 3/2. Note that the following relation was substantially simplified to obtain the analytical result. However, from the numerical results, it was already found that the minimum drainage time is correlated with the critical angular velocity. It is believed that the drainage time scales and grows with Π^3 or $\Pi^{3/2}$ beyond the critical Π-number. This hypothesis is displayed in figure 58, where the minimum of the parabola is related to the minimum drainage time and the critical Π-number. From there on in the vortex regime (pink area), the line develops in the third power or 3/2, depending on the flow regime.

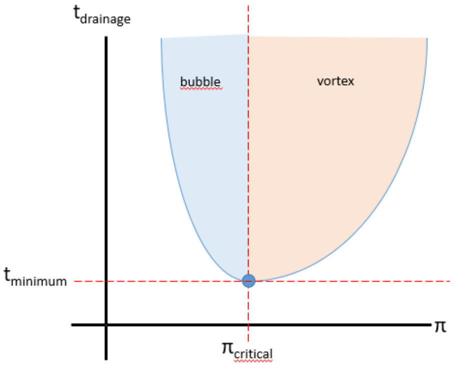

Figure 58: Expected relation between Π and drainage time

4.1.7 Conclusion hypothesis Π-drainage time relation

The hypothesis of the curve was tested and will be compared with the numerical results in this section. The result from the analytical calculation was that the drainage time would grow in the power to the third or 3/2 of the Π-number, depending on the flow regime. Before the comparison between the analytical and numerical solutions will be shown, first a few assumptions has to be checked whether they were valid or not. In particular, equations 94 and 95 will be cross-checked with the obtained numerical results. The comparison between equations 94 (red line), 95 (blue line) and the numerical results (black line) is plotted in figure 59. As can be seen in figure 59, more data points are present than previously discussed in the Π-case. A full overview of all the data points used for this conclusion is depicted in table 7.

Angular velocity [rad/s]	Π
0	0
5	0.0172
10	0.0688
15	0.1549
17	0.1989
20	0.2753
25	0.4302
27	0.5018
28	0.5397
30	0.6195
31	0.6615
35	0.8432
40	1.1014
45	1.3939
50	1.7209

Table 7: Different testcases for the Π-case

The numerically obtained fluid thickness δ is derived from the effective area A_{liquid} through the following:

$$A_{liquid} = \frac{1}{4}\pi(d_h^2 - (d_h - \delta)^2) \tag{112}$$

where d_h is the diameter of the bottle opening. The effective area A_{liquid} is numerically obtained by:

$$A_{liquid} = \frac{\sum \alpha_{liquid}(i,j,k) \cdot A_{cell}(i,j,k)}{\sum \alpha_{liquid}(i,j,k)} \tag{113}$$

where $A_{cell}(i,j,k)$ is the cell area of that specific cell. For equation 94, the angular velocity in the bottle opening was needed. This was numerically obtained by calculating the mean angular velocity in the bottle connector for every time-step and then averaged over all the time-steps. As can be seen in figure 59 does the calculated values for the fluid thickness differ. However, since equations 94 and 95 are order estimations instead of quantitative results, the course of the line gives a better indication whether the relations are valid or not. Even though equation 94 and 95 do not align perfectly with the numerical results, it can still be concluded that the course of the lines correlate well between each other.

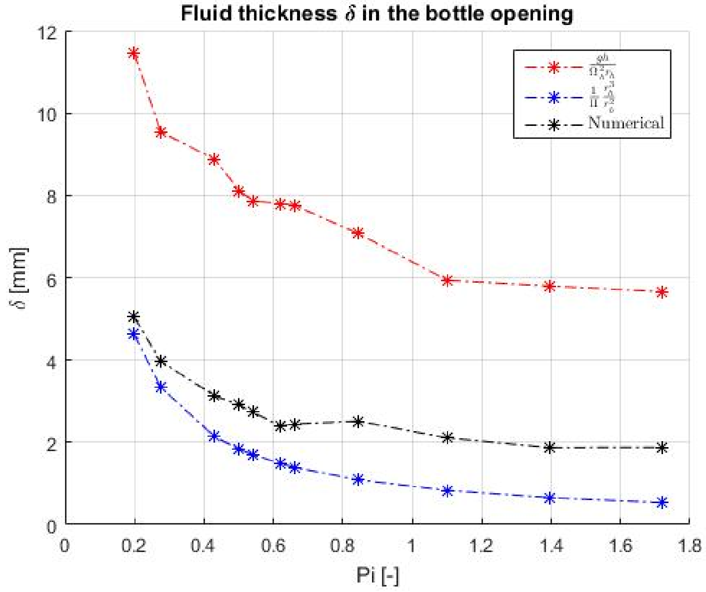

Figure 59: Comparison between the estimated relations for the fluid thickness (red and blue lines) and the numerically obtained fluid thickness (black line).

Also, the flow regime in the bottle connector should be determined, since the relation between the non-dimensional drainage time and Π differ, dependent on the flow regime. One way to prove the flow regime is by plotting both sides of equation 97. This is depicted in figure 60. Since plotting all the results for equation 97 from the data points in table 7 in figure 60, this would result in a chaotic graph. Therefore, only the four angular velocities are presented in the graph that were also discussed through the whole Π case. At every time-step in the vortex regime, the wall shear stress was calculated. Since the wall shear stress was related to the bulk velocity divided by the liquid layer in the bottle opening, at every time-step the liquid layer thickness δ was derived from the effective area A_{liquid} depicted in equation 112 and the bulk velocity u_b was derived from the liquid flow rate Q_{liquid} as:

$$u_b = \frac{Q_{liquid}}{A_{liquid}} \tag{114}$$

At every time-step the shear force was plotted against the spatial gradient $\frac{du}{dy} = \frac{u_h}{\delta}$. It is expected that a linear relation should be obtained in the plot to prove the laminar nature of the flow. As can be observed from figure 60, the linear relation is indeed realized for 20 and 30 rad/s. However, for 40 and 50 rad/s, it can be observed that an exponential increase is noticed in the right top corner. It was found that these are related to the first half of time interval in which the vortex regime is present, where in the bottle connector, the flow still was turbulent. Therefore, it is concluded Π should grow to the power third for 20 and 30 rad/s, whereas for 40 and 50 rad/s Π should grow to the power 3/2..

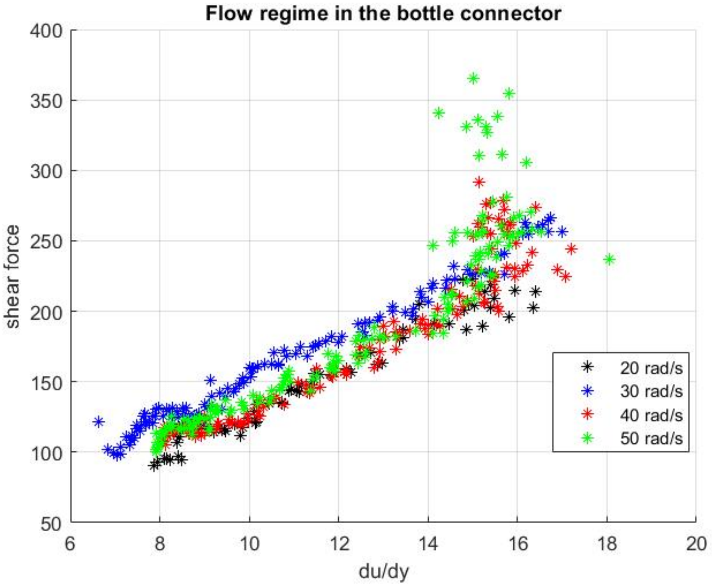

Figure 60: Every data point in the plot represents one time-step, where the calculated shear force is compared to the spatial gradient of $\frac{u_h}{\delta}$

The numerical drainage time over Π is depicted in figure 61, where it is made dimensionless with the stationary drainage time shown in equation 10. Three lines can be seen in the graph, where the black line shows the numerically calculated drainage times for the corresponding angular velocities. The blue line shows how Π^3 scales with the drainage time starting from the minimal drainage time. The red line shows how $\Pi^{1.5}$ scales with the drainage time starting from the Π-number, where the flow regime in the bottle connector turns turbulent. It is observed that the critical Π number is equal to $\Pi = 0.1989$. Also, a critical transition Π number is found for a value of $\Pi = 0.5397$. Comparing the two lines, it can be seen that both lines correlate well with the numerical results.

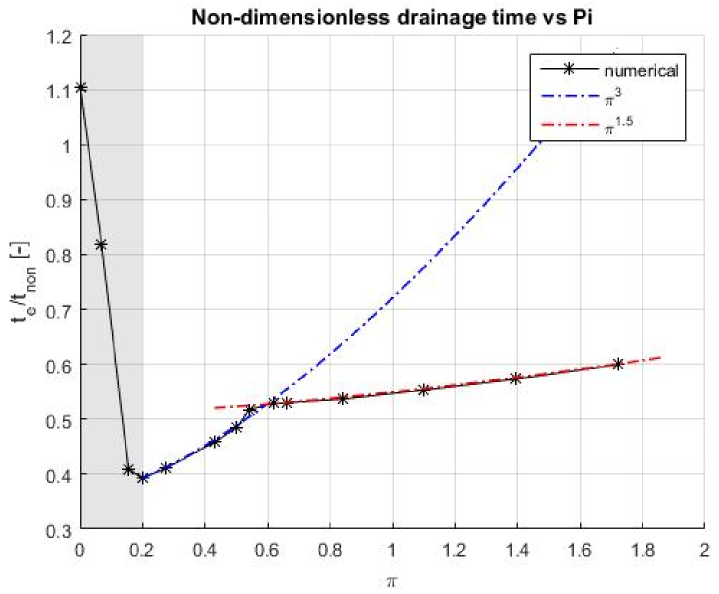

Figure 61: The numerical results for the relation between the drainage time and Π. The numerical results are shown as the black line. The grey area represents the bubble regime. The blue dotted line shows the development of the laminar relation (Π^3). The red dotted line shows the development of the turbulent relation ($\Pi^{1.5}$).

4.2 Case 2: Influence of the Morton number

Case 1 characterized the vortex regime and how the Π-number influenced the vortex regime and the drainage time. The fluid properties will be altered in the next two cases. The influence of the Morton number will be tested in this section. To keep the Π-number constant, the initial angular velocity and height had to remain constant. It was ensured that the selected Π-number was high enough, for the air-core to be formed. If the centrifugal force is not strong enough for all the cases to form this air-core, the drainage time will increase significantly and therefore the sole effect of the Morton number can not be studied correctly. An example is given in section 4.2.6, where the Morton number has been excessively increased, resulting in the Π-number being lower than the critical Π-number. How the critical Π-number changes due to an alteration of the Morton number will be discussed in this section.

To keep the Eötvos number constant, the liquid properties except for the viscosity should remain constant. with their fluid propertiesHowever, by using existing fluids with physical properties, it was difficult to find a fluid that can change its viscosity without altering the other fluid properties. For glycerol-water, it was found that by altering the glycerol weight percentage, the viscosity increases significantly relative to the density and the surface tension. This was based on experimental data by Takamura et al [89]. The properties of the fluid can be seen in table 8, where 3 different weight percentages were used for this case. The Morton number increased 3 times (45%-glycerol) and 8.6 times (50%-glycerol) with respect to the 40% glycerol, whereas the Π-number stayed equal due to the same initial angular velocity and height. The Eötvos number only increased by 0.018 times (45%-glycerol) and 0.037 times (50%-glycerol). Therefore, it was stated that the effect of the increase on the Eötvos number was negligible and thus the effect of the Morton number could be investigated with these weight percentages of glycerol.

Glycerol-%	40%	45%	50%
Morton	4.5145e-09	1.3850e-08	3.8696e-08
Density	1100	1114	1128
Viscosity	0.00363	0.0048	0.0062
Surface tension	0.07	0.069625	0.06925
Π	0.5619	0.5619	0.5619
Eötvos	61.5954	62.7161	63.8491

Table 8: Different test cases with their fluid properties for the Morton case

4.2.1 Draining regimes

The different parameters over time are shown in figure 62, 63 and 64. Also, the averaged circumferential velocity of the liquid layer over time is displayed in figure 65. The drainage time per regime for every case is depicted in table 9. The graphs and table will be elaborated further in this section.

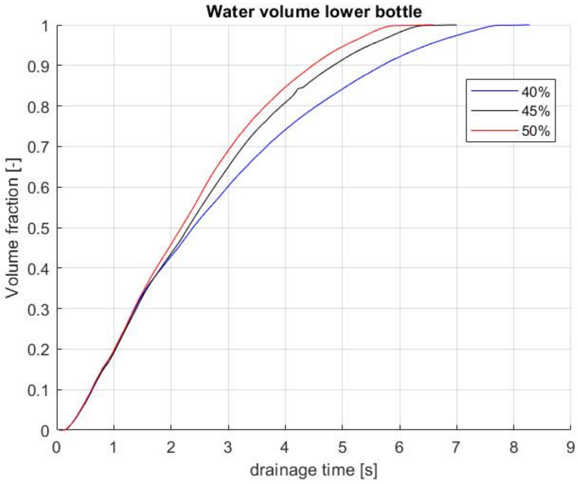

Figure 62: Volume over time for the bottom bottle

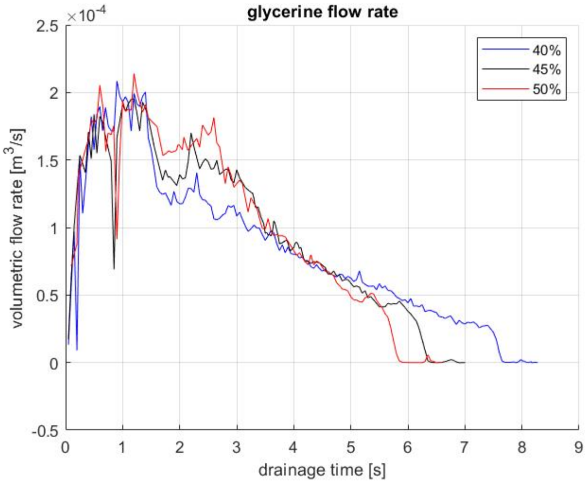

Figure 63: Glycerine flow rate out of the bottle opening

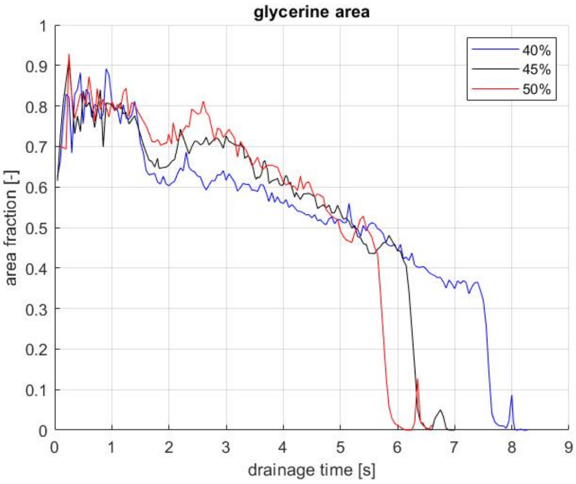

Figure 64: Glycerine area in the bottle opening

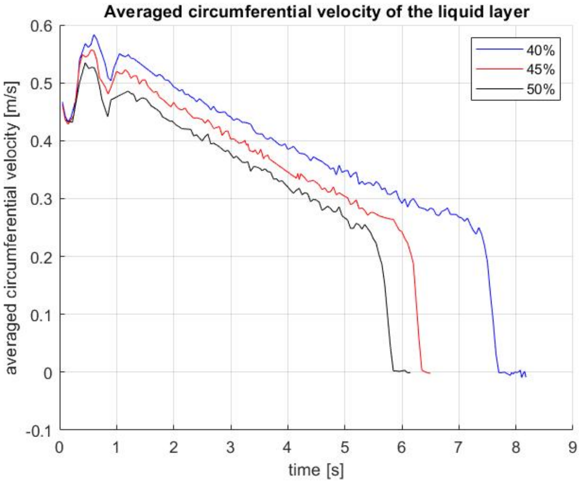

Figure 65: The averaged circumferential velocity of the liquid layer throughout the draining regime

Glycerol-%	40%	45%	50%
Drainage time [s]	8.075	7	6.6
Bubble regime [s]	1.05	1	0.95
Transition regime [s]	0.3	0.4	0.5
Vortex regime [s]	6.25	4.6	4.15
swirl regime [s]	0.475	0.9	1

Table 9: Duration of draining regimes for the Mo-case

4.2.2 Bubble regime

The Morton number influences the bubble characteristics in the bottle, as can be seen in figure 3. From the literature review, relations for the terminal rise velocity of Taylor bubbles in vertical tubes and the terminal velocity of rising bubbles in unhindered liquid environment were found. The emptying process starts with Taylor bubbles being formed in the opening of the bottle, where the shape and the rising velocity of the bubbles are determined due to the geometric restrictions of the connector walls. For the vertical rising velocity, equation 6 can be used which is valid when surface tension is negligible ($Eo > 40$). The rising velocities of the Taylor bubbles calculated by equation 6 are shown in the second column of table 10 labeled as velocity. From the table, it appears that the rising velocity for Taylor bubbles is higher for lower viscosities. Since it is more useful to compare the volumetric flow rates, rather than the rising velocity of the bubbles, the effective area in the bottle opening should be estimated as well. The film thickness δ around a Taylor bubble in the bottle mouth can be estimated with the following relation [90]:

$$\delta = d_h \left(\frac{-1 + \sqrt{1 + 2.44 N_f^{2/3}}}{2.44 N_f^{2/3}} \right) \tag{115}$$

where d_h is the inner diameter of the bottle opening and N_f is the inverse viscosity number. By calculating the film thickness in the bottleneck, the effective area of the air-layer in the bottleneck can be determined. By multiplying the rise velocity of the bubble with the obtained effective area, the air volumetric flow rate can be estimated. By applying volume conservation, the liquid flow rate is also obtained. The liquid volumetric flow rates are depicted in the third column in table 10. It should be noted that the values calculated in table 10 are values for the case when the bottle is initialized with no rotational velocity. However, since the Π-number is kept constant, it can be expected that these values still can give a correct qualitative description on the volumetric flow rates and the bubble behaviour. From table 10, it appears that the differences in volumetric flow rates between the different glycerol weight percentages are barely noticeable. This would indicate that the bubble regime is independent in the range of Morton numbers used in this study. When referring back to the literature review, namely figure 6, it was shown that the range of Morton numbers used in this study are in region 3, which indicates that the bubble regime is indeed independent of viscosity. This was also noticed in the numerical results, where nearly to no difference was obtained in the volumetric flow rate, depicted in figure 63 or the volume over time graph, depicted in figure 62.

Glycerol weight percentage	Velocity [m/s]	Flow rate [m^3/s]
40%	0.0891	7.9346e-06
45%	0.0859	7.6394-06
50%	0.0827	7.3480e-06

Table 10: Velocity and volumetric flow rate for the Morton case based on the theory stated in equation 115.

Also, from figure 66, it can be seen that the initial bubble growth due to the Rayleigh-Taylor instability is independent of the Morton number. Bellman and Pennington [91] studied the effect of viscosity on the growth rate of the Rayleigh-Taylor instability for the initial regime. They concluded that viscosity is negligible for a wave number of $k < 3$ cm^{-1}. The maximum wavelength is identical for all the cases due to the geometrical restrictions. Also, the difference in film thickness between the cases is negligible. From observation on the numerical results shown in figure 66, it is evident that the shape of the interface is similar to one half of the wave length. Therefore, the maximum wavelength for all the cases is approximately equal to twice the inner diameter of the bottle opening (2.15 cm). Thus, it can be concluded that viscosity effects can be neglected for the initial growth rate of the bubbles in the bottle, since $k = \frac{2\pi}{\lambda} = \frac{2\pi}{2.15} = 2.92$ cm^{-1} is smaller than 3 cm^{-1}.

Even though the difference in flow rates and the effective area in the bubble regime are negligible in relation with the Morton number, one parameter changes in the bubble regime. From figure 65, it can be seen that the viscosity influences the overall liquid circumferential velocity. Especially from around 0.5 seconds, the deceleration between the cases starts to show. However, this deceleration has not effected the drainage time yet, and thus the bubble regime remains unaffected by the alteration of the Morton number.

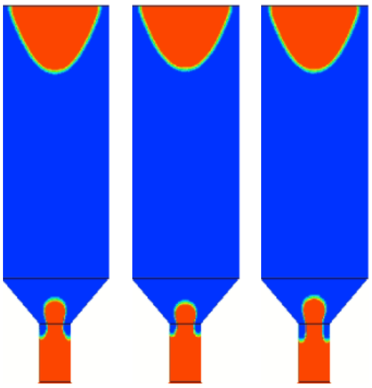

(a) (b) (c)

Figure 66: VOF contour of the bubbling regime at t=0.1 s for a) 40% b) 45% c) 50% glycerol

4.2.3 Transition regime

It was found that the bubble regime was independent in the range of the tested Morton numbers. However, the circumferential velocity started to differ between the three cases and it is believed that this caused dissimilarities between the three cases in the transition regime. The dissimilarities can be seen from table 9. From the table, it can be obtained that an increase in the Morton number results in a small increase of the drainage time in the transition regime.

In the Π-case, an inverse correlation was found between the time of the transition period and the initial angular velocity, which stated that the transition regime lasted longer for a decrease of the angular velocity. From figure 65, it is visible that an increase in Morton number reduces the circumferential velocity. Combining the inverse correlation from the Π-case and the relation between the Morton number and the circumferential velocity, it is expected that this inverse correlation is also applicable on the Morton case. This means that with an increase in viscosity, the transition regime should last longer. From table 9, it can be seen that indeed an increase in viscosity results in an increase of the drainage period of the transition regime. A horizontal and vertical circumferential contour was made to visualize how for the three cases the circumferential velocity behaves in the transition regime. The contours at t=0.05 seconds in the transition regime was made and depicted in figure 67 and 68. It can be seen from the contours that the overall circumferential velocity is higher for the least viscous fluid.

The deceleration due to viscosity can be explained with viscous dissipation. Consider the kinetic energy of the fluid layer

$$E = \frac{1}{2}\int_{V_b} \rho|\mathbf{u}|^2 dV \tag{116}$$

where V_b is the volume of the liquid layer in the top bottle. To obtain the energy dissipation, the time derivative of equation 116 will be taken and through mathematical manipulation, the following energy dissipation equation is obtained:

$$\frac{d}{dt}E = \int_A \mathbf{u}\cdot(\mathbf{n}\cdot\sigma)dA - 2\mu\int_{V_b}|E|^2 dV + \int_{V_b}\rho\mathbf{b}\cdot\mathbf{u}dV \tag{117}$$

where A is the surface, $\sigma = -pI + \tau$, τ is the stress tensor, which contains a pressure and viscosity term, $|E|$ is the strain rate magnitude and $\mathbf{b}$ is the body force. The first term represents the work done by the hydrodynamic force, the second term is the energy dissipated and thus the viscous dissipation rate, the last term is the work done by the body force. From equation 116, it is obtained that by increasing the viscosity of the fluid, more energy will be dissipated. This is done by transforming the motion of the fluid into internal energy of the fluid. In other words, more of the circumferential velocity will be turned into heat with increasing viscosity, resulting in the higher deceleration of the circulation, which is in agreement with figure 65.

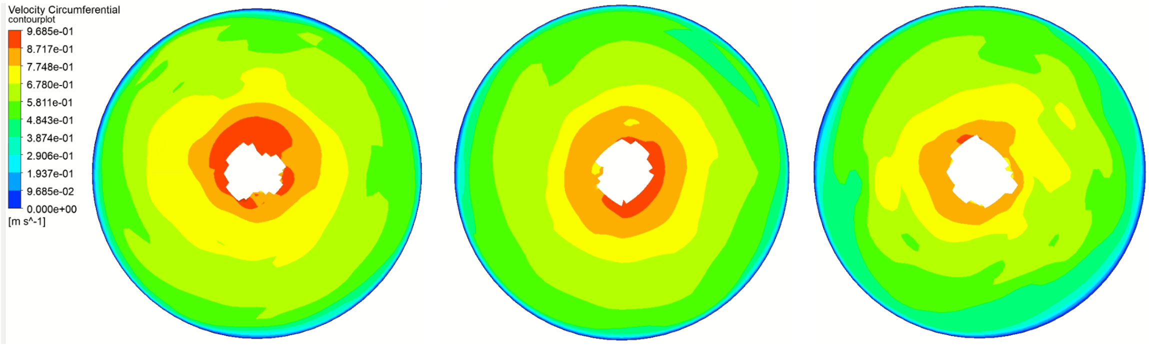

(a) (b) (c)

Figure 67: Horizontal circumferential velocity contour at t=0.05 seconds in the transition regime for a liquid volume fraction $\alpha_l > 0.9$ at z=0.3 m for a) 40% glycerol b) 45% glycerol c) 50% glycerol

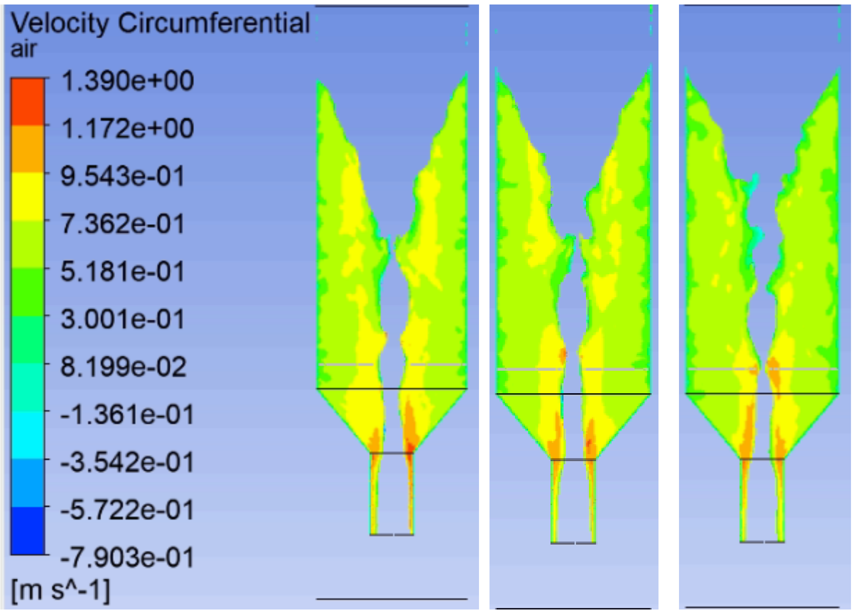

(a) (b) (c)

Figure 68: Vertical cirumferential velocity contour at t=0.05 seconds in the transition regime for a liquid volume fraction $\alpha_l > 0.9$ for at x=0 m a) 40% glycerol b) 45% glycerol c) 50% glycerol

4.2.4 Vortex regime

It seems that even though the decrease in circumferential velocity is already noticed in the transition regime, the effect of viscous dissipation on the drainage time is the largest in the vortex regime. From figure 62, it can be seen that the difference in drainage time between the different Morton case starts to grow wider in the vortex regime. The height-time gradient is also found to be steeper in the vortex regime for increasing viscosity, indicating a higher liquid flow rate for the most viscous fluid. The difference is mainly influenced by the effect of circumferential velocity. The weakened swirl velocity for increasing viscosity was obtained in the results. The evolution of the mean circumferential velocity of the whole liquid layer in the vortex regime is plotted in figure 69 and is calculated as follows:

$$u_{circumferential,mean} = \frac{\sum \alpha_{liquid}(i,j,k) \cdot u_{circumferential}(i,j,k)}{\sum \alpha_{liquid}(i,j,k)} \tag{118}$$

where $\alpha_{liquid}(i,j,k)$ is the volume fraction of the liquid in a specific cell, $u_{circumferential}(i,j,k)$ is the circumferential velocity of the cell. The slopes in the graph of figure 69 is calculated, where the slope is -0.0511, -0.0564 and -0.0604 for the lowest, middle and the highest Morton number respectively. A sharper slope indicates a higher deceleration of the fluid in the bottle, which is a direct result of viscous dissipation. This was also obtained by Zielinski and Villemonte [92], who showed that as the viscosity increased, the circulation of the free surface vortex would decrease faster due to the increased viscous shear.

Combining this with the initial lower angular velocity for increasing viscosity at the start of the vortex regime, it is expected that the centrifugal force acting on the liquid layer should also be weaker for increasing viscosity throughout the vortex regime. From figure 64, it can be seen that this is valid. The radius of the air-core decreases for increasing liquid velocity, which is a direct result of the weaker centrifugal force. The smaller air-core radius corresponds to a thicker liquid film in the bottle opening. Also, due to the weaker centrifugal force, it is easier for the fluid to flow down, increasing the axial downward velocity. Both of these contribute to a higher mass flow rate, resulting the overall drainage time to be the lowest for the most viscous fluid in the vortex regime .

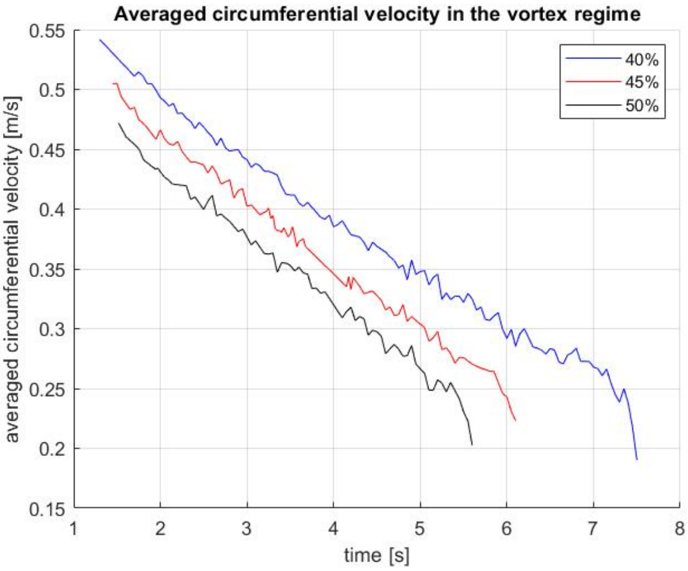

Figure 69: The averaged velocity profiles of the water layer over time in the vortex regime.

4.2.4.1 Π-criterion for the Morton case

As discussed above does the viscosity influence the magnitude of the velocity. This also means that the viscosity influences the exact moment when the air-core vortex is being generated. Increasing the viscosity results in a weaker circumferential velocity and thus a later generation of the free surface vortex. In section 4.1.4.3, it was already found that the generation of the air-core vortex strongly depends on the onset Π-number. To prove that the onset Π-criterion is also applicable for different fluid compositions, the onset Π-number was calculated for the three Morton numbers tested in this section. The calculation of the Π-number is done equivalently as in chapter 4.1.4.3 and the results are shown in figure 70. The red line indicates the onset Π number for the three Morton numbers. The range of onset Π-numbers for the Π-cases is depicted in the grey area. The mean value for the onset Π-number for the Π-case is depicted in the blue striped line, whereas for the Morton case is shown in the black striped line. From figure 70, it can be seen that the onset Π-number for the Morton numbers is in the range of onset Π numbers for the Π-case and the mean value (0.3845 for Π and 0.3319 for Morton) is close for both cases. This indicates that indeed a relation exists between the onset Π-number and when the air-core vortex is being generated. However, the onset number between the different cases still fluctuate too much, therefore no real conclusions can be drawn yet.

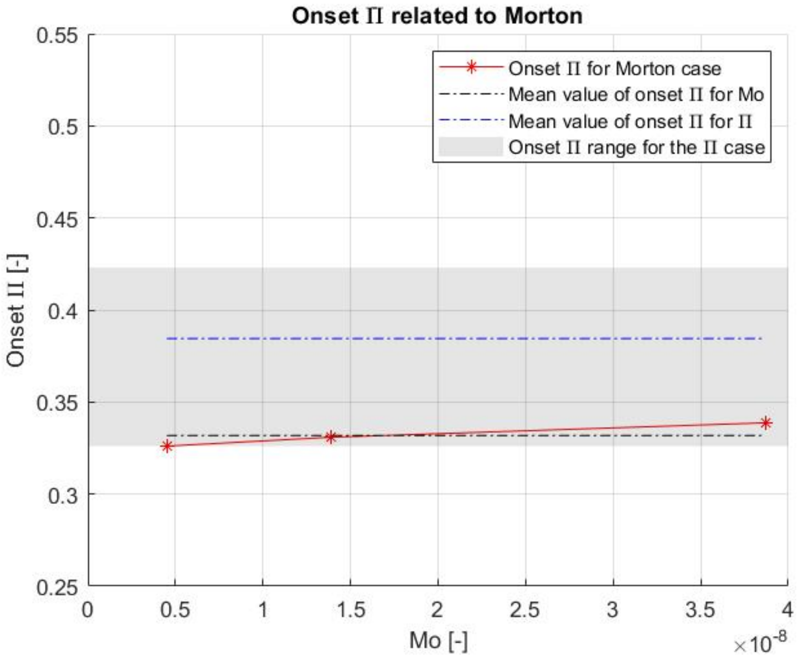

Figure 70: The onset Π-number for the different Morton cases compared to the Π case

4.2.5 Swirl stage

How the increased viscous shear has helped to reduce the drainage time in the vortex regime, the increased viscosity now increases the drainage time in the swirl stage, as can be seen in table 9. In the swirl stage of the Π-case, it was obtained that the swirl stage was strongly dependent on the disappearing hydrostatic force and the still present centrifugal force. When we compare the averaged circumferential velocities of the fluid layer at the beginning of the swirl stage for the different Morton cases, it was found that these velocities were close to each other. The values are depicted in the second column in table 11. The hydrostatic force is dependent on the density of the fluid and the remaining amount of fluid. It was noticed that for the different Morton numbers, the amount of fluid in the top bottle at the beginning of the swirl stage differed between each other. The values of the volume are shown in the last column in table 11. Since the volume is higher for higher viscosity, in normal circumstances the higher hydrostatic force should push the fluid down faster and reduce the drainage time. However, since the amount of volume is rather low, it can be expected that the effect of hydrostatic force can be neglected. Therefore, it seems that the swirl stage is independent of the Π-number and is influenced by the viscous property of the fluid and the Morton number.

Glycerol weight percentage	Mean velocity [m/s]	Initial volume [mL]
40%	0.18	0.55
45%	0.20	10.1
50%	0.19	15.9

Table 11: The mean circumferential velocity profile and the volume in the top bottle at the start of the swirl stage

In the vortex regime, the viscosity and the wall effects decelerate the overall velocity, including the circumferential and the axial velocity. However, in the vortex regime, only the deceleration effect on the circumferential velocity was noticed. The wall effects were negligible due to the dominating hydrostatic effects pushing the fluid down. This is not the case in the swirl regime. The fluid viscosity again decelerates the velocity, however in the swirl regime, the hydrostatic effects are negligible and the difference in circumferential velocity are barely noticeable. This causes the wall effects to start playing a key role in the swirl regime. The influence of the wall shear is shown in figure 71, where the wall shear stress is averaged over the perimeter at the same height. It can be seen that the wall shear stress is higher for an increasing Morton number. This implies that it is harder for the fluid to flow down in the axial direction, causing the longer "swirl" of the fluid and increasing the drainage time for increasing Morton numbers in the swirl regime.

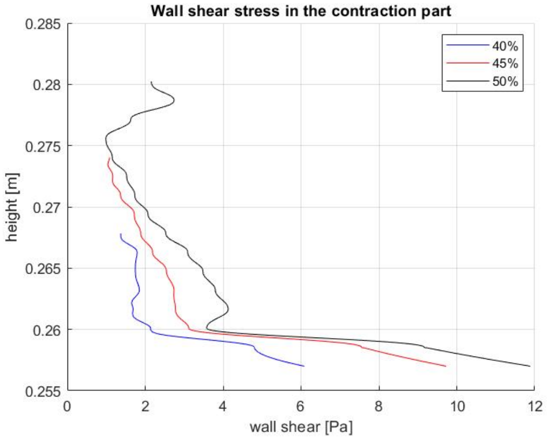

Figure 71: Averaged wall shear stress in the contraction part at the beginning of the swirl stage for the Morton case

4.2.6 Shift of the critical Π-number due to increasing Morton number

The relation that was found in this section between the drainage time and the Morton number stated that an increase in the Morton number resulted in a faster drainage time. This was due to viscous dissipation causing a quicker decay of the circumferential velocity, weakening the centrifugal force. However, by extensively increasing the viscosity, this can lead to a centrifugal force that is weaker than the hydrostatic force throughout the whole drainage. This causes the fluid flow to remain in the bubble regime, resulting in a significant increase in the drainage time. Due to the increased viscosity, more of the centrifugal force will be dissipated, making it a necessity to initialize with a higher rotational velocity, otherwise the air-core vortex will not form. Therefore, it is believed that the critical Π-number shifts depending on the change of the Morton number.

An example is given where a fluid composition of 78% glycerol and 22% water is initialized. The associated Morton number is equal to Mo=4.8969e-07. The bottle is initialized with an angular velocity of 30 rad/s. The volume over time graph is plotted in figure 72 and the result for Mo=4.8969e-07 (78% glycerol) is shown in blue. It was obtained that for this fluid composition, the fluid was too viscous for the air-core to be formed. This resulted that the flow regime would remain in the bubble regime, increasing the drainage time significantly. A comparison is also given in figure 72 shown with the red line, where the bottle is initialized with the same angular velocity of 30 rad/s, however with a Morton number of Mo=4.5145e-09 (40% glycerol). For this Morton number, the air-core vortex was formed, and as can be seen from the graph, the drainage time got significantly reduced. From this, it is believed that the critical Π-number shifts depending on the change in Morton numbers. This conclusion correlated well with the experimental findings of the team of BSc students from the TU Delft (Appendix A), where it was already obtained that the critical angular velocity to form the air-core vortex was not constant for the different glycerol-water compositions.

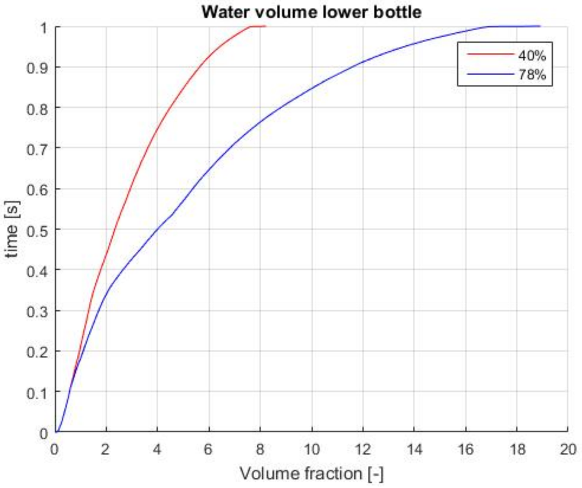

Figure 72: Volume over time for the bottom bottle for 40% glycerine (red line) and 78% glycerine (blue line)

4.3 Case 3: Eötvos

For the last case of this study, the influence of the Eötvos number on the drainage time will be tested. Due to the changing Eötvos number, from figure 3 it can be seen that for an Eötvos number of 30.7977 the bubble shape will change. Since the surface tension term is present in the Morton and Eötvos number, to keep the Morton number constant, viscosity also has to change accordingly. Once more, the base fluid is chosen to be the same as the Morton case, where the 40% glycerol fluid is initialized with an angular velocity of 30 rad/s. However, unlike the previous two cases, no physical fluids were found that matched the requirements that were necessary to alter the Eötvos, while keeping Morton and Pi constant. Thus, for this case no physical fluids are used. To alter the Eötvos number and keep the Morton number constant, the surface tension γ and viscosity μ had to be modified. They are calculated as follows:

$$\begin{aligned} \gamma &= C \cdot \gamma_{40} \\ \mu &= C^{3/4} \cdot \mu_{40} \end{aligned} \tag{119}$$

where γ_{40} and μ_{40} are the surface tension and the viscosity of the 40% glycerol fluid and C is the constant that has a value of 0.5, 1 and 2. This constant is equal to the inverse factor of how much the Eötvos number changes with respect to the base fluid of 40%-glycerol case. A summary of the fluid properties and the dimensionless numbers is given in table 8.

Constant C [-]	0.5	1 (40%-glycerol)	2
Eötvos	123.1907	61.5954	30.7977
Density	1100	1100	1100
Viscosity	0.0022	0.00363	0.0061
Surface tension	0.035	0.07	0.14
Π	0.5619	0.5619	0.5619
Morton	4.515-09	4.515-09	4.515-09

Table 12: Different testcases for the Eo-case

4.3.1 Draining regime

The different parameters over time are shown in figure 73, 74 and 75. The drainage time per regime for every case is depicted in table 13. The graphs and table will be elaborated further in this section.

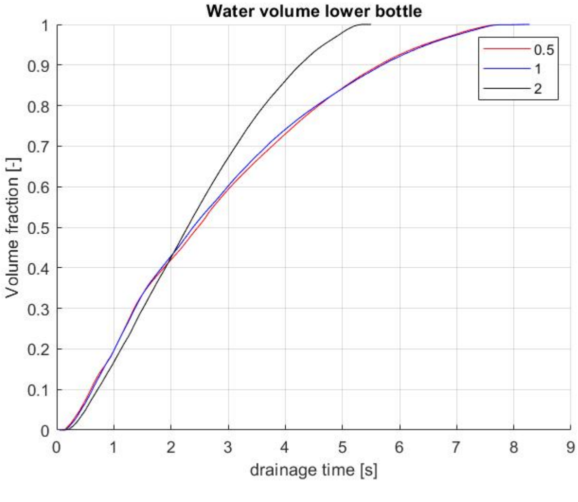

Figure 73: Volume over time for the bottom bottle

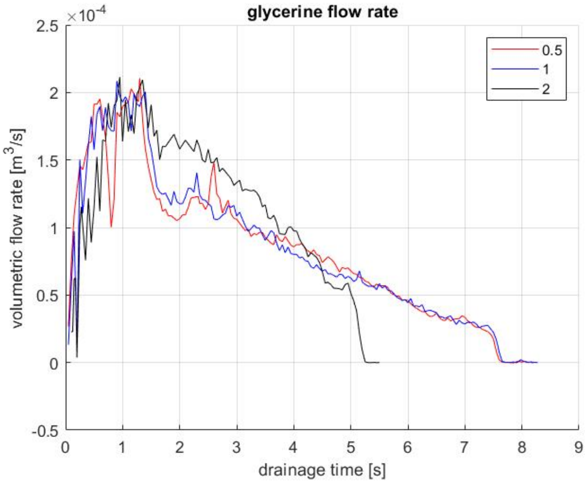

Figure 74: Glycerine flow rate over time out of the bottle opening

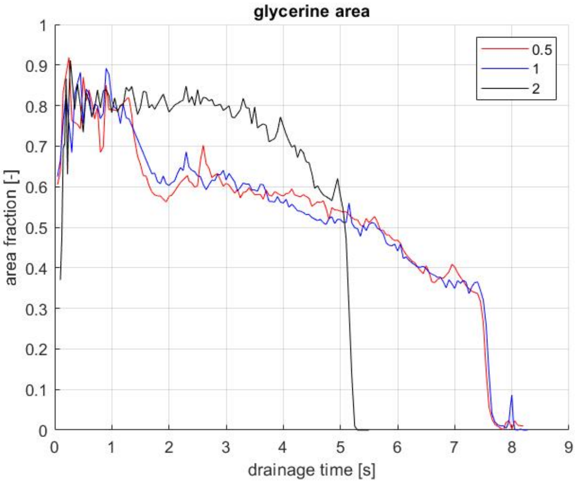

Figure 75: Glycerine area over time in the bottle opening

Constant	0.5	1	2
Drainage time [s]	8.1	8.075	5.25
Bubble regime [s]	1.1	1.05	1.2
Transition regime [s]	0.3	0.3	0.3
Vortex regime [s]	6.3	6.25	3.65
swirl regime [s]	0.4	0.475	0.1

Table 13: Duration of the draining regimes for the Eötvos case

4.3.2 Bubble regime

By increasing the surface tension, physically it means that a higher force is necessary to extend the air-liquid interface. For the special case where the heavier fluid lies on top (Rayleigh-Taylor instability), there is a range of short waves for which the surface tension stabilizes the interface, resulting in an impenetrable interface. At a certain value does the hydrostatic force surpass the surface tension force and mixing between the two layers start to occur. This statement was proven by Kohira [93], who obtained that for an air-water system, fluid flow was only found for a bottle opening diameter bigger than 4mm. This can be explained with the capillary wave length, which relates gravity to surface tension as $\lambda c = \sqrt{\frac{\gamma}{\Delta\rho g}}$. When the wave length of the interface is larger than the capillary wave length, the interface becomes unstable, which causes the start of the formation of bubbles. The capillary wave lengths from the highest to the lowest Eötvos numbers are 1.8 mm, 2.5 mm and 3.6 mm respectively. Since the inner diameter of the bottle opening is 1.075 cm and even though the formation of the interface is only one half of the wavelength, it can still be concluded that for all the cases the interface becomes unstable.

From the first two time steps of 0.05 seconds each, depicted in figure 77, the influence of the different Eötvos numbers on the bubble regime is already noticed. It can be seen that for the lowest Eötvos number, the deformation of the interface is the smallest. This is due to the surface tension providing a restoring force to the interface, which explains the later starting point of the lowest Eötvos number in the graph in figure 73. The rate of deformation can also be expressed with the growth rate of the interface. The growth rate ω can be solved from the dispersion relation for the Kelvin-Helmholtz and the Rayleigh-Taylor instability:

$$\omega(k) = \left(\frac{\rho_1 U_1 + \rho_2 U_2}{\rho_1 + \rho_2}\right)k \pm \frac{k}{\sqrt{\rho_1 + \rho_2}} \cdot \sqrt{-\frac{\rho_1\rho_2(U_2 - U_1)^2}{\rho_1 + \rho_2} + \frac{(\rho_1 - \rho_2)g}{k} + \gamma k} \tag{120}$$

where subscript 1 is for the bottom fluid and subscript 2 stands for the top fluid, k is the wave number. For simplicity, it is assumed that during the beginning stage of the Rayleigh-Taylor instability, no velocity difference between the two layers has yet been noticed, reducing equation 120 to

$$\omega_{RT}(k) = \pm\frac{k}{\sqrt{\rho_1 + \rho_2}} \cdot \sqrt{\frac{(\rho_1 - \rho_2)g}{k} + \gamma k} \tag{121}$$

The instability of the interface is triggered when an unstable mode with a positive growth rate ($\omega_i > 0$) exists, where the subscript i stands for the imaginary value. Thus, to trigger the Rayleigh-Taylor instability, the heavier fluid has to be on top ($\rho_1 - \rho_2 < 0$). Note from equation 121 that for the case when $\rho_1 - \rho_2 < \gamma k$, the growth rate becomes a real value and therefore erases the instability. This satisfies the condition discussed earlier in this subsection, that for high surface tension values, the surface tension fully stabilizes the interface. From equation 121, it can be concluded that an increase of the surface tension results in a decrease of the growth rate for a constant wave number. Since the wavelength is constant due to geometric constraints, it can be expected that the growth rate is the highest for the highest Eötvos value and vice versa. Ergo, for a higher Eötvos number, bubbles will be generated easier. The equations stated above are generally used for the Rayleigh-Taylor instability in stagnant fluid. However, El-Ansary et al.[66] found that the theory is still valid for rotational flow. The only difference between the stagnant and the rotational case is that the values of the growth rate were slightly lower for the rotational case in comparison with the stagnant case.

Not only the initial deformation of the interface is dependent on the surface tension, also the deformation of the bubble can also be found to be in relation with the surface tension. When the bubble is sufficiently distorted, its top is found to be spherical, whereas the bottom is close to being flat. This deformation occurs when the effect of gravity is larger than the surface tension. If the effect of surface tension is large, the bubble is nearly a sphere. The underlying physics is described in the literature review. From the figure designed by Clift [8] in figure 76, it can be seen that for C=1 and C=2, the bubbles will stay in the spherical-cap regime, whereas for C=0.5 the bubble will occur in the wobbling regime. This was also obtained in the numerical results, shown in figure 78 d, e and f.

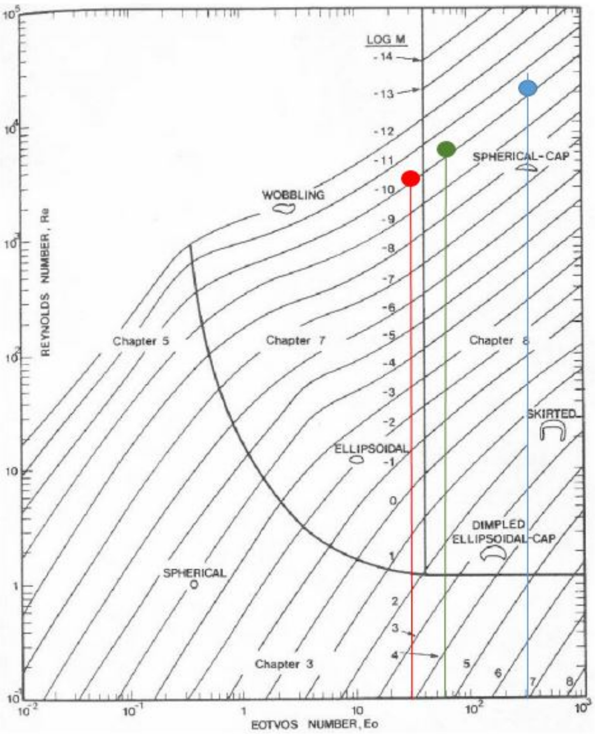

Figure 76: Behaviour of the bubble shape by Clift[8] for different glycerol weight percentages. Blue: C=0.5 Green: C=1 Red: C=2

Surface tension also effects the bubble size. With an increase in surface tension, the bubble size should increase as well. Due to the geometrical restrictions at the bottle opening does the initial bubble size in the opening not differ between the three cases. However, when the bubble enters the conical section, the bubble has no limitations, which results in it expanding radially and axially, where the fluid properties such as the surface tension determine the bubble size. It was expected that due to the increase in surface tension, the bubble size should increase, which would result in a slower frequency in the oscillatory flow pattern. A slower frequency results in a less amplified pulsating behaviour leading to a longer duration of liquid flowing down through the thin liquid layer around the bubble. Therefore, increasing the liquid flow rate. However, from figure 74, it can be seen that the glycerine flow rate for the different cases fluctuate around the same values. Also, the steepness of the slope in the height-time graph in figure 73 barely differ, where after the first generated bubble, the slopes are 0.2098, 0.2266 and 0.2230 for the lowest, intermediate and the highest Eötvos numbers respectively. The gas bubble velocity was calculated where the average bubble velocity for each case was equal to 0.47, 0.51 and 0.5 m/s for the lowest, intermediate and highest Eötvos number. From the literature review in figure 5, it can be observed that only for the Eötvos value of 30.7977 (C=2), the Froude number should be slightly lower compared to the other two tested Eötvos values. However, this difference in velocity is negligible comparing to the total liquid level. Thus, it was found that an increase in Eötvos number did not alter the flow rate or the bubble velocity, even though the bubble shape had changed. Therefore, it is believed that the alteration of the Eötvos number only influenced the flow rate at the initial start of the bubble regime. The effect of surface tension can be assumed to be negligible for the later stages in the bubble regime. Similar findings were found by Sohn [94, 95], who showed that surface tension only affected the initial growth of the Rayleigh-Taylor instability. He also found that an increase in the Eötvos number would decrease the bubble velocity, however the difference in bubble velocity was too small to take into account.

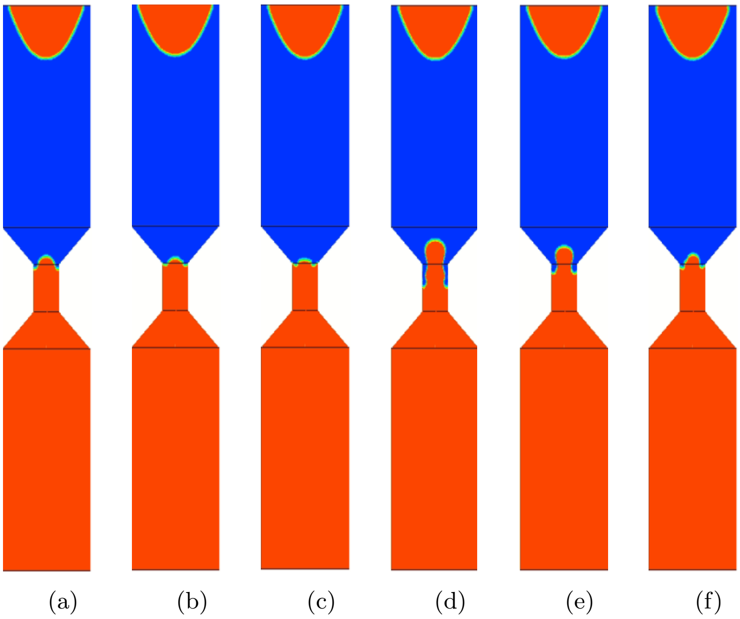

Figure 77: The VOF contour at t=0.05 s for a) C=0.5 b) C=1 c) C=2 and t=0.1 s for d) C=0.5 e) C=1 f) C=2

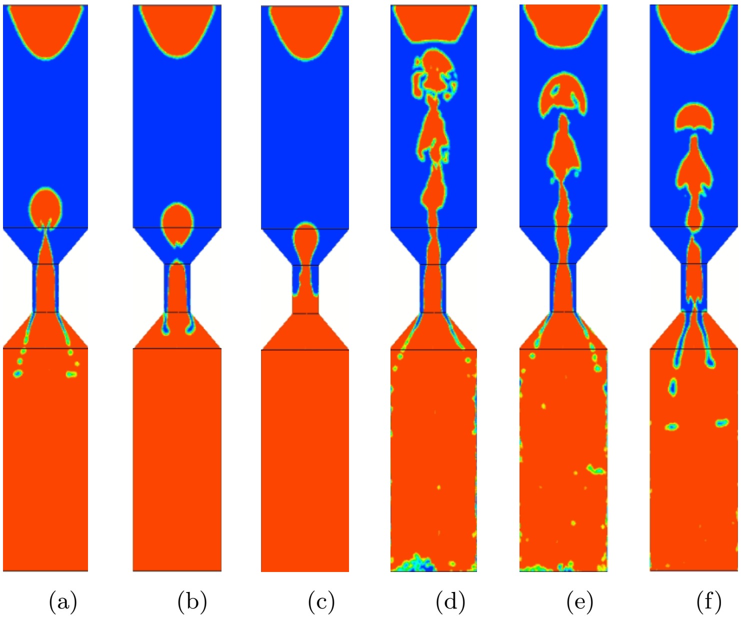

Figure 78: The VOF contour at t=0.2 s for a) C=0.5 b) C=1 c) C=2 and t=0.4 s for d) C=0.5 e) C=1 f) C=2

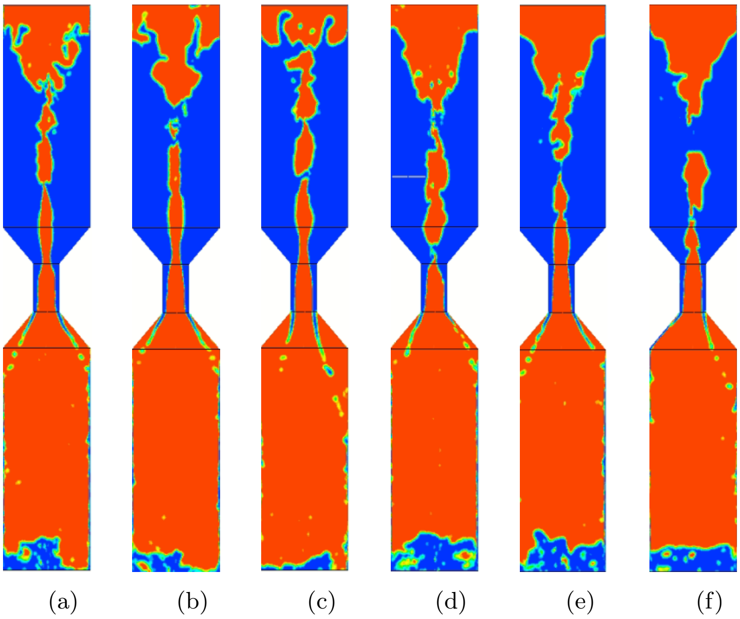

Figure 79: The VOF contour at t=0.6 s for a) C=0.5 b) C=1 c) C=2 and t=0.8 s for d) C=0.5 e) C=1 f) C=2

4.3.3 Transition regime

From table 13, it can be seen that the drainage time for the transition regime is identical for the three different cases. By increasing the Eötvos number, two fluid properties got altered. Both of these parameters will be investigated separately on their effects first.

How the interface behaves, is effected by the surface tension and the Laplace pressure difference, which is defined as:

$$\Delta p_{l\to g} = \gamma\left(\frac{1}{R_1} + \frac{1}{R_2}\right) \tag{122}$$

From the Laplace equation, it can be obtained that for a constant pressure, the radius of the interface will increase for an increase in surface tension. The transition regime is defined as the regime prior to the fully developed vortex regime where the pressure in the air-core layer is equal to the ambient pressure. Therefore, it is expected that due to the same jump of Laplace pressure for every case, the interface would flatten out sooner for the lower Eötvos cases and thus decrease the time of the transition regime.

Since the viscosity increases for a decrease in the Eötvos number, it was expected that the same conclusion from the transition regime in the Morton case was applicable. The conclusion stated that the increased viscosity would decelerate the circumferential velocity faster, which was also obtained from figure 80. This would result in a longer transition for the higher viscous fluid. However, from the Morton case, it was obtained that the effect of viscous dissipation was small in the transition regime compared to the vortex regime. Therefore, it is also believed that the effect of viscous dissipation is small for the Eötvos case. Since the effect of surface tension and viscosity are both small, it is believed that the increase in surface tension and viscosity will cancel each other out or it can be stated that both effects are negligible towards the drainage time. From table 13, it can be seen that the transition regime time is indeed the same for all the three cases.

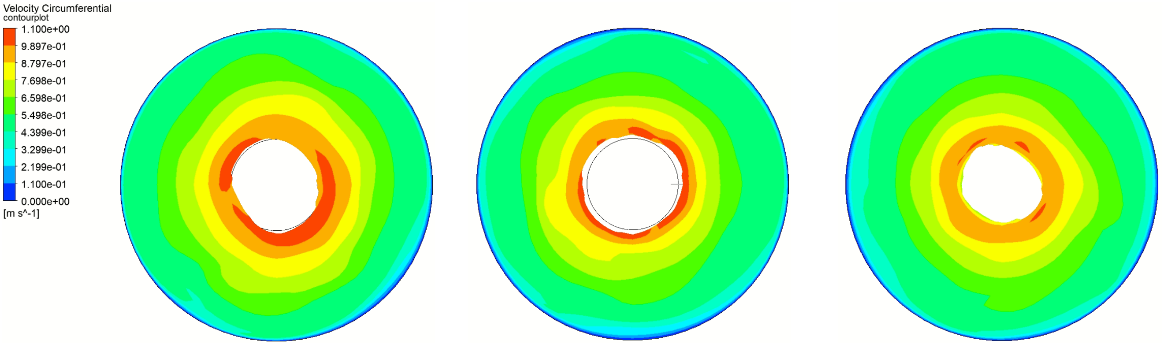

(a) (b) (c)

Figure 80: Circumferential velocity contour at t=0.05 s in the transition regime for a) C=0.5 b) C=1 c) C=2

4.3.4 Vortex regime

From the literature review, it was found that the surface tension had negligible effect on the drainage period of the vortex regime. However, by altering the Eötvos number and keeping the Morton number constant, the surface tension as well as the viscosity got adjusted in the right proportions. From the results, shown in figure 73, it can be seen that the drainage period is significantly shorter for the lowest Eötvos case compared to the other two cases. To clarify this change, again both fluid properties will first be discussed separately.

The alteration of the viscosity was extensively discussed in the Morton case. From that section, it was found that the dissipation rate was higher for the higher viscous fluid, resulting in a quicker decay of the velocities. This implied that the acting centrifugal force was weaker resulting in the effective fluid area in the bottle opening and the downward axial velocity to become higher, which would lead to the increase of the flow rate and thus the shorter drainage time.

The behaviour of the interface due to surface tension can be discussed with the Laplace pressure in equation 122. By assuming that the axial interface is close to flat and thus $\frac{1}{R_1} \to 0$, the Laplace pressure is only a function of the surface tension and the radial curvature. Since the pressure in the air-core in the vortex regime is equal to atmospheric pressure, the pressure difference in each case should be the same provided that the hydrostatic pressure is the same. Thus, by increasing the surface tension, the radius also has to increase due to the Laplace pressure jump. This results in a smaller effective liquid area in the bottle opening and thus a smaller liquid flow rate. However, the decrease in area size was not obtained in the numerical results as can be seen in figure 75. Especially in the early stages of the vortex regime, it can be seen that the effective area is the biggest for the lowest Eötvos case, whereas the difference between the intermediate and the highest Eötvos number is barely noticeable. The averaged circumferential velocity of the liquid layer is shown in figure 81a. From the averaged circumferential velocity, it can be seen that the alteration of the surface tension and the viscosity from the two highest Eötvos number has no significant influence on the circumferential velocity. However, the difference between the lowest Eötvos case and the higher two cases is too big to neglect, where the slope also is steeper for the lowest Eötvos number compared to the other two. It is believed that the steeper deceleration is probably due to the effect of increased viscous dissipation, which was also seen in figure 69 in the Morton case, where the slope is steeper for an increase in viscosity.

It is believed that the surface tension has no effect on the deceleration of the fluid layer and therefore on the centrifugal force. A comparison case was setup, where both fluids had the same viscosity, but different surface tensions. Both fluids contained the same composition as the 45%-glycerol fluid, shown in table 8. However, one fluid had a surface tension of 0.069625 kg/s^2 and the other contained a surface tension of 0.14 kg/s^2. As can be seen from figure 81b, does the circumferential velocity correlate well between the two different values of surface tension. Therefore, it can be assumed that the effect of the surface tension on the centrifugal force in the tested range of Eötvos numbers is most likely negligible. Since the centrifugal force has a significant impact on the downward axial flow velocity and the effective liquid area, it is believed that the overall drainage time is also unaffected by the surface tension. This also agrees with what was found in the literature study, where different studies [96, 97] obtained that the surface tension had negligible effect on the free surface vortex, except for very low circulation rates. Due to the independent behaviour of the circumferential velocity on the change of viscosity for the two higher Eötvos cases, it is assumed that there is a certain threshold or critical Eötvos number / Morton number, where above the critical Eötvos or below the critical Morton number, viscous effects can be neglected. Unfortunately, not enough data was obtained to prove this assumption, where the lowest tested viscosity value for the Morton case was only 0.00363 kg/m s. When the fluid is more viscous than the critical threshold, viscosity effects can not be neglected and the viscous dissipation plays a key role to decelerate the fluid layer and thus decrease the drainage time of the vortex regime.

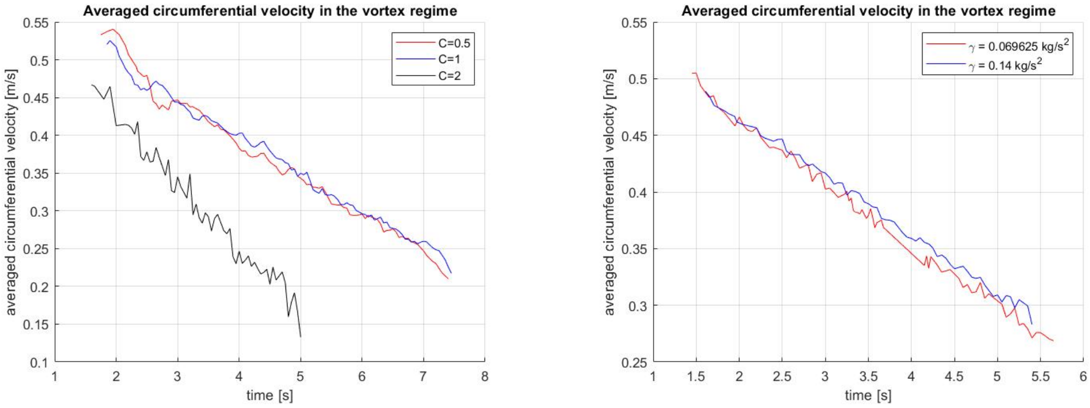

(a) (b)

Figure 81: a) Averaged circumferential velocity for the Eötvos cases b) Comparison of the averaged circumferential velocity for the two test cases with different surface tension but equal viscosity

4.3.4.1 Π-criterion for the Eötvos case

In chapter 4.2.4.1, it was proven that for an increase in viscosity, the relation between the onset Π-number and the generation of the air-core vortex still remained valid. In this section, again the onset Π-number is tested to investigate whether the range of critical Π-numbers still remain the same for different Eötvos numbers.

In figure 82, both onset Π-ranges for the Π (grey) and Morton (pink) numbers are marked. As can be observed, does the onset Π numbers for the Eötvos case remain in the coloured areas. Also, the mean value for the Eötvos case (0.3590) is inbetween the two other mean values. It can be argued that the onset Π-number deviates between the three cases. However, the range where the values deviate correlate quite strong and also the mean values have the same approximate values. Therefore, it is concluded that the moment when the air-core is generated can be predicted through the local Π-number.

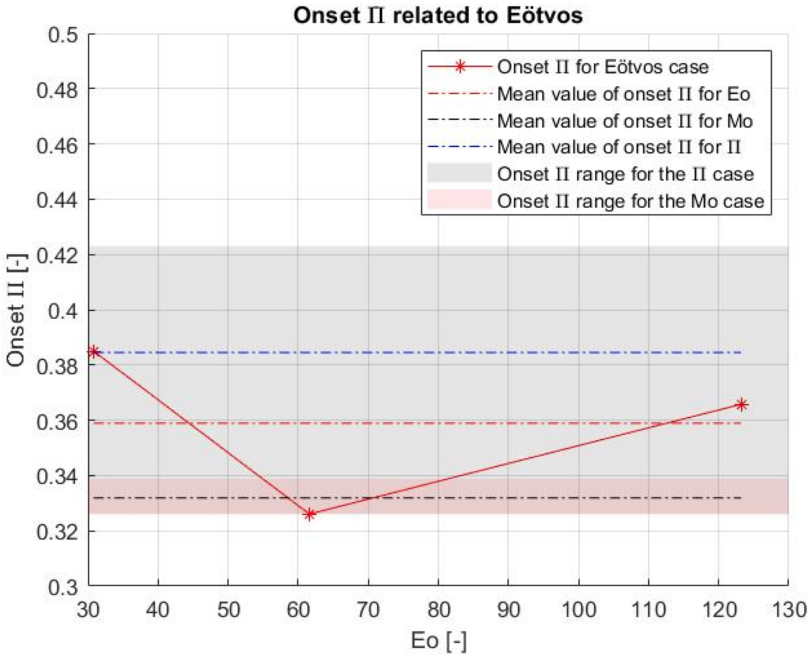

Figure 82: The onset Π-number for the different Eötvos cases

4.3.5 Swirl stage

It was concluded that the difference in drainage time between the three cases in the vortex regime was due to the change in viscosity and the difference in surface tension was negligible. From the Morton case, where solely the viscosity was altered, it was obtained that the drainage time in the swirl stage would increase with an increase in viscosity. When looking at table 13, it can be observed that this is not valid. For the two higher Eötvos cases, it can be seen that for an increase in viscosity, this results in an increase in the duration of the swirl regime. However, for the lowest Eötvos case, it was observed that no swirling was found in the bottle.

Once more, the averaged wall shear stress for the three cases is displayed (figure 83). It can be seen that the wall shear stress is lower for increasing Eötvos numbers, which should result in the fastest downwards flow rate. This is valid for the two higher Eötvos numbers, where the magnitude of the circumferential velocity is still substantial. However, from figure 81a, it can be seen that the circumferential velocity is significantly lower for the lowest Eötvos case, compared to the higher two cases. It was found that for the lowest Eötvos case (C=2), viscous dissipation had already decelerated the fluid flow sufficiently, resulting in a negligible circumferential velocity. This caused the fluid to directly fall down into the bottom bottle, instead of swirling in the bottle.

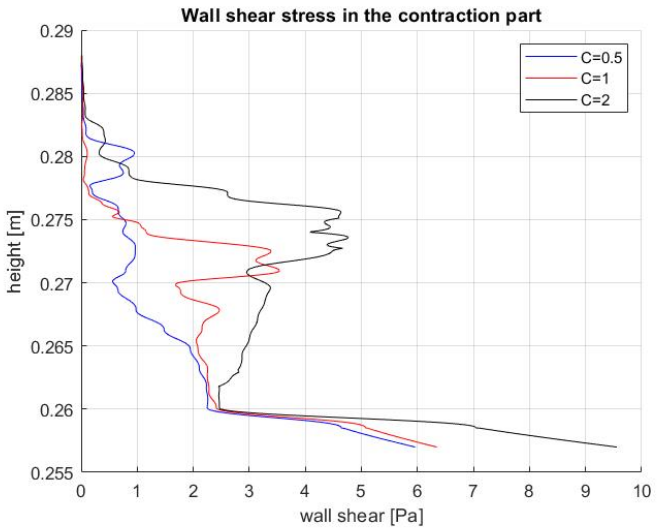

Figure 83: Averaged wall shear stress in the contraction part at the initial stage of the swirl regime for the Eötvos case.

5 Conclusion

The aim of this numerical study was to minimize the non-dimensional drainage time through alteration of three dimensionless parameters, namely the Π, Morton and Eötvos number. The influence of the Π-number was investigated by changing the initial circumferential velocity. The Morton number got tested by increasing the viscosity. The effect of the Eötvos number was analyzed by changing the surface tension and altering the viscosity accordingly to keep the Morton number constant.

For the Π-case, it was crucial that the force balance of the free-surface vortex was studied. The force balance was proven to be correct, where the vortex was balanced between the centrifugal force and hydrostatic force. A higher initialized angular velocity resulted in an earlier generated free-surface vortex with a higher liquid level. It was obtained that at a certain value of Π, the drainage time was minimal. The critical Π-number was found to be $\Pi = 0.1989$ (17 rad/s). A further increase beyond the critical Π-number resulted in a longer drainage time, due to the stronger acting centrifugal force decreasing the effective liquid area and the axial downward flow velocity. From analytical result, it was obtained that the drainage time in relation to Π grows to the power 3 for the laminar regime, whereas for the turbulent regime Π grows to the power 1.5. Comparing this with the numerical results, it was found that the flow regime in the bottle connector turned turbulent for $\Pi = 0.5397$ (28 rad/s). The numerical results correlated well with both the laminar and turbulent relation between Π and the drainage time. Below the critical value, it was found that the air-core vortex could not be maintained during drainage, causing the flow regime to remain in the bubble regime. This resulted in a significant increase in drainage time. In the bubble regime, it was obtained that an increase in angular velocity resulted in an increase in flow rate. However, this difference was relatively small compared to the vortex regime.

For the Morton case, the drainage time got heavily influenced by the viscosity. It was found that an increase in viscosity resulted in a significant decrease in the overall drainage time, where the highest tested Morton number in this study had the lowest drainage time. Viscous dissipation played a key role in the reduction of the drainage time. Due to viscous dissipation, the liquid layer would decelerate, weakening the centrifugal force. This resulted in a bigger effective liquid area in the bottle opening and a higher downward axial velocity, causing the higher liquid flow rate. It was found that the bubble regime was independent in the range of the tested Morton numbers. The effects of viscous dissipation started to get noticed in the transition regime, resulting in a longer transition time between the bubble and vortex regime. The difference in liquid flow rate and drainage time was best noticed when entering the vortex regime. The initial circumferential velocity was lower entering the vortex regime for increasing Morton numbers due to the small effects of viscous dissipation in the transition regime. Moreover, the fluid layer decelerated faster in the vortex regime, resulting in the big difference in drainage time. However, by excessive increasing the Morton number, the effect of viscous dissipation is too strong, preventing the vortex from forming. This causes the drainage regime to remain in the bubble regime, increasing the drainage time significantly. Therefore, to minimize the drainage time, increasing the Morton number is also a viable solution, however the Π-number should always be higher than the critical Π-number for the air-core to be formed.

For the last case, the influence of the Eötvos number got investigated. To vary the Eötvos number and keep the other two parameters constant, both the viscosity and surface tension had to be altered accordingly. From the numerical results, it was obtained that increasing the Eötvos number two times compared to the base fluid (40%-glycerine) had negligible effect on the drainage time. On the contrary, by decreasing the Eötvos with a factor of two, a significant effect on the reduction of the drainage time was obtained. It was found that the bubble regime was independent on the Eötvos number. Only the initial deformation due to the Rayleigh-Taylor instability was found to differ between the Eötvos cases. It was obtained that the surface tension in the tested range of Eötvos number had negligible effect on the air-core vortex and the drainage time. Only viscous dissipation due to the change in viscosity caused the differences in drainage time. It was observed that for the vortex regime the reduction of the Eötvos number was noticed between the lowest and intermediate Eötvos number. However, the difference between the highest and intermediate Eötvos number was negligible. It is believed that a certain critical Eötvos number/ Morton number exists, where the above the critical Eötvos number or below the critical

Morton number, viscous effects can be neglected. When these effects are neglected, it is believed that the drainage time would remain relatively the same. To reduce the drainage time, a decrease in Eötvos number should be realized.

Also, the onset Π-theory was investigated, which stated that the ratio between the centrifugal and hydrostatic force should remain relatively the same when the air-core vortex is generated. It was found that the range where the onset Π-numbers deviated in, correlated well between the different cases, where the maximum range was between $\Pi_{onset} = 0.3261$ and $\Pi_{onset} = 0.4230$. The mean values were 0.3845, 0.3319 and 0.3590 for Π, Morton and Eötvos, respectively. Even though the critical values and the mean values did not align perfectly between the cases, the differences were relatively small. Therefore, it is believed that a certain onset value exists when the air-core is generated.

Concluding this study, it is obtained that the angular velocity should be equal to the critical Π-number and the viscosity should be increased to minimize the drainage time. However, a maximum limit exists on the increase of the viscosity, due to viscous dissipation cancelling the formation of the air-core vortex. Therefore, it is important that for the minimization of the drainage time, the Π-number is always higher than the critical Π-number. Also, it was obtained that surface tension has negligible effect on the drainage time.

6 Recommendations

A big limitation on this study was the available duration to numerically study the air-core vortex in the PET bottle. During the mesh independency study, it was already found that mesh independency was not fully reached for the selected mesh in this study. The reason behind this was that the research goals would not be successfully achieved with the available computational time. In order to prove that the numerical results provided in this study were accurate enough, one should design a denser mesh. As such, more accurate results that satisfies mesh independency can be obtained.

For the Π-number, more numerical calculations should be performed around the critical Π-number and the transition regime between the laminar and turbulent flow regimes. For now, it is obtained that the critical Π-number is 0.2753 and the transition regime happens around $\Pi = 0.6195$. However, it is known that the critical Π-number should be lower than 0.2753 and therefore in order to find the critical angular velocity, one should perform calculations below $\Pi = 0.2753$.

For the Morton case, it is known that by excessive increasing the Morton number, the air-core will not be formed and therefore the drainage time will be increased significantly. Therefore, a maximum Morton number exists for every Π-number, where due to the viscous property of the fluid, the centrifugal force is not strong enough to push the liquid to the side. To minimize the drainage time, the Morton number should be close to the critical Morton number, where for a Morton number higher than the critical Morton number, the fluid flow will remain in the bubble regime. For a Morton number lower than the critical number, the air-core vortex will be formed. Thus, additional numerical simulations should be performed to find this critical Morton number.

Also, a strong correlation was found between the onset Π-number and when the air-core vortex was formed. It is believed from this study that a certain onset value should exist. However, this value was not found and more research should be conducted to find this onset value. It is believed that when this onset value is found and the decay of the circumferential is known, the exact moment when the air-core will be generated can be predicted.

A Appendix I: BSc findings

In this section, a short summary will be given on the research projects conducted by the team of BSc students in the P&E department of the Delft University of Technology under supervision of Dr.ir. W.-P. Breugem, where they experimentally investigated the free-surface vortex.

To test the the free-surface vortex, they designed a closed system with an emptying and a receiving PET bottle that are connected with a ball valve. A visualization of their experimental setup is depicted in figure 26. The bottles are 1L Sourcy bottles where the dimensions are the same as the numerical model. The dimensions can be found in figure 27. To initialize the fluid with a certain initial angular velocity, both bottles are placed in a setup which is actuated by a motor. For their conducted tests, they rotated the bottle with rotational velocities between 3.75 and 40.8 radian per second. Besides the initial angular velocity, viscosity is their other parameter that got studied. The influence of viscosity was studied by testing water and four different water-glycerol mixtures: 19%, 35%, 63% and 83% glycerol weight percentage. Fourteen different angular velocities were tested on water. Three tests were conducted per angular velocity to asses experimental uncertainty. From the data obtained from the water tests, four different angular velocities were determined to test on the water-glycerol mixtures.

The experimental results for the case where water was used as the tested fluid are depicted in figure 84. They obtained from figure 84 that a slight increase in volumetric flow rate was obtained at the start of the drainage for increasing initial angular velocity. However, at the end of the drainage time, they observed a large decrease in the volumetric flow rate for these higher initial angular velocity. This was caused by water that kept circulating in the contraction part of the bottle. Therefore, it was concluded that the highest initial angular velocities did not minimize the outflow time. When they tested the lower initial angular velocities, a more linear relation was perceived in the graph in figure 84 (tests 4 to 7). A relation was found where a decrease in the angular velocity resulted in a decrease of the drainage time, where the minimal drainage time was obtained for test 4-5. At a certain decrease of the initial angular velocity (test 8 to 10), where the initial angular velocity was lower than the critical angular velocity, a transition regime was noticed. For the initial part of the drainage, first a bubble regime was noticed that turns into a vortex regime. However, the air-core will collapse again due to the too weak centrifugal force, transforming the flow regime back into the bubble regime, which resulted in a longer drainage time. When the angular velocity was reduced even more, only a bubble regime occurred, which applies to tests 11 and 12. In this range of angular velocity did the initial angular velocity have no large influence on the drainage time.

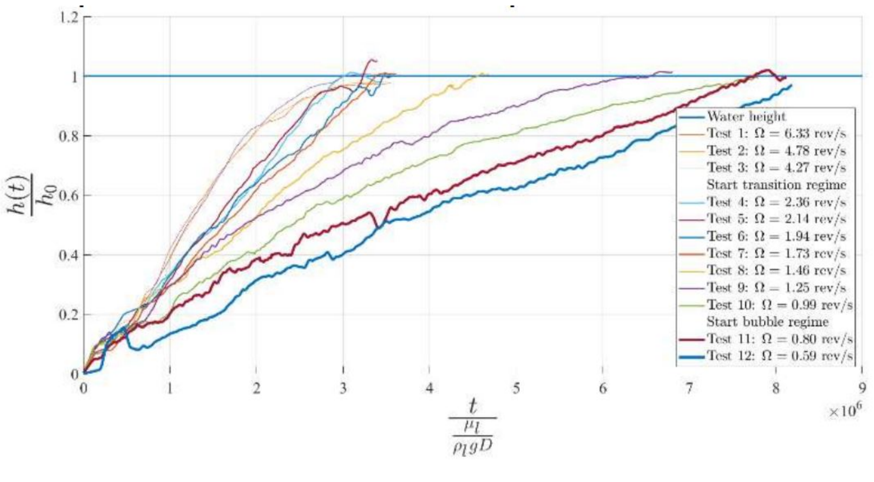

Figure 84: The experimental results obtained by the BSc group where the measured dimensionless height is plotted against the dimensionless time.

The BSc group also compared the drainage time between the different glycerol weight percentages.

They obtained that the two lowest viscosities (100% water and 19% glycerol) had the lowest drainage times. However, to obtain the same drainage time between the 100% water and 19% glycerol, a higher initial angular velocity for the 19% glycerol was necessary. The dimensionless outflow time $\frac{t_{drainage}}{\sqrt{\frac{h_0}{g}}}$ is significantly increased at higher viscosities. They also obtained that the drainage time was highly dependent on the surface tension.

Summarizing their results, it is concluded that the angular velocity has a substantial effect on the outflow time. Most importantly because the rotation initiates a vortex which drastically reduces the outflow time. The higher the angular velocity, the stronger the vortex. However, they found that the optimal initial angular velocity is not the highest reachable velocity, but lies somewhere between a fast vortex and the bubble regime. The optimal initial angular velocity is one that creates a vortex that is just strong enough to provide constant inflow of air. The viscosity of the fluid has a significant influence on the extent to which a vortex be formed and maintained and therefore also on the outflow time. It is found that higher viscosities have a lower outflow time for the same initial angular velocity up to the point where it is not possible to create a vortex and a bubble regime is always present.

B Summary and additional CFD settings

Solver	
Type	Pressure-based
Time	Transient
Pressure-velocity coupling	
Scheme	PISO
Spatial discretization	
Gradient	Least squares cell based
Pressure	PRESTO!
Momentum	Central differencing
Volume fraction	Geo-Reconstruct
Level-Set function	Second Order Upwind
Time discretization	
Transient formulation	First Order Implicit

Table 14: Solution Methods

Viscous Model	Laminar
Multiphase modelling	
Multiphase model	Volume of Fluid
Interface tracking	Coupled Level-Set + Volume of Fluid
Volume fraction formulation	Explicit
Volume fraction cutoff	1e-06
Global Courant number	<0.25
Primary phase	Air
Secondary phase	Water

Table 15: Models

Gravitational acceleration [m/s^2]	-9.81 (z-direction)
Operating density [kg/m^3]	0
Operating pressure [Pa]	101,325

Table 16: Operating conditions

	Water	Air
Density [kg/m^3]	998.2	1.225
Dynamic viscosity [kg/ms]	1.003e-03	1.7894e-05
Surface tension [kg/s^2]	7.3e-02	

Table 17: Water and Air properties at 20°C

	40% Glycerol & 60% Water	Air
Density [kg/m^3]	1100	1.225
Dynamic viscosity [kg/ms]	3.63e-03	1.7894e-05
Surface tension [kg/s^2]	7e-02	

Table 18: Glycerol/water and air properties at 20°C

All these CFD settings were applied and the numerical solutions in this study were calculated in Fluent 19.2

Some notes on the CFD settings that were found in this study:

- The operating density had to be set to zero, otherwise no hydrostatic pressure was achieved in the numerical solutions.
- The gas phase had to be set as the primary phase and the liquid phase as the secondary phase.
- By interpolating the solution from a coarse grid to a fine grid, the pressure values in the cell would sometimes explode. This happened only for the case when the ratio between the two mesh densities were too big. To avoid this problem, the numerical solution would first get interpolated with a mesh, where the density was chosen between the coarse mesh and finer meshes. When the numerical calculation stabilized, again the solution would get interpolated to the finer mesh density.
- All the turbulence models would explode when solving in 2D axisymmetric, where the turbulent viscosity ratio would be above 1e5. This was also the case when initializing with a very low turbulent viscosity ratio.
- For every case, the interface should undergo deformation due to the heavier fluid being on top. However, for very low angular velocities, it was obtained that this deformation did not occur automatically. Therefore, the Rayleigh-Taylor instability had to be initialized at the interface to start the drainage process for very low initial angular velocities. Instead of a flat interface, the interface was initialized with a certain curvature that would look similar to the initial Rayleigh-Taylor instability.

C Appendix II: Mesh independence study

Before valid results can be produced, a mesh independence study has to be conducted first to determine the "correct" mesh size to achieve numerically accurate results. Generally, a denser mesh is desired to capture all the important flow fluctuations. However, a very fine mesh increases the computational resources and time significantly. By increasing the mesh density, the accuracy of the numerical result grows like an asymptote, whereas beyond a certain level of fineness, increase of computational resources will result in negligible improvement of accuracy. At this point, increasing the mesh density is ineffective and it can be taken that mesh independency has been reached.

To test the different meshes, a test case had to be selected. Since the bachelor students performed several tests with water and measured the drainage time for different rotational velocities, the logical following step would be to mimic the same fluid properties and rotational velocities for the test case. However, it was quickly found that using water as the fluid medium was not achievable. The computing time to simulate 1 second on the finest mesh (mesh 4 in table 2) for water was 30 days on 24 cores. Also, mesh independency was not found while comparing the finest mesh with the second finest mesh, which meant that further refinements were necessary. This meant that it would take months to fully simulate the drainage process of the bottle for this specific test case. Considering the time available for this study, this did not seem efficient, thus a different approach was needed.

The spatial resolution of the mesh, thus the total number of grid cells scale with $\mathcal{O}(Re^{9/4})$. [86] Also, the integration time-step to resolve the smallest timescales scales with $\sim Re^{1/2}$. Thus, the computational effort to fully resolve all the scales in the computational domain, scales as follows:

$$\mathcal{O}(Re^{9/4} \cdot Re^{1/2}) = \mathcal{O}(Re^{11/4}) \tag{123}$$

As can be seen from equation 123, the computational effort grows with around the third power of Reynolds. Since a minimum rotational velocity is necessary to generate the free-surface vortex, lowering the velocity to reduce the Reynolds was not feasible. The geometry of the bottle was also kept constant, thus altering the fluid properties was the only alternative solution. By doubling the viscosity of the fluid, a power to the third decrease of the computational effort is expected.

Using aqueous glycerol solutions to invest the variety of aspects of two phase flow concerning viscosity has been done by numerous studies.[98, 99] Glycerol in combination with water provides a wide variety of viscosity values. All the fluid properties of the glycerol/water solutions used in this study, are based on the works of Takamura et al.[89] They obtained experimental values for the fluid properties, which included density, surface tension (against air) and viscosity for different temperatures.

To study the grid sensitivity, a combination of 40% glycerol and 60% water was used. The fluid properties are depicted in table 18. The bottle was initiated with a rotational speed of 50 radian per second and again stopped, when solid body rotation had been achieved, which in this case was equal to 74 seconds. The evolution of the circumferential velocity during spin-up is depicted in figure 85. It was noticed that the difference in computational time to spin the fluid up between the water case and the glycerol/water case was significantly large. The computational spin-up time was 2 weeks to simulate 115 seconds for the water case, whereas only 36 hours was needed to simulate the 74 seconds for the glycerol/water case. Both the spin-up cases were using the same identical mesh. When looking back at figure 85, a bump in the velocity profile was noticed at a radius of 0.005m. At first it was thought that the transition in the mesh between the inner cuboid and the radial profile caused this bump. However, altering the dimensions of the inner cuboid did not change or remove the bump. Since it was not expected that the bump would have significant influence on the flow characteristics and the drainage time, the search on the cause of the bump was halted and no explanation was found.

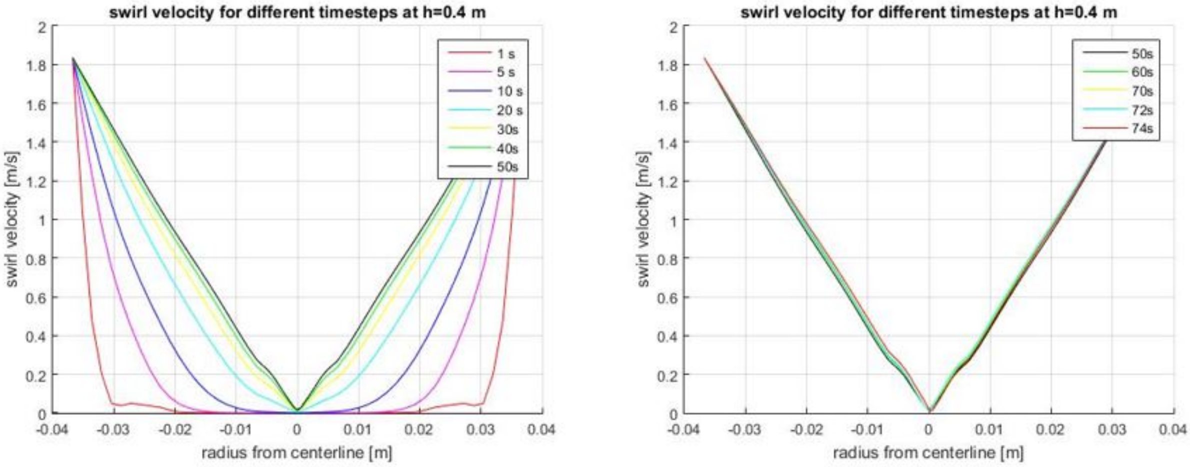

Figure 85: Circumferential velocity profile of the spin-up process for a fluid combination of 40%-glycerol and 60%-water with an initial rotational velocity of 50 radian per second.

To efficiently use the computing resources, the spin-up process was done on the coarse mesh of 400.000 cells. When solid body rotation had been reached, the solution got interpolated to the finer meshes, where for all the cases, the simulation would spin for 1 more second in numerical time to smoothen the peaks out. The interpolated circumferential profile for the different meshes are depicted in figure 86. It can be observed that the velocity profiles look identical between the four meshes after interpolation. The air volume fraction contour for the 4 meshes are shown in figure 87. Notice that the parabolic surface is realized during the spin-up process.

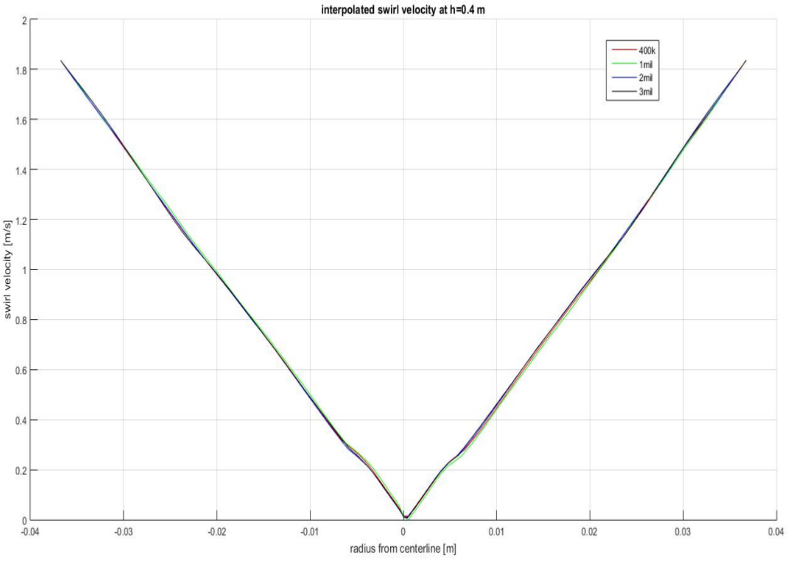

Figure 86: Circumferential velocity profile for the 4 meshes

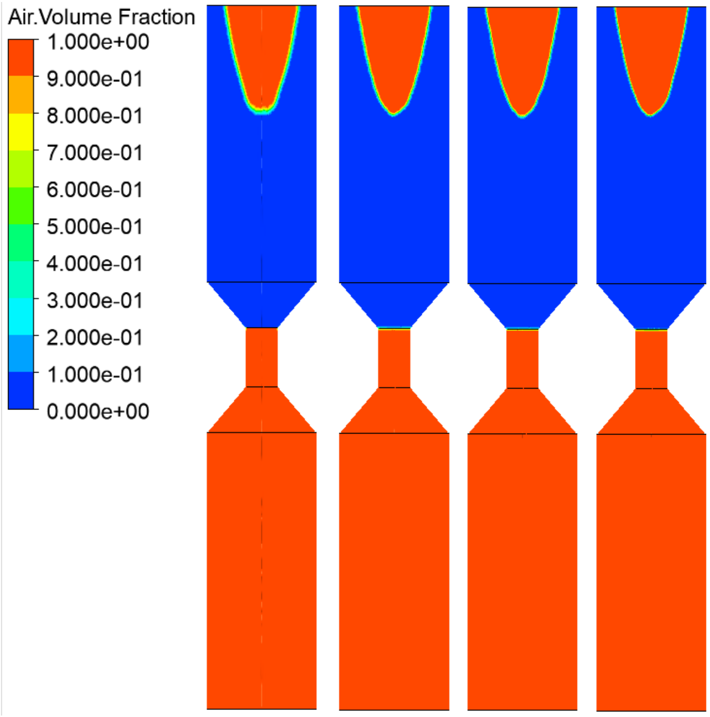

(a) (b) (c) (d)

Figure 87: Air volume fraction for meshes a) 400.000 b) 1 million c) 2 million d) 3 million nodes

To validate the "correct" size to achieve numerically accurate results, various parameters should be compared. These parameters should be based on the important flow characteristics and the goal of the research. The goal of this research is to minimize the drainage time, thus the most important parameter for mesh independency is to ensure that the drainage time is calculated as accurate as possible. The drainage time is dependent on the volumetric flow rate out of the top bottle and the effective area in the bottle opening. Therefore, the volumetric flow rates and the effective area are compared as well. In addition, these two parameters can give a good insight in the different flow regimes. Next to the transient behaviour, also the velocity profiles at different moments during the drainage period will be compared. For example, the Π-number is dependent on the centrifugal force, which on its own is related to the circumferential velocity. Therefore, obtaining accurate results for the velocity profile is also a necessity.

C.1 Drainage time

In table 19, the drainage time for the different mesh densities are shown. Also, the computational time to calculate the different meshes are depicted in table 19. The computational time is twice as large for the 2 million mesh compared to the 1 million mesh, whereas the drainage time between these two meshes barely differed. The calculation for the 3 million mesh was not finished, which is why the result is replaced with "*simulation not completed*". The reason why the calculation was not finished, is that the computational time to fully simulate 2.5 seconds was already 24 days. This meant that it would at least take twice as long to fully finish the whole calculation. Due to the available time for this master thesis, it was decided that the computational time for the 3mil was too long to achieve the research goals in the available time that was given. Thus the calculation was stopped and no result for the 3mil drainage time was obtained.

Mesh	Drainage time	Computation time
400k	9.25 s	8 days
1mil	9.15 s	11 days
2mil	9.175 s	24 days
3mil	*simulation not completed*	*simulation not completed*

Table 19: Drainage and computation times for the different meshes

C.2 Flow rate

The glycerine flow rate out of the top bottle into the bottom bottle was compared between the meshes. The glycerine flow rate was calculated as follows:

$$\dot{V}_{glycerine} = \frac{\sum \alpha(i,j,k)u(i,j,k)}{n_{cell}} A_{liquid} \tag{124}$$

where α is the liquid volume fraction, u the velocity, n_{cell} the amount of cells in the liquid regime, A_{liquid} the liquid area in the bottle opening and i, j, k are the indices of the cell. A clear distinction between the four flow regimes can be seen in figure 88. The bubble regime is located in the time period between 0 and 0.55 seconds. The transition regime is between 0.55 and 0.75 seconds. The vortex regime is between 0.75 and 8.4 seconds. The swirl stage is after 8.4 seconds. From figure 88, it can be observed that the flow rate differed quite substantially, especially at the beginning stage of the vortex regime. However, the exact transition moment between the 4 stages got predicted quite accurately, where the maximum difference between the meshes was 0.2 seconds.

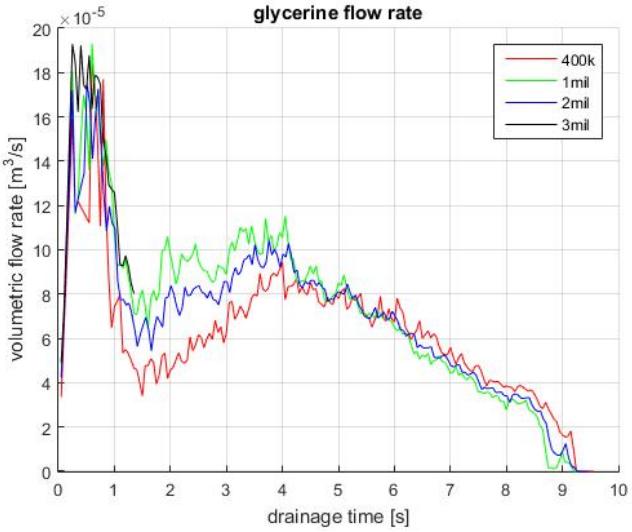

Figure 88: Glycerine flow rate

C.3 Area fraction

Several parameters are dependent on the calculation of the effective area fraction of the liquid layer, such as the flow rate as well as the drainage time. Therefore, an accurate representation of the liquid area in the bottle opening is desired. An example of the glycerol-water area is depicted in figure 89. How the area fraction develops through the drainage period is shown in figure 90. When looking at the vertical axis of figure 90, the y-label is depicted as area fraction. This area fraction is defined as the liquid area divided by the total area in the connector of the bottle. Again, the transition moment between the different flow regimes correlate well between the meshes. Only the coarsest mesh deviates from the 1mil and 2mil mesh.

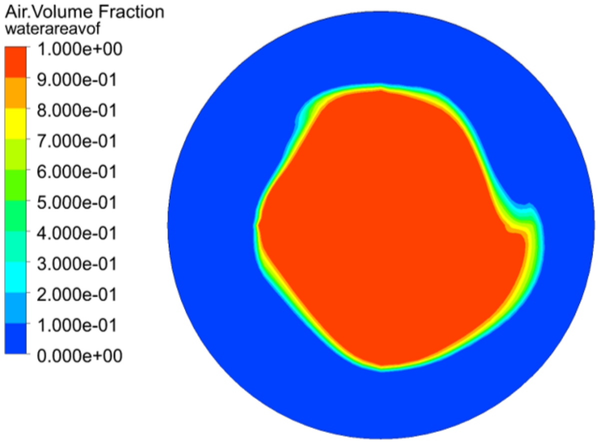

Figure 89: VOF contour of the glycerine area in the connector

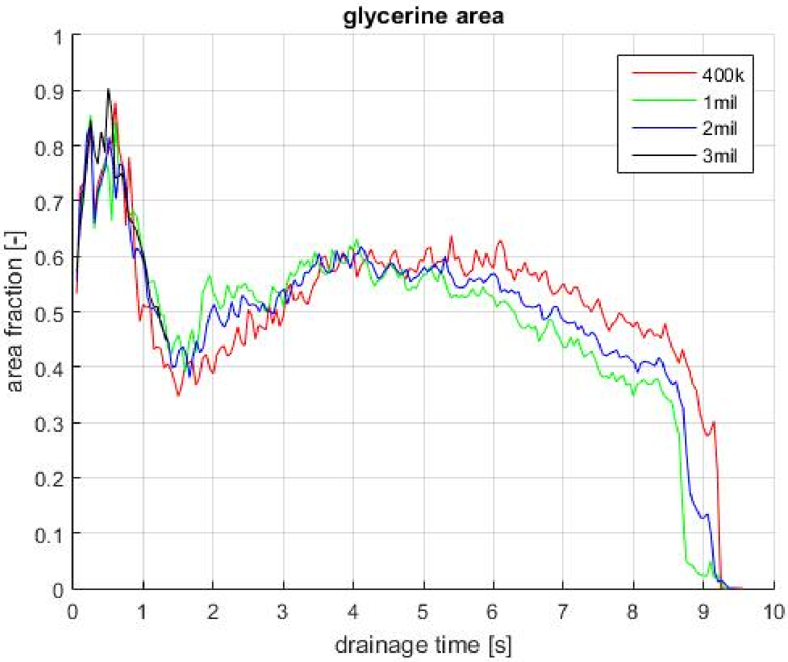

Figure 90: Liquid area fraction in the bottle opening

C.4 t = 0.05 s

Instabilities generated at the beginning of the simulations can dominate the whole flow characteristics throughout the drainage process. Therefore, to avoid the risk of non-physical instabilities due to mesh inaccuracy, the first time step at t=0.05 s is studied.

Right after the bottle is opened, air will start to penetrate into the top bottle, while simultaneously water will start to fall out. The deformation of the interface is due to the Rayleigh-Taylor instability. The exact process and visualization of the first bubble was described in chapter 2.1.5. It is expected that a gaseous finger will start to form at the bottle opening. This was also seen at the timestamp t = 0.05 s. The VOF contour is compared for the different meshes and depicted in figure 91.

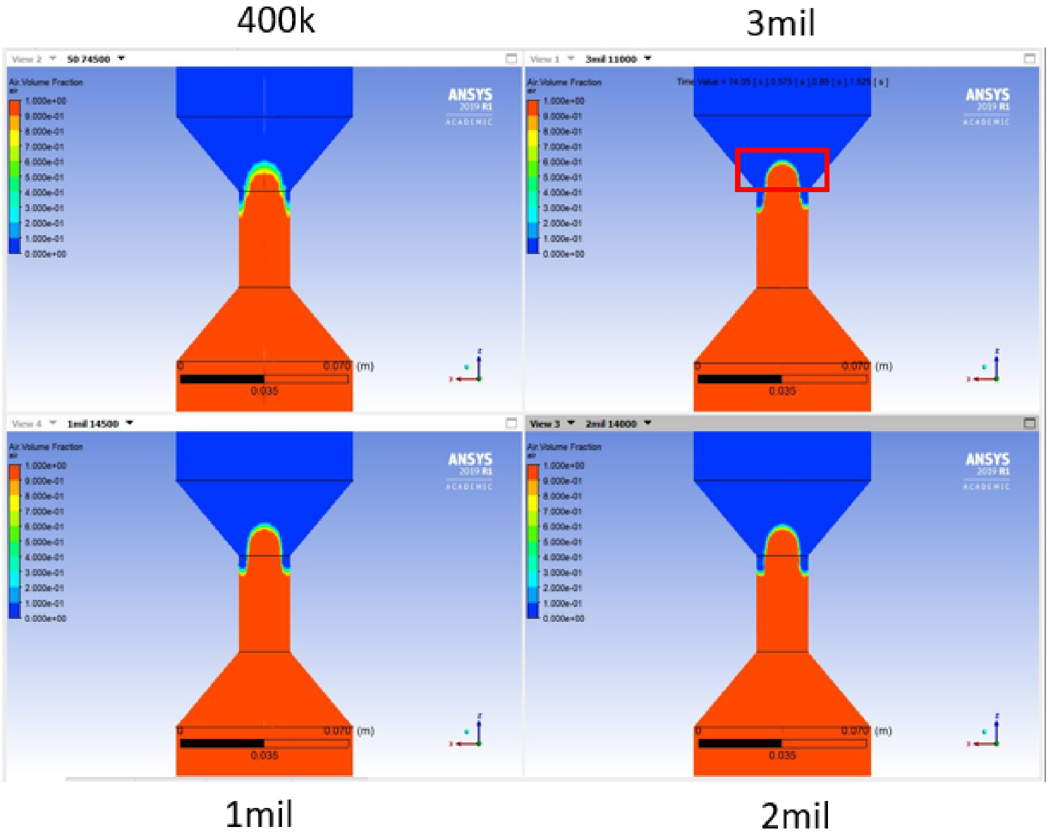

Figure 91: VOF contour for the different meshes

The shape of the gaseous finger looks similar for all the meshes. However, it is fairly important that the development of the free surface is calculated as accurate as possible. Especially for the Eötvos case, where the alteration of surface tension will be investigated. The Rayleigh-Taylor instability can dominate how the bubble regime will behave. To determine whether the meshes were accurate enough, the surface of the bubble was compared by plotting the air volume fraction $\alpha_{air} = 0.9999$ for the area right above the bottle opening. The area is marked with the red box shown in figure 91 for the 3mil mesh. The result is plotted in figure 92. As can be seen in figure 92, a big difference is noticed between the most coarse mesh and the rest of the meshes, whereas the interface for the two finest meshes looks nearly identical.

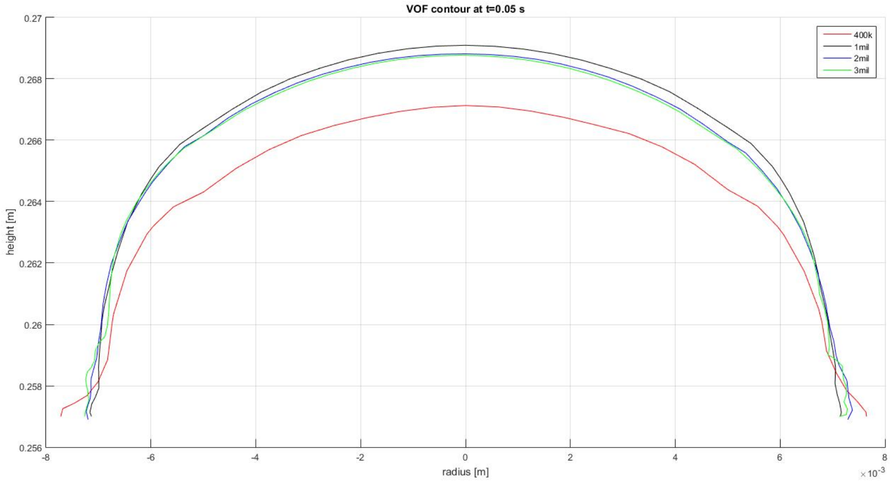

Figure 92: Interface of the gasesous finger right above the bottle opening for $\alpha_{air} = 0.9999$

Also, the circumferential profile was compared and plotted for t=0.05 s and depicted in figure 93a. The exact location of where the circumferential profile is taken is shown as the black dotted line in figure 93b, where the line is a horizontal line in the x-z plane. From the comparison between the 4 meshes, it is obtained that the three finer meshes are close to identical, whereas the coarsest mesh deviates significantly.

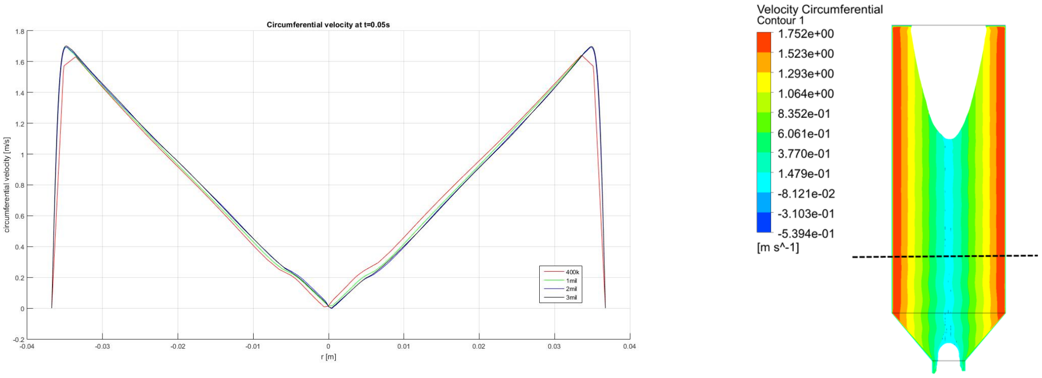

(a) (b)

Figure 93: a) Circumferential plots for the different meshes b) Location of the plotted profile

To check whether the wall regions were fully resolved, a close-up was made on the circumferential velocity profile. A smooth transition should be seen in the close-up. The most coarse mesh did not have any wall refinements, whereas the rest of the meshes were refined in the way described in section 3.3.3. The first cell height had the requirement $y+ = 0.9$, resulting in the first cell height as $y = 3.4 \cdot 10^{-2}$ mm. As can be seen from figure 94, a smooth transition is noticed in the meshes except for the most coarse mesh. Moreover, the 3 different meshes correlated extremely well.

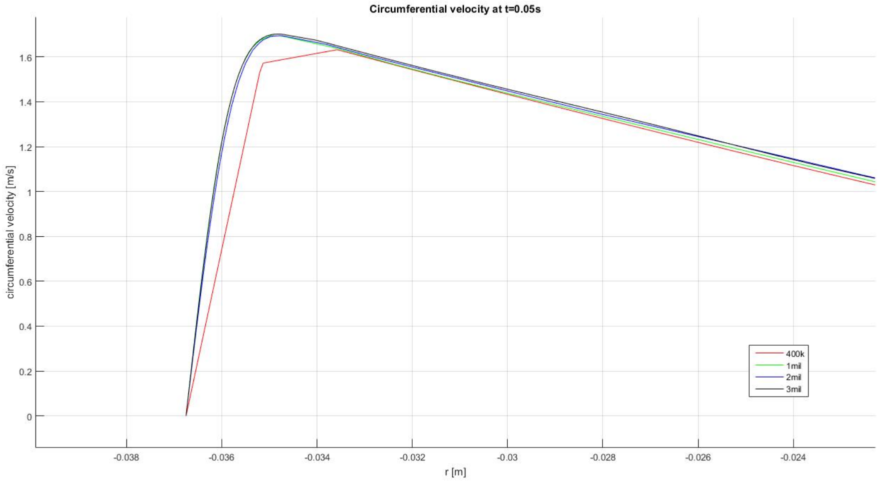

Figure 94: Circumferential velocity profile in the wall region

C.5 t = 1.5 s

At the time step $t = 1.5s$, the beginning phase of the vortex regime is noticed. Due to the transient behaviour of the Taylor vortices, a considerable amount of random peaks were noticed in the velocity profiles. These peaks made it unclear and imprecise when mesh independency had been reached. By applying a time-averaging method, a better correlation was obtained between the finer meshes. The time-averaging method is defined as [86]:

$$\bar{u}^T(t) = \frac{1}{T}\int_{-0.5T}^{+0.5T} u(t+\tau)d\tau \tag{125}$$

where T represents is the averaging time or the time period where time-averaging is applied. In this case, the time-period was taken as one revolution of the vortex. Equation 125 can also be written as:

$$\bar{u}^T(t) = \frac{\sum_{i=0}^{N-1} u(t_i)}{N} \tag{126}$$

The time period T where time-averaging was applied, was equal to one revolution of the vortex. By taking $N = 20$ datasets between $-0.5T < t = 1.5s < 0.5T$, averaged velocity profiles could be obtained. The time-averaged circumferential and axial velocity profiles are depicted in figure 95 and 96.The marked grey area represents the air-core, while the white area indicates the liquid layer. The locations of these plots are on the same dotted line displayed in figure 93b.

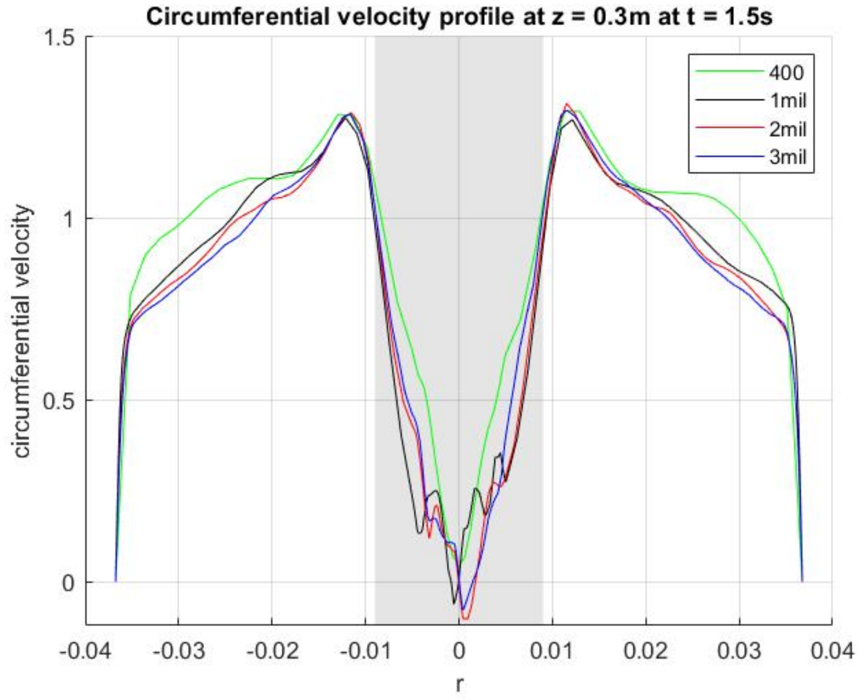

Figure 95: Time-averaged circumferential velocity profile at t=1.5 s

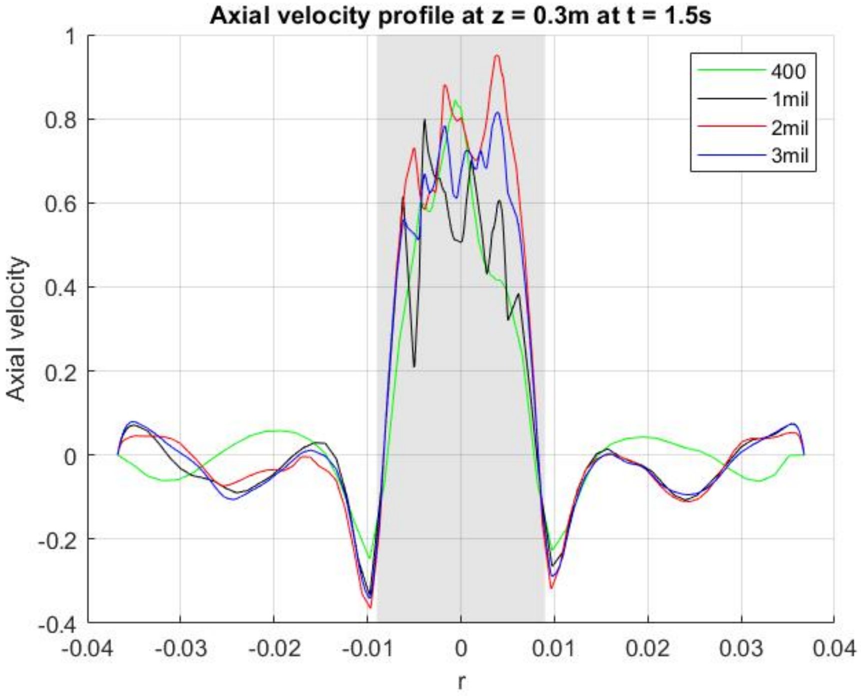

Figure 96: Time-averaged axial velocity profile at t=1.5 s

As can be seen in the velocity plots, time-averaging smoothed out the peaks in the liquid layer. where the velocity profile in the liquid layer already started to indicate mesh independence. However, uncorrelated peaks were still found in the air-core. These peaks are being formed due to the chaotic turbulent flow characteristics. It is expected that by increasing the mesh density, more accurate results will be obtained for the air layer. However, as discussed before, by refining the grid more, the required computational resources and time will increase significantly. It is believed that the generation of the vortex and the drainage time is mainly influenced by the liquid layer and thus a compromise has been made where if mesh independence was found for the velocity profiles in the liquid layer, overall mesh dependence would be declared.

C.6 Taylor vortices

The flow regime in the drainage period is characterized by the Taylor vortices. To ensure that the mesh density was fine enough, an analysis on the flow characteristics also had to be performed. The Rayleigh instability in the form of Taylor vortices had to be present in the numerical flow regime, otherwise the mesh was too inaccurate, resulting in non-physical numerical results. This is done by looking at the vector velocity field depicted in figure 97a. The mesh that is used in figure 97 is the 1 million mesh. When taking a closer look in the red box in figure 97, it is noticed that these Taylor vortices are present in the numerical results (in the red circles). This means that the mesh density is fine enough to predict these vortices and the characteristic turbulent behaviour of the spin-down regime.

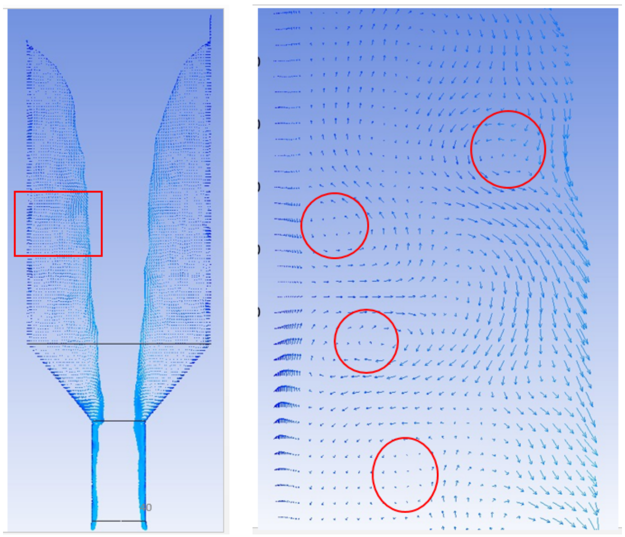

(a) (b)

Figure 97: a) Velocity vector field b) Zoomed in on the red box

C.7 Conclusion of the mesh independence study

Comparing the different results obtained in this section, it can be argued that the numerical results obtained from the coarsest mesh (400k) deviated too much in comparison with the other meshes. Refining the 400k would increase the accuracy significantly, thus mesh independency was by no means achieved. Slight differences were still found between the 1mil and 2mil mesh, however the difference was considerably smaller compared to the first refinement. The last refinement was not fully comparable due to the unfinished 3mil case. However, by comparing the first few seconds of the drainage, preliminary conclusions could be drawn, where it was obtained that they started to look identical for a few of the studied parameters. Thus, the right decision was to select the 2mil mesh. However, taking into account the significant increase in computational time, the available time for this study and only the slight difference in results, it was chosen to select the 1mil mesh as the mesh for the remaining study. It is believed that the results should still be accurate enough to draw conclusions about the effects of the three dimensionless parameters on the drainage time and the overall flow structure.

D Appendix III: Verification with experimental results

To verify the grid, experimental results made by the bachelor students were used for comparison. Their results are discussed in appendix A. They performed several experiments with glycerol and water combinations. A combination of 35%-glycerol and 65%-water was chosen for verification of the numerical model. They performed their experimental results with an initial angular velocity of 27 radian per second. They measured the drainage time and filmed the rising liquid level of the bottom bottle through time. By tracking the interface with the software Tracker [100], the graph with the line labeled "experimental" in figure 98 could be obtained. For the numerical case, a more accurate approach was performed, where the volume in the bottom bottle was calculated and measured over time by using CFD Post. This is labeled as "ansys" in figure 98. As can be seen in figure 98, the vertical axis is labeled as "h*", which is defined as the dimensionless height ($h^* = h/h_0$), where h_0 is the initial liquid level. Thus, for the numerical data, the volume that was calculated by Ansys was divided by the area of the bottle to obtain the liquid level. The shape of the lines did not fully align correctly with each other in the transition regime and parts of the vortex regime, however the drainage times were quite similar. The experimental drainage time that was measured by the bachelor students was 7.34 seconds, whereas Ansys calculated 7.05 seconds. Normally, multiple test cases should be verified with the numerical results to fully proof that the mesh and numerical settings are chosen correctly. However, looking at the duration of this study, for now it is satisfactory to say that with this verification, the 1million mesh is fine enough to provide accurate results.

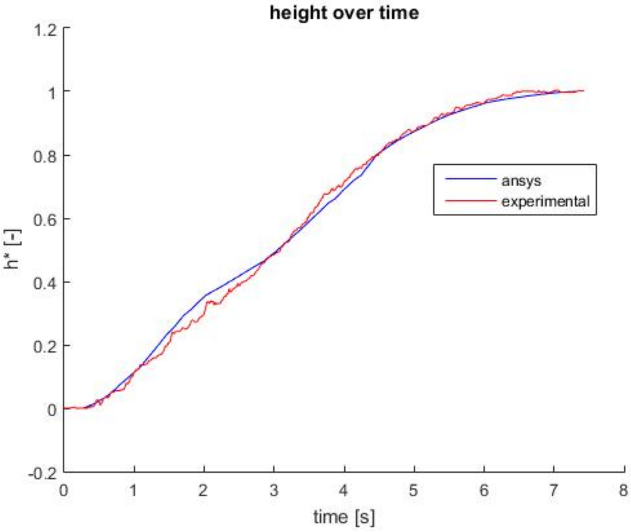

Figure 98: Comparison of the transient liquid level between experimental and numerical data

References

[1] B. L. Gowda, P. Joshy, and S. Swarnamani, “Device to suppress vortexing during draining from cylindrical tanks,” *Journal of spacecraft and rockets*, vol. 33, no. 4, pp. 598–600, 1996.

[2] M. Baum and M. Cook, “Gas entrainment at the free surface of a liquid: entrainment inception at a vortex with an unstable gas core,” *Nuclear Engineering and Design*, vol. 32, no. 2, pp. 239–245, 1975.

[3] S. Dhakal, A. B. Timilsina, R. Dhakal, D. Fuyal, T. R. Bajracharya, H. P. Pandit, N. Amatya, and A. M. Nakarmi, “Comparison of cylindrical and conical basins with optimum position of runner: Gravitational water vortex power plant,” *Renewable and Sustainable Energy Reviews*, vol. 48, pp. 662–669, 2015.

[4] G. B. Wallis, “One-dimensional two-phase flow,” 1969.

[5] F. Viana, R. Pardo, R. Yánez, J. L. Trallero, and D. D. Joseph, “Universal correlation for the rise velocity of long gas bubbles in round pipes,” *Journal of Fluid Mechanics*, vol. 494, pp. 379–398, 2003.

[6] C.-W. Kang, S. Quan, and J. Lou, “Numerical study of a taylor bubble rising in stagnant liquids,” *Physical Review E*, vol. 81, no. 6, p. 066308, 2010.

[7] D. H. Sharp, “Overview of rayleigh-taylor instability,” tech. rep., Los Alamos National Lab., NM (USA), 1983.

[8] R. Clift and W. Gauvin, “Motion of entrained particles in gas streams,” *The Canadian Journal of Chemical Engineering*, vol. 49, no. 4, pp. 439–448, 1971.

[9] C. S. Martin, “Vertically downward two-phase slug flow,” 1976.

[10] D. T. Dumitrescu, “Strömung an einer luftblase im senkrechten rohr,” *ZAMM - Journal of Applied Mathematics and Mechanics / Zeitschrift für Angewandte Mathematik und Mechanik*, vol. 23, no. 3, pp. 139–149, 1943.

[11] R. Davies and G. I. Taylor, “The mechanics of large bubbles rising through extended liquids and through liquids in tubes,” *Proceedings of the Royal Society of London. Series A. Mathematical and Physical Sciences*, vol. 200, no. 1062, pp. 375–390, 1950.

[12] E. White and R. Beardmore, “The velocity of rise of single cylindrical air bubbles through liquids contained in vertical tubes,” *Chemical Engineering Science*, vol. 17, no. 5, pp. 351–361, 1962.

[13] D. Nicklin, “Two-phase flow in vertical tubes, trans,” *Inst. Chem. Engr.*, vol. 40, no. 1, pp. 61–68, 1962.

[14] S. Polonsky, L. Shemer, and D. Barnea, “The relation between the taylor bubble motion and the velocity field ahead of it,” *International Journal of Multiphase Flow*, vol. 25, no. 6-7, pp. 957–975, 1999.

[15] L. Rohilla and A. K. Das, “Fluidics in an emptying bottle during breaking and making of interacting interfaces,” *Physics of Fluids*, vol. 32, no. 4, p. 042102, 2020.

[16] S. G. Bankoff and S. C. Lee, “A critical review of the flooding literature,” in *Multiphase Science and Technology*, pp. 95–180, Springer, 1986.

[17] R. Davies and G. I. Taylor, “The mechanics of large bubbles rising through extended liquids and through liquids in tubes,” *Proceedings of the Royal Society of London. Series A. Mathematical and Physical Sciences*, vol. 200, no. 1062, pp. 375–390, 1950.

[18] P. Whalley, “Flooding, slugging and bottle emptying,” *International journal of multiphase flow*, vol. 13, no. 5, pp. 723–728, 1987.

[19] C. Clanet and G. Searby, “On the glug-glug of ideal bottles,” *Journal of Fluid Mechanics*, vol. 510, p. 145, 2004.

[20] A. Andersen, T. Bohr, B. Stenum, J. J. Rasmussen, and B. Lautrup, “Anatomy of a bathtub vortex,” *Physical review letters*, vol. 91, no. 10, p. 104502, 2003.

[21] C. K. Batchelor and G. Batchelor, *An introduction to fluid dynamics.* Cambridge university press, 2000.

[22] V. B. Bhatia, *Classical mechanics: With introduction to nonlinear oscillations and chaos.* Alpha Science Int’l Ltd., 1997.

[23] A. H. Shapiro, “Bath-tub vortex,” *Nature*, vol. 196, no. 4859, pp. 1080–1081, 1962.

[24] P. A. Tyvand and K. B. Haugen, “An impulsive bathtub vortex,” *Physics of Fluids*, vol. 17, no. 6, p. 062105, 2005.

[25] J. Proudman, “On the motion of solids in a liquid possessing vorticity,” *Proceedings of the Royal Society of London. Series A, Containing Papers of a Mathematical and Physical Character*, vol. 92, no. 642, pp. 408–424, 1916.

[26] S. Zilitinkevich, “On the determination of the height of the ekman boundary layer,” *Boundary-Layer Meteorology*, vol. 3, no. 2, pp. 141–145, 1972.

[27] F. Busse, E. Dormy, R. Simitev, and A. Soward, “Dynamics of rotating fluids,” *Mathematical aspects of natural dynamos*, pp. 119–198, 2007.

[28] A. Andersen, T. Bohr, B. Stenum, J. J. Rasmussen, and B. Lautrup, “The bathtub vortex in a rotating container,” *Journal of Fluid Mechanics*, vol. 556, pp. 121–146, 2006.

[29] W. S. Lewellen, “A solution for three-dimensional vortex flows with strong circulation,” *Journal of Fluid Mechanics*, vol. 14, no. 3, p. 420–432, 1962.

[30] Y.-C. Chen, S.-L. Huang, Z.-Y. Li, C.-C. Chang, and C.-C. Chu, “A bathtub vortex under the influence of a protruding cylinder in a rotating tank,” *Journal of Fluid Mechanics*, vol. 733, pp. 134–157, 2013.

[31] A. Eliassen, “On the ekman layer in a circular vortex,” *Journal of the Meteorological Society of Japan. Ser. II*, vol. 49, pp. 784–789, 1971.

[32] Y. A. Stepanyants and G. H. Yeoh, “Stationary bathtub vortices and a critical regime of liquid discharge,” *Journal of Fluid Mechanics*, vol. 604, pp. 77–98, 2008.

[33] K. Stewartson, “On almost rigid rotations,” *Journal of Fluid Mechanics*, vol. 3, no. 1, p. 17–26, 1957.

[34] R. Hide and C. Titman, “Detached shear layers in a rotating fluid,” *Journal of Fluid Mechanics*, vol. 29, no. 1, pp. 39–60, 1967.

[35] R. Hide, “On source-sink flows in a rotating fluid,” *Journal of Fluid Mechanics*, vol. 32, no. 4, pp. 737–764, 1968.

[36] D. W. Moore and P. G. Saffman, “The structure of free vertical shear layers in a rotating fluid and the motion produced by a slowly rising body,” *Philosophical Transactions of the Royal Society of London. Series A, Mathematical and Physical Sciences*, vol. 264, no. 1156, pp. 597–634, 1969.

[37] S. Smith, “The formation of stewartson layers in a rotating fluid,” *The Quarterly Journal of Mechanics and Applied Mathematics*, vol. 40, no. 4, pp. 575–594, 1987.

[38] W. B. Watkins and R. Hussey, “Spin-up from rest in a cylinder,” *The Physics of Fluids*, vol. 20, no. 10, pp. 1596–1604, 1977.

[39] E. Benton and A. Clark Jr, “Spin-up,” *Annual Review of Fluid Mechanics*, vol. 6, no. 1, pp. 257–280, 1974.

[40] M. Basta, V. Picciarelli, and R. Stella, “A simple experiment to study parabolic surfaces,” *Physics Education*, vol. 35, no. 2, p. 120, 2000.

[41] J. H. Son, C. H. Sohn, and I. S. Park, “Numerical study of 3-d air core phenomenon during liquid draining,” *Journal of Mechanical Science and Technology*, vol. 29, no. 10, pp. 4247–4257, 2015.

[42] N. Khoshkalam, A. F. Najafi, M. H. Rahimian, and F. Magagnato, “Numerical study on air-core vortex: analysis of generation mechanism,” *Archive of Applied Mechanics*, vol. 90, no. 1, pp. 1–16, 2020.

[43] C. H. Sohn, J. H. Son, and I. S. Park, “Numerical analysis of vortex core phenomenon during draining from cylinder tank for various initial swirling speeds and various tank and drain port sizes,” *Journal of Hydrodynamics*, vol. 25, no. 2, pp. 183–195, 2013.

[44] S. Yukimoto, H. Niino, T. Noguchi, R. Kimura, and F. Y. Moulin, “Structure of a bathtub vortex: importance of the bottom boundary layer,” *Theoretical and Computational Fluid Dynamics*, vol. 24, no. 1-4, pp. 323–327, 2010.

[45] K. Nazir and C. H. Sohn, “Effect of water temperature on air-core generation and disappearance during draining,” *Journal of Mechanical Science and Technology*, vol. 32, no. 2, pp. 703–708, 2018.

[46] T. Lundgren, “The vortical flow above the drain-hole in a rotating vessel,” *Journal of Fluid Mechanics*, vol. 155, pp. 381–412, 1985.

[47] A. J. Odgaard, “Free-surface air core vortex,” *Journal of Hydraulic Engineering*, vol. 112, no. 7, pp. 610–620, 1986.

[48] J. E. Hite Jr and W. C. Mih, “Velocity of air-core vortices at hydraulic intakes,” *Journal of Hydraulic Engineering*, vol. 120, no. 3, pp. 284–297, 1994.

[49] H.-f. Li, H.-x. Chen, Z. Ma, and Y. Zhou, “Experimental and numerical investigation of free surface vortex,” *Journal of hydrodynamics*, vol. 20, no. 4, pp. 485–491, 2008.

[50] J. A. Whitehead Jr and D. L. Porter, “Axisymmetric critical withdrawal of a rotating fluid,” *Dynamics of Atmospheres and Oceans*, vol. 2, no. 1, pp. 1–18, 1977.

[51] D. Dherbecourt, S. Charton, F. Lamadie, S. Cazin, and E. Climent, “Experimental study of enhanced mixing induced by particles in taylor–couette flows,” *Chemical Engineering Research and Design*, vol. 108, pp. 109–117, 2016.

[52] L. R. S. R.S., *XIX. On the instability of cylindrical fluid surfaces*, vol. 34. Taylor & Francis, 1892.

[53] G. I. Taylor, “Viii. stability of a viscous liquid contained between two rotating cylinders,” *Philosophical Transactions of the Royal Society of London. Series A, Containing Papers of a Mathematical or Physical Character*, vol. 223, no. 605-615, pp. 289–343, 1923.

[54] Y. Takeda, “Quasi-periodic state and transition to turbulence in a rotating couette system,” *Journal of Fluid Mechanics*, vol. 389, pp. 81–99, 1999.

[55] F. M. White, *Fluid Mechanics*. Mcgraw-Hill Education, 2011.

[56] C. D. Andereck, S. Liu, and H. L. Swinney, “Flow regimes in a circular couette system with independently rotating cylinders,” *Journal of fluid mechanics*, vol. 164, pp. 155–183, 1986.

[57] S. Mulligan, G. De Cesare, J. Casserly, and R. Sherlock, “Understanding turbulent free-surface vortex flows using a taylor-couette flow analogy,” *Scientific reports*, vol. 8, no. 1, pp. 1–14, 2018.

[58] H. J. Lugt, *Vortex flow in nature and technology.* Wiley & Sons Foundation, 1983.

[59] P. K. Dutta and A. K. Ray, “Experimental investigation of taylor vortex photocatalytic reactor for water purification,” *Chemical Engineering Science*, vol. 59, no. 22-23, pp. 5249–5259, 2004.

[60] J. Burkhalter and E. Koschmieder, “Steady supercritical taylor vortex flow,” *Journal of Fluid Mechanics*, vol. 58, no. 3, pp. 547–560, 1973.

[61] D. Coles, “Transition in circular couette flow,” *Journal of Fluid Mechanics*, vol. 21, no. 3, pp. 385–425, 1965.

[62] G. P. King, Y. Li, W. Lee, H. L. Swinney, and P. S. Marcus, “Wave speeds in wavy taylor-vortex flow,” *Journal of Fluid Mechanics*, vol. 141, pp. 365–390, 1984.

[63] M. Gorman and H. L. Swinney, “Spatial and temporal characteristics of modulated waves in the circular couette system,” *Journal of Fluid Mechanics*, vol. 117, pp. 123–142, 1982.

[64] E. Koschmieder, “Turbulent taylor vortex flow,” *Journal of Fluid Mechanics*, vol. 93, no. 3, pp. 515–527, 1979.

[65] J. B. FlÓr, M. Ungarish, and J. W. Bush, “Spin-up from rest in a stratified fluid: boundary flows,” *Journal of Fluid Mechanics*, vol. 472, pp. 51–82, 2002.

[66] N. El-Ansary, G. Hoshoudy, A. Abd-Elrady, and A. Ayyad, “Effects of surface tension and rotation on the rayleigh–taylor instability,” *Physical Chemistry Chemical Physics*, vol. 4, no. 8, pp. 1464–1470, 2002.

[67] S. Chandrasekhar, *Hydrodynamic and hydromagnetic stability.* Courier Corporation, 2013.

[68] G. Carnevale, P. Orlandi, Y. Zhou, and R. Kloosterziel, “Rotational suppression of rayleigh-taylor instability,” *Journal of Fluid Mechanics*, vol. 457, pp. 181–190, 2002.

[69] F. Geiger, K. Velten, and F.-J. Methner, “3d cfd simulation of bottle emptying processes,” *Journal of food engineering*, vol. 109, no. 3, pp. 609–618, 2012.

[70] V. Hernandez-Perez, M. Abdulkadir, and B. Azzopardi, “Grid generation issues in the cfd modelling of two-phase flow in a pipe,” *The Journal of Computational Multiphase Flows*, vol. 3, no. 1, pp. 13–26, 2011.

[71] H. Schlichting and K. Gersten, *Boundary-layer theory.* Springer, 2016.

[72] H. Sarkardeh, A. Reza Zarrati, E. Jabbari, and M. Marosi, “Numerical simulation and analysis of flow in a reservoir in the presence of vortex,” *Engineering Applications of Computational Fluid Mechanics*, vol. 8, no. 4, pp. 598–608, 2014.

[73] I. F. Suerich-Gulick, *Axial stretching, viscosity, surface tension and turbulence in free surface vortices at low-head hydropower intakes.* PhD thesis, McGill University Libraries, 2013.

[74] S. Mulligan, “Experimental and numerical analysis of three-dimensional free-surface turbulent vortex flows with strong circulation,” *Ireland: Institute of Technology Sligo*, 2015.

[75] W.-L. Chuang and S.-C. Hsiao, “Three-dimensional numerical simulation of intake model with cross flow,” *Journal of Hydrodynamics*, vol. 23, no. 3, pp. 314–324, 2011.

[76] A. Škerlavaj, A. Lipej, J. Ravnik, and L. Škerget, “Turbulence model comparison for a surface vortex simulation,” in *IOP Conference Series: Earth and Environmental Science*, vol. 12, p. 012034, IOP Publishing, 2010.

[77] T. Sakai, Y. Eguchi, H. Monji, K. Ito, and H. Ohshima, “Proposal of design criteria for gas entrainment from vortex dimples based on a computational fluid dynamics method,” *Heat Transfer Engineering*, vol. 29, no. 8, pp. 731–739, 2008.

[78] S. Muntean, I. Buntić, A. Ruprecht, and R. Susan-Resiga, “A numerical investigation of the 3d swirling flow in a pipe with constant diameter—part 2: Turbulent computation,” *Sci. Bull. Politeh. Univ. Timisoara, Trans. Mech.*, vol. 50, no. 64, pp. 87–96, 2005.

[79] S. O. Unverdi and G. Tryggvason, “A front-tracking method for viscous, incompressible, multi-fluid flows,” 1992.

[80] J. E. Welch, “The mac method-a computing technique for solving viscous, incompressible, transient fluid-flow problems involving free surfaces,” *Los Alamos scientific laboratory report LA-3425*, 1968.

[81] C. W. Hirt and B. D. Nichols, “Volume of fluid (vof) method for the dynamics of free boundaries,” *Journal of computational physics*, vol. 39, no. 1, pp. 201–225, 1981.

[82] M. Sussman and E. G. Puckett, “A coupled level set and volume-of-fluid method for computing 3d and axisymmetric incompressible two-phase flows,” *Journal of computational physics*, vol. 162, no. 2, pp. 301–337, 2000.

[83] T. Ménard, S. Tanguy, and A. Berlemont, “Coupling level set/vof/ghost fluid methods: Validation and application to 3d simulation of the primary break-up of a liquid jet,” *International Journal of Multiphase Flow*, vol. 33, no. 5, pp. 510–524, 2007.

[84] D. Sun and W. Tao, “A coupled volume-of-fluid and level set (voset) method for computing incompressible two-phase flows,” *International Journal of Heat and Mass Transfer*, vol. 53, no. 4, pp. 645–655, 2010.

[85] N. Y. Gnedin, V. A. Semenov, and A. V. Kravtsov, “Enforcing the courant–friedrichs–lewy condition in explicitly conservative local time stepping schemes,” *Journal of Computational Physics*, vol. 359, pp. 93–105, 2018.

[86] F. T. Nieuwstadt, J. Westerweel, and B. J. Boersma, *Turbulence: introduction to theory and applications of turbulent flows.* Springer, 2016.

[87] K. A. Baldwin, M. M. Scase, and R. J. Hill, “The inhibition of the rayleigh-taylor instability by rotation,” *Scientific reports*, vol. 5, p. 11706, 2015.

[88] R. Ostilla-Mónico, E. P. Van Der Poel, R. Verzicco, S. Grossmann, and D. Lohse, “Exploring the phase diagram of fully turbulent taylor–couette flow,” *Journal of fluid mechanics*, vol. 761, pp. 1–26, 2014.

[89] K. Takamura, H. Fischer, and N. R. Morrow, “Physical properties of aqueous glycerol solutions,” *Journal of Petroleum Science and Engineering*, vol. 98, pp. 50–60, 2012.

[90] S. Nogueira, M. Riethmuler, J. Campos, and A. Pinto, “Flow in the nose region and annular film around a taylor bubble rising through vertical columns of stagnant and flowing newtonian liquids,” *Chemical Engineering Science*, vol. 61, no. 2, pp. 845–857, 2006.

[91] R. Bellman and R. H. Pennington, “Effects of surface tension and viscosity on taylor instability,” *Quarterly of Applied Mathematics*, vol. 12, no. 2, pp. 151–162, 1954.

[92] P. B. Zielinski, “Effect of viscosity on vortex orifice flow,” *Journal of the Hydraulics Division*, vol. 94, no. 3, pp. 745–752, 1968.

[93] M. I. Kohira, N. Magome, H. Kitahata, and K. Yoshikawa, “Plastic bottle oscillator: Rhythmicity and mode bifurcation of fluid flow,” *American Journal of Physics*, vol. 75, no. 10, pp. 893–895, 2007.

[94] S.-I. Sohn, “Effects of surface tension and viscosity on the growth rates of rayleigh-taylor and richtmyer-meshkov instabilities,” *Physical Review E*, vol. 80, no. 5, p. 055302, 2009.

[95] S.-I. Sohn and S. Baek, “Bubble merger and scaling law of the rayleigh–taylor instability with surface tension,” *Physics Letters A*, vol. 381, no. 45, pp. 3812–3817, 2017.

[96] L. L. Daggett, G. H. Keulegan, *et al.*, “Similitude conditions in free-surface vortex formations,” 1974.

[97] H. O. Anwar, J. A. Weller, and M. B. Amphlett, “Similarity of free-vortex at horizontal intake,” *Journal of Hydraulic Research*, vol. 16, no. 2, pp. 95–105, 1978.

[98] J. Taber, J. Kirby, and F. Schroeder, “Studies on the displacement of residual oil: Viscosity and permeability effects,” in *AIChE Symp. Ser*, vol. 69, p. 53, 1973.

[99] H. Fischer and N. R. Morrow, “Scaling of oil recovery by spontaneous imbibition for wide variation in aqueous phase viscosity with glycerol as the viscosifying agent,” *Journal of Petroleum Science and Engineering*, vol. 52, no. 1-4, pp. 35–53, 2006.

[100] D. Brown, “Tracker 5.1.4.” `https://physlets.org/tracker`.